Thermo-hydro-mechanical simulation of a generic geological disposal facility for radioactive waste

Samuel William Parsons
University of Leeds
School of Earth and Environment

Submitted in accordance with the requirements for the degree of
Doctor of Philosophy
February, 2020

Acknowledgements

Thank you to Dr David Price, Professor Quentin Fisher, Dr Hannah Bentham, Dr Tom Lynch and James Woodman for their feedback and collaboration. Thank you to Dr Doug Angus, Professor Graham Stuart, Dr William Murphy and Dr Mark Hildyard for their supervision. Thank you to my examiners, Dr Mark Thomas and Professor Peter Cleall. Thank you to everyone within the HydroFRAME consortium, especially, Dr John-Paul Latham who started me off on this journey.

Thank you to NERC RATE, RWM and EA for backing the opportunity. Thank you to Rockfield for their software and support. Thank you to ANDRA and GRS for sharing their heater test data.

Special thanks to my family and friends for their love and support, always.

Abstract

Geological disposal is required for the safe and long-term disposal of legacy radioactive waste. High level waste and spent fuel generate significant heat that will cause thermo-hydro-mechanical coupled processes in the rock mass. The thermal expansion of the fluid will be greater than the grains causing a decrease in mean effective stress with the low permeability ($<10^{-19}$) restricting Darcy flow and excess pore pressure equilibration. A decrease in mean effective stress can reduce material strength in granular materials, which may be significant near excavations where differential stress is increased. Microseismic monitoring provides cost effective, non-intrusive and three-dimensional data that can be calibrated with the stress and strain behaviour of a rock mass. However, there is no precedent for the microseismic monitoring of heat-producing radioactive waste. Generic concepts, analogue materials and data from in situ experiments are used to demonstrate the potential for the microseismic monitoring of heat-producing radioactive waste in lower strength sedimentary rocks. A mechanism for early post-closure microseismicity is demonstrated, whereby excess pore pressure decreases the mean effective stress towards yielding in shear. The rock and fluid property uncertainties are ranked according to their contribution to the excess pore pressure. Permeability is found to be important as expected, however, Biot's coefficient is demonstrably more important and yet often overlooked. Furthermore, the microseismic event locations, timings and pseudo scalar seismic moments are shown to have statistically significant relationships with the engineered backfill swelling pressure. Therefore, early post-emplacement microseismic monitoring could provide constraints for the engineered backfill swelling pressure and rock property uncertainties whilst the facility is still operational. Insights could prove timely for adapting the engineering designs, if they are not behaving as expected, in further high level waste and spent fuel tunnels.

CONTENTS

Abbreviations **xi**

Common Symbols **xiii**

List of Figures **xv**

List of Tables **xvii**

1 Introduction **1**

1.1 Motivation 1
1.2 Aim, objectives and scope 4
1.3 Thesis structure 5

2 Literature review **7**

2.1 Radioactive waste disposal 7
2.2 Numerical modelling 10
2.2.1 Coupled thermo-hydro-mechanical modelling 10
2.2.2 Numerical modelling methods 15
2.3 Rock mass uncertainty 18
2.3.1 Rock mass characterization 18
2.3.2 Sensitivity analysis 19
2.4 Seismic monitoring methods 21
2.4.1 Microseismic monitoring 22
2.5 Summary 23

3 Numerical modelling theory and validation **25**

3.1 Introduction 25
3.2 Multifield modelling theoretical formulation 27
3.2.1 Thermal field 28
3.2.2 Porous flow field 29
3.2.3 Geomechanical field 30
3.3 Case study: HE-D experiment 35

3.3.1 Comparability of other heater test methods 36
3.4 Model setup 37
3.4.1 Geometry 38
3.4.2 Conditions 40
3.4.3 Host rock properties 42
3.5 HE-D benchmark test results 50
3.5.1 Temperature 50
3.5.2 Pore pressure 51
3.6 Discussion 54
3.6.1 Transient pore pressure anomaly 54
3.6.2 Summary 55

4 Global sensitivity analysis **59**

4.1 Introduction 59
4.2 Global sensitivity analysis approach 60
4.2.1 Elementary Effects Test 61
4.2.2 Regional sensitivity analysis 62
4.2.3 PAWN sensitivity analysis 63
4.2.4 Variance-based sensitivity analysis 64
4.2.5 Assessing convergence 64
4.3 Experimental setup 65
4.3.1 Model 65
4.3.2 Defining the model output 66
4.3.3 Uncertainty in the rock properties 67
4.3.4 Sampling the input factor space 69
4.4 Results 71
4.4.1 Mean effective stress 72
4.4.2 Temperature 77
4.4.3 Pore pressure 78
4.4.4 Displacement 79
4.5 Discussion 79

5 Microseismic modelling 83
5.1 Introduction 83
5.2 Experimental setup 85
  5.2.1 Model 85
  5.2.2 Input factor ranges for sensitivity analysis 88
5.3 Microseismic modelling 90
  5.3.1 Thermo-hydro-mechanical and microseismic modelling 90
  5.3.2 Microseismic event distribution 91
  5.3.3 Microseismic source magnitude and mechanism 91
5.4 Results 92
  5.4.1 Stress plotting 92
  5.4.2 Input factor mapping for microseismicity 95
  5.4.3 Microseismic monitoring insights 97
5.5 Discussion 104

6 Discussion 107
6.1 Introduction 107
6.2 Thermo-hydro-mechanical modelling for GDFs 107
  6.2.1 Benchmark test temperature behaviour 109
  6.2.2 Benchmark test pore pressure behaviour 111
  6.2.3 Benchmark test displacement behaviour 113
  6.2.4 Isotropic and anisotropic representations 113
6.3 Global sensitivity analysis 115
  6.3.1 Input factor screening 115
  6.3.2 Input factor ranking 118
  6.3.3 Effect of anisotropy 119
  6.3.4 Maximising data 120
6.4 Microseismic monitoring for GDFs 121
  6.4.1 Representation of heat-producing waste in rock 121
  6.4.2 Pseudo scalar seismic moment 123
  6.4.3 Predicted microseismicity 125
  6.4.4 Input factor space 127
6.5 Summary 130

7 Conclusions **131**
7.1 Aim and approach . . . 131
7.2 Originality . . . 132
7.3 Findings . . . 132
7.4 Applications . . . 134
7.5 Future work . . . 134

References **136**

Appendix **175**

ABBREVIATIONS

AGR	Advanced gas-cooled reactor
BEIS	Department for Business, Energy and Industrial Strategy
BGS	British Geological Society
DECC	Department of Energy and Climate Change
DEM	Discrete element method
EA	Environment Agency
EET	Elementary Effects Test
FEM	Finite element method
GDF	Geological disposal facility
HLW	High level waste
IAEA	The International Atomic Energy Agency
NDA	Nuclear Decommissioning Authority
OECD	Organisation for Economic Co-operation and Development
RWM	Radioactive Waste Management
THM	Thermo-hydro-mechanical
URL	Underground research laboratory

COMMON SYMBOLS

Geomechanics

$\rho_{b/s/f}$	Density
E	Young's modulus
ν	Poisson's ratio
P_c	Pre-consolidation pressure
P_t	Tensile intercept
β	Friction angle
κ	Gradient of the elastic unloading-reloading line
λ	Gradient of the normal consolidation line
ϕ	Porosity
k	Permeability
μ	Viscosity
$K_{s/f}$	Stiffness
α	Biot's coefficient
$c_{b/s/f}$	Specific heat capacity
$\lambda_{s/f}$	Thermal conductivity
$\alpha_{s/f}$	Thermal expansion coefficient
σ_{ij}	Stress tensor
σ'_{ij}	Effective stress tensor
p'	Mean effective stress
q	Deviatoric stress
ϵ_v	Volumetric strain
ϵ_v^p	Volumetric plastic strain
$\dot{\epsilon}^p$	Plastic flow
p_f	Pore fluid pressure
q_f	Darcy fluid flux
T	Temperature
q_t	Local heat flux
t	Time
M_0	Seismic moment

* $_{b/s/f}$ denotes bulk, solid or fluid property

Statistics

x	Input factor matrix
y	Output factor vector
n	Latin Hypercube sample size
N	Total sample size for EET sampling
k	Number of input factors
x_0	Non-influential group of input factors
T	Threshold value
EE	Elementary Effect
μ_i^*	Total effects sensitivity indices
σ_i	Standard deviation of Elementary Effects
S_i	Sensitivity indices (multi-method approach)
V	Variance
R	Correlation coefficient

LIST OF FIGURES

1.1 Illustration of a generic GDF. 3

2.1 Generic lower strength sedimentary host rock environment in the UK. 9
2.2 Events and perturbations during the lifetime of a GDF. 10
2.3 Illustrative summary of the simulated THM coupled processes. 11
2.4 Numerical methods for an excavation in a rock mass. 15
2.5 Photograph of a triaxial rig. 19
2.6 Microseismic event location demonstrated in Verdon et al. (2011). . . 23

3.1 Layout of the HE-D experiment with heater and measuring boreholes. 26
3.2 Non-linear dependence of intrinsic permeability on porosity. 30
3.3 Nonlinear dependence of Young's modulus on mean effective stress. . 31
3.4 Soft rock (SR3) yield surface. 32
3.5 Unloading-reloading line and normal compression line. 34
3.6 Examples of the hardening/softening evolution functions. 35
3.7 Various geometric representations of a disposal tunnel. 39
3.8 Geometry and mesh for the HE-D model. 40
3.9 Thermal load for the HE-D model. 41
3.10 Properties of twelve generic clays. 44
3.11 Column test conceptual model and model mesh. 45
3.12 Compaction curves of the generic clays. 46
3.13 Triaxial test conceptual model, model geometry and mesh. 47
3.14 Triaxial test behaviour of the generic clays. 49
3.15 Triaxial test behaviour of the Opalinus Clay. 50
3.16 Predicted temperature and pore pressure contour plots. 51
3.17 Benchmark test for temperature at the sensor locations. 52
3.18 Benchmark test for pore pressure at the sensor locations. 53
3.19 Peak pore pressure shift analysis for opposite effect diagnosis. 56

4.1 Illustrative example of the Elementary Effects Test sensitivity indices. 61
4.2 Illustrative example of the regional sensitivity analysis indices. 62

4.3 Illustrative example of the PAWN sensitivity indices. 63
4.4 Illustrative example of the variance-based sensitivity analysis indices. 65
4.5 Illustrative examples of random and Latin Hypercube sampling. . . . 70
4.6 Elementary Effects Test sensitivity indices for the mean effective stress. 73
4.7 Time varying heat map of elementary effects for mean effective stress. 74
4.8 Andres Test for validating screening. 75
4.9 Multi-method sensitivity indices of the reduced set of input factors. . 76
4.10 Elementary effects computed for temperature. 77
4.11 Elementary effects computed for pore pressure. 78
4.12 Elementary effects computed for x-displacement. 80

5.1 Schematic diagram illustrating an SR3 yield envelope in p'-q space. . 84
5.2 Lower strength sedimentary rock concept for HLW disposal tunnels. . 85
5.3 Axisymmetric model for the HLW disposal tunnel. 87
5.4 HLW and AGR spent fuel disposal canister power curves. 88
5.5 Support pressure percentage of in situ vertical stress. 90
5.6 Event locations and stress path plotting for microseismic events. . . . 93
5.7 Radial transects of pore pressure 2 years after waste emplacement. . . 94
5.8 Input factor mapping for no microseismicity. 95
5.9 Input factor mapping for microseismicity after backfilling. 96
5.10 Microseismicity mapped onto swelling pressure against depth. 97
5.11 Histograms for microseismic events after waste emplacement. 98
5.12 Mean effective stress and pore pressure against time. 99
5.13 Histograms for grouped microseismic events after waste emplacement. 100
5.14 2D histogram for microseismic events after waste emplacement. . . . 101
5.15 Multi-method sensitivity analysis for the microseismic events. 102
5.16 Multi-method sensitivity analysis for the microseismic events statistics. 103
5.17 Linear regression for total events against swelling pressure. 104
5.18 Linear regression for the response variable swelling pressure. 105

6.1 Temperature and pore pressure curves from the HE-D experiment. . . 108
6.2 Cylindrical radiation from a continuous line source. 110
6.3 HE-D temperature data interpolated onto an axisymmetric space. . . 114
6.4 RWM lower strength sedimentary rock concept for HLW. 122

List of Tables

3.1 Hydraulic and thermal properties of the Opalinus Clay. 43
3.2 Geomechanical properties of the Opalinus Clay. 48

4.1 Input factor space for the Opalinus Clay in the experiment test site. . 68
4.2 Summary table of the screened and ranked input factors. 81

5.1 Input factor space for microseismic modelling. 91

Chapter 1

Introduction

1.1 Motivation

A geological disposal facility (GDF) is internationally recognised as the safest long-term solution for legacy radioactive waste (CoRWM, 2006). A GDF provides long-term and cost-effective protection of people and the environment. The UK is in the national geological screening stage (BGS, 2018) of its project to build a GDF for radioactive waste (OECD, 1995; DECC, 2014). The characterization of the host rock will have inherent uncertainty and this needs to be investigated in numerical modelling. In particular, the effects of the uncertainty should be quantified and methods for reducing the uncertainty should be investigated.

The total radioactivity of UK wastes is $8.3 \times 10^{19}\,\mathrm{Bq}$ (BEIS & NDA, 2016). This does not include spent fuel or wastes from planned decommissioning of nuclear power facilities. For comparison, an estimated $9.4 \times 10^{17}\,\mathrm{Bq}$ was released by the Fukushima Daiichi accident and $5.2 \times 10^{18}\,\mathrm{Bq}$ by the Chernobyl accident (IAEA, 2011a).

High level waste (HLW) is the source of over 95 % of the radioactivity of UK wastes (BEIS & NDA, 2016). HLW is defined as waste in which the temperature may rise significantly as a result of their radioactivity (Defra & Nirex, 2002). Heat-producing waste in a GDF will increase the temperature of the rock mass. Increasing temperature increases fluid flux by increasing pore pressure gradients and decreasing fluid viscosity (Winpenny et al., 2012). Thermally enhanced groundwater flow may erode the concrete barriers that are used for intermediate and low level waste (Watson et al., 2009). Therefore, the generic designs for the GDF have HLW and spent fuel disposal tunnels separated from the intermediate and low level waste disposal tunnels (RWM, 2016a).

There are many other risks for the construction of a GDF and the containment of radionuclides. Risks include, but are not limited to, tunnel profile deformation, rock bursts, induced microseismicity, hazardous material transport and surface uplift. Surface uplift is predicted in GDF forward modelling studies (Amec Foster Wheeler, 2015) and is a risk shared by carbon storage projects (Stenhouse & Savage, 2004; Vasco et al., 2010). This is similar, yet opposite to subsidence which has been caused by mining and oil and gas production (Nagel, 2001). Tunnel profile deformation (Huang et al., 2010) and rock bursts (Zhao et al., 2018a) are similar to well failure and borehole breakouts seen in oil and gas production (Zhang, 2013). Induced microseismicity has societal impacts which have been seen by hydraulic fracturing operations (Warpinski et al., 2001) and geothermal energy operations (Cuenot et al., 2008).

These risks will be managed by extensive characterization and monitoring during construction, operation and closure (RWM, 2016b). For example, microseismic monitoring has been successfully used to predict rock bursts in mining (Ma et al., 2018). Characterization and monitoring are interrelated because monitoring is used to constrain characterizations to reduce uncertainty (i.e. history matching; Ballester & Carter., 2007; Emerick & Reynolds, 2012).

Time-lapse seismic surveys and microseismic monitoring are largely non-intrusive, relatively cheap and provide 3D data (Barkved, 2004). However, there are no precedents for using either method to monitor the unique effects of emplacing heat-producing radioactive waste, therefore, further research is required to assess the effectiveness of these methods. It is possible to use generic concepts (Figure 1.1), underground research laboratories (URLs) and analogue materials to enhance our understanding of the likely feasibility. For example, Bentham et al. (2018) used a generic model to determine if the additional survey design flexibility provided by access to the facility could improve the excavation damage zone resolution from time-lapse seismic monitoring.

Geophysical techniques provide observations which need to be related to rock mass properties (Herwanger & Koutsabeloulis, 2011). Seismic geomechanics relates

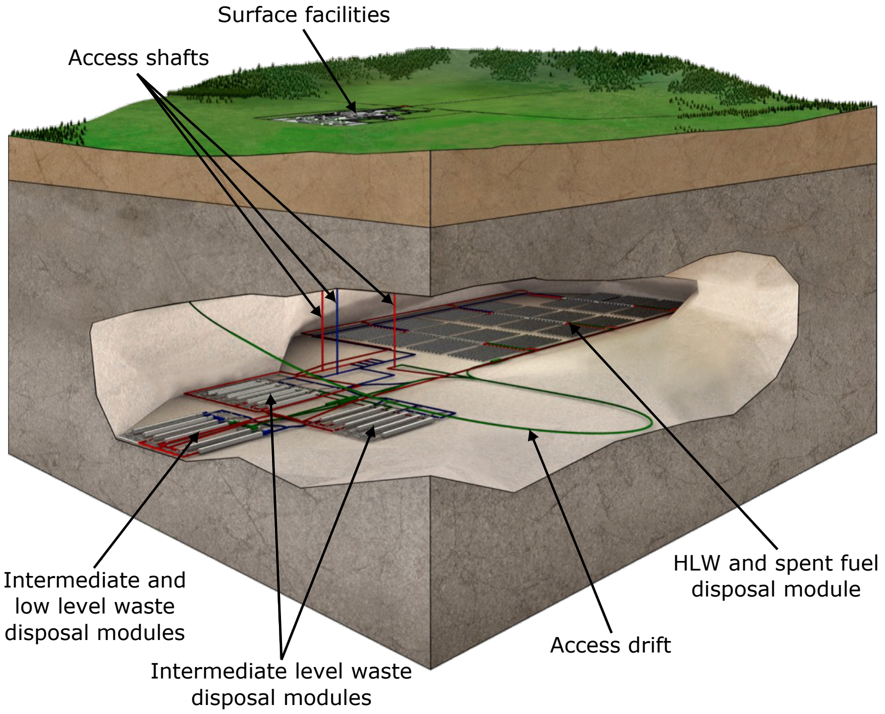

Figure 1.1: Illustration of a generic GDF, in which heat-producing and negligible heat-producing wastes are emplaced into different disposal modules (from NDA, 2010a).

time-lapse seismic velocities to hydro-mechanical modelling using a rock physics model (e.g. Angus et al., 2015; Guilbot & Smith, 2002). Microseismic modelling predicts microseismic events and has been used to identify faults during reservoir depletion (Angus et al., 2010). Thermo-hydro-mechanical (THM) models are common in radioactive waste disposal research aiming to identify risks and constraints (e.g. DECOVALEX, Birkholzer et al., 2018). However, seismic geomechanics and microseismic modelling have not been explored for monitoring a GDF. This may be because there is no requirement for monitoring the GDF post closure. The oversight being that the facility will be operational for decades (Watson et al., 2009; DECOVALEX, 2014) and peak thermally driven pore pressure could be reached around the disposal tunnels during this time.

Using observations (e.g. geophysical) to reduce uncertainty in forward modelling is achieved by exploring an uncertainty space and fitting model results to observations. This is usually called back analysis in rock engineering (Gao et al., 2018; Qi &

Fourie, 2018) and inversion in reservoir engineering (Haas & Dubrule, 1994). By doing so, we can use numerical modelling to characterize a rock mass or to predict with greater confidence using calibrated forward modelling. However, back analysis and sensitivity analysis in geomechanics are typically one-at-a-time analyses assuming all other properties are known (e.g. Zhang et al., 2007a; Seyedi et al., 2018). This does not consider uncertainty in other properties or interactions between multiple properties. Furthermore, inversion in reservoir simulation is typically simpler given that coupled hydro-mechanical modelling has more input factors, interactions and nonlinearity (Price et al., 2017). Yet, there are statistical approaches that are largely overlooked in geomechanics that can be applied to models with many input factors, interactions and nonlinearity (Campolongo et al., 2011; Petropoulos & Srivastava, 2016).

1.2 Aim, objectives and scope

The aim of this work is to investigate the potential for using microseismic monitoring during radioactive waste disposal. Specifically, to explore the previously unconsidered phase of tunnel closure and post-closure because the facility will still be operational after tunnel closures. Uncertainty in rock and fluid property characterization and engineering designs is explored to improve understanding of the processes occurring in the rock mass surrounding heat-producing waste and their relation to microseismicity. The objectives of this work are to:

- Define material properties to represent lower strength sedimentary rock.
- Build a model and validate that it is a good representation of heat-producing waste in lower strength sedimentary rock.
- Determine the effect of uncertainty in rock and fluid properties on observable properties that are perturbed by heat-producing radioactive waste.
- Integrate microseismic modelling with a THM model to predict possible microseismic events near heat-producing waste during the operation of a generic GDF.
- Explore predicted microseismicity from the modelling to determine what insights monitoring could provide during the operation of a generic GDF.

This work uses generic concepts rather than site-specific plans because of the early-stage international outlook (Gens, 2018; IAEA, 2011b; Fayblshenko et al., 2016). From a geological perspective, the main consideration for a GDF is whether the host rock is a lower strength sedimentary rock, higher strength rock or an evaporite (RWM, 2016b). This affects the facility design (RWM, 2016a), likely geological setting (Watson et al., 2007), depth, initial stress and pore pressure conditions (NDA, 2010b). Given the large scope of the challenge, it would have been impossible to address the assessment of all three generic rock types. The lower strength sedimentary host rock is considered in this thesis because quality data was obtained from an in situ heater test in lower strength sedimentary rock allowing for a benchmark test to validate the modelling (Chapter 3).

1.3 Thesis structure

The thesis starts with a review of the current literature that splits into four sections. The first focuses on radioactive waste disposal to explore the problem and its risks, and to discuss conceptual decisions and their context amongst alternatives. The second section focuses on modelling approaches and THM modelling applications. The third section focuses on exploring uncertainty and sensitivity analyses. The fourth section focuses on seismic monitoring methods and their applications.

In Chapter 3 the model setup and validation is discussed. Firstly, the modelling software, ELFEN developed by Rockfield Software Limited (Rockfield Software Limited, 2013a; 2013b), is introduced and the theoretical formulation used in the modelling is described. The theoretical formulation describes the THM coupling and the material characterizations. Then an in situ heating experiment (Wileveau & Rothfuchs, 2003; Zhang et al., 2007a) is described as a case study for benchmarking a THM model. Then the setup of that THM model is described. Finally, there is an analysis of the model results and comparison with the benchmark to validate the theoretical formulation.

A sensitivity analysis on the validated model forms the basis for Chapter 4. Firstly, the sensitivity analysis approach (Petropoulos & Srivastava, 2016) is described. Then the experimental setup is described, which includes defining the input factors, sampling strategy (Morris & Mitchell, 1995; Forrester et al., 2008;

Garg & Stogner, 2017) and output. Finally, the results are analysed in terms of the sensitivity analysis aims: input factor screening (Sarrazin et al., 2016) and input factor ranking (Saltelli et al., 2008) for mean effective stress, temperature, pore pressure and displacement.

Chapter 5 focuses on integrating microseismic modelling with THM modelling to predict microseismic events during the operation of a GDF. Firstly, the model is described. The validated models geometry and thermal load were adjusted to simulate the generic designs for a HLW and advanced gas-cooled reactor (AGR) spent fuel disposal tunnel in lower strength sedimentary rock (RWM, 2016a). Then the microseismic modelling approach (Angus et al., 2010; Angus et al., 2015; Profit et al., 2016) and integration are described. Finally, the results are analysed in terms of the predicted microseismic events and what they may constrain.

Chapter 6 is a discussion of the potential for microseismic monitoring to enhance rock characterization and understanding of the processes occurring in the rock during the operation of a generic GDF. The discussion focusses on the system drivers that will affect the geophysical observations.

The final chapter concludes the work, including a summary of the originality and applications of the work. Finally, further research is discussed.

Chapter 2

Literature review

2.1 Radioactive waste disposal

Radioactive wastes are produced as a by-product from the nuclear power industry, research, defence, medical and other industrial activities. The greatest amount of radioactive waste is produced during the decommissioning of nuclear power facilities (BEIS & NDA, 2016). The standard international practice is to categorize radioactive waste as HLW, intermediate level waste and low level waste (Fayblshenko et al., 2016) using activity (becquerels) concentration (DEFRA et al., 2018).

HLW is stored as heat-producing glass created by vitrification of a liquid by-product from the reprocessing of spent nuclear fuel (Donald, 2010). Spent fuel is not currently classified as waste because it has potential value, however, spent fuel generates significant heat and is typically colocated with HLW in GDF plans (RWM, 2016a). Waste inventories are uncertain because disposal dates and future nuclear activities are undetermined. The forecasted baseline inventory has 7457 m^3 of packaged HLW and 10 363 m^3 of packaged spent fuel (BEIS & NDA, 2016). For comparison, the volume of an Olympic swimming pool is 2500 m^3.

There is a lack of international case studies for GDFs, with most research focussing on URLs. A comprehensive list of operating and discontinued URLs (Table A.1; Gens, 2018) and an international outlook on HLW and spent fuel disposal plans (Table A.2; IAEA, 2018; Fayblshenko et al., 2016) is provided in the Appendix. The proposed host rocks in the plans are broadly categorized using the UK generic concepts: higher strength rock, lower strength sedimentary rock and evaporites.

The focus in this work is lower strength sedimentary rock. Lower strength sedimentary rocks with high clay contents are recognized as high-quality barriers to the migration of radionuclides and chemical contaminants towards the surface environment. The favourable THM properties are:

- very low permeability, restricting flow to diffusion and providing strong transport delays (NDA, 2010b; Grambow, 2016);
- GDF related fractures may self-seal once rehydrated (RWM, 2016a);
- deposited with significant lateral continuity to facilitate large-scale characterization (Norris et al., 2017);
- high retention capacity for many radionuclides and chemical contaminants (Bartl & Czurda, 1991; Chen et al., 2014).

Lower strength sedimentary rocks are typically geologically younger sedimentary rocks with high clay content. Candidates in the UK, considering lithology and depth, are Jurassic shales and mudstones (e.g. Oxford Clay) and Triassic mudstones and siltstones (Watson et al., 2007). Generic UK stratigraphy for lower strength sedimentary host rock is illustrated in Figure 2.1.

Reconstituted clay (e.g. compacted bentonite) is used as the buffer, backfill and sealing material in many engineered barrier concepts (Dixon et al., 2011; García-Siñeriz et al., 2015). Reconstituted clay has low permeability, self-sealing fractures, chemical stability and creates high swelling pressures as it saturates (Tripathy et al., 2004; Sellin & Leupin, 2013). It may be emplaced as pre-compacted blocks and as pellets under pressure (NDA, 2010b).

RWM (2016a; 2016b) provide generic GDF design concepts for higher strength rock, lower strength rock and evaporite environments. The concepts have common features and constraints. The maximum depth of the GDFs is 1000 m. The GDF footprints are approximately 4400 m by 2600 m. The GDFs have one level. The disposal tunnels are grouped together into heat-producing waste modules and negligible heat-producing waste modules. Finally, the heat-producing waste modules are at a minimum 500 m separation from the negligible heat-producing waste modules. Investigations presented in this work use the RWM concept generic designs for lower

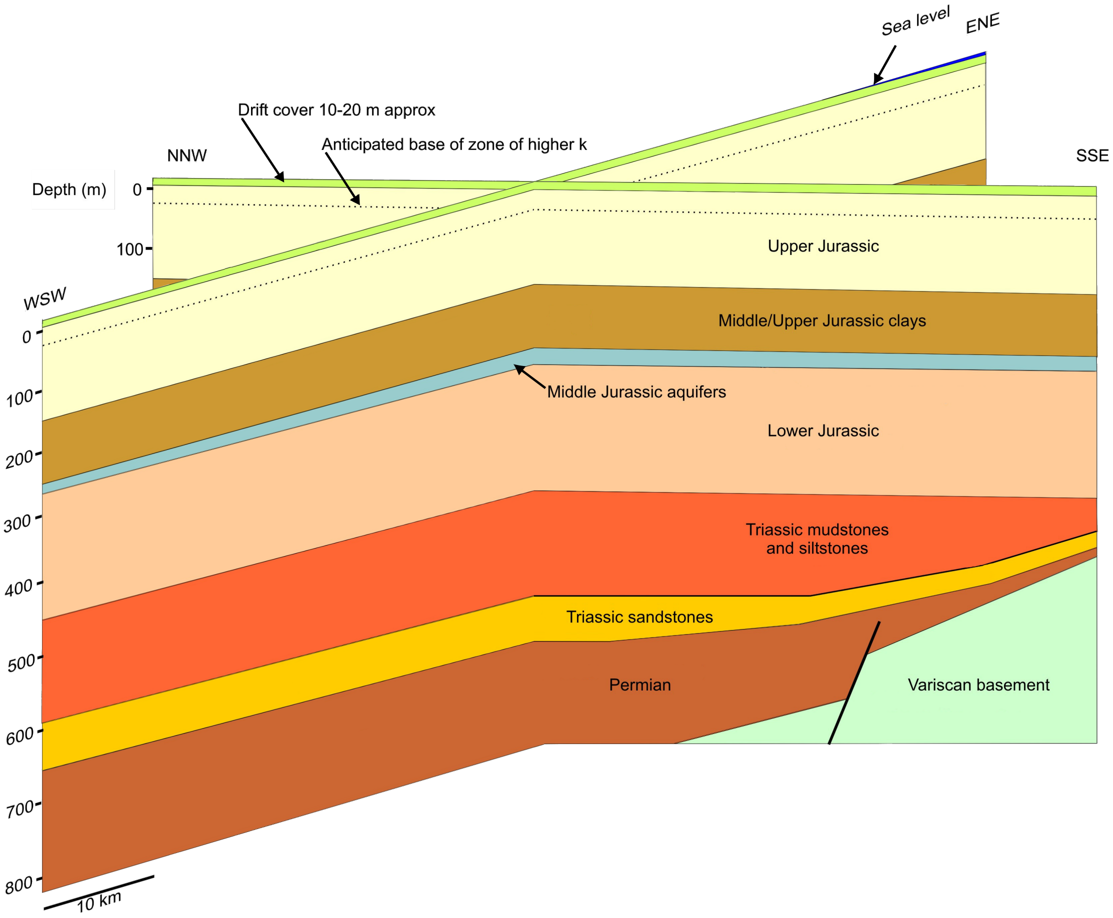

Figure 2.1: Generic lower strength sedimentary host rock environment in the UK (edited from Towler et al., 2008). The GDF could be constructed in the Lower Jurassic or underlying Triassic mudstones and siltstones in this generic scenario.

strength sedimentary host rocks to be consistent with the decision to focus on lower strength sedimentary host rocks in this work (Section 1.2).

Figure 2.2 describes the main events and perturbations expected with a GDF during construction, operation and closure. The operation stage may take up to 100 years (Watson et al., 2009) during which time peak temperatures and pore pressures may be established around the earliest emplaced waste.

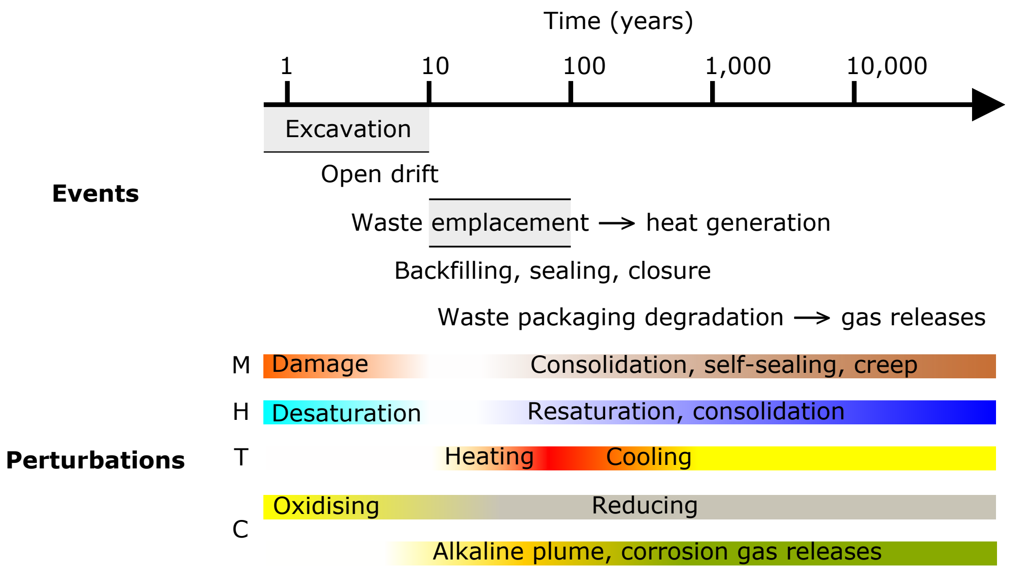

Figure 2.2: Major events and THM-chemical perturbations of the geosphere during the lifetime of a GDF (edited from DECOVALEX, 2014). Year zero represents the start date for construction of the GDF.

2.2 Numerical modelling

Generic concepts can be combined with numerical modelling to forward model scenarios. Numerical modelling can provide one-to-one mapping of specific output values through time and enhance our understanding of processes involved (Jing & Hudson, 2002).

2.2.1 Coupled thermo-hydro-mechanical modelling

Coupled processes are loosely defined as interactions between two or more processes regardless of a feedback loop (Galson & Crawford, 2013). Coupled processes have major significance in assessing the post-closure safety of a GDF (Bond & Watson, 2012). Therefore, coupled THM modelling is an essential tool for understanding the effects of heat-producing wastes in rock.

Investigations presented in this work simulate THM coupled processes which are summarized in Figure 2.3. For recent research into coupled processes involving chemical and biological processes in the context of radioactive waste disposal see,

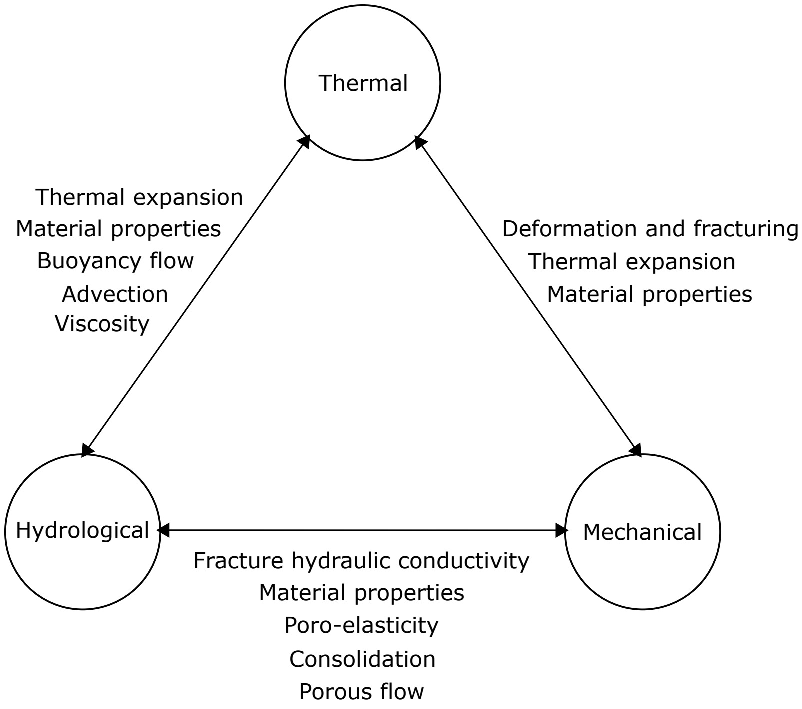

Figure 2.3: Illustrative summary of the THM coupled processes in numerical modelling for rock mechanics.

for example, Liu et al. (2016); Kenney et al. (2017) and Kirby et al. (2018). For an overview of coupled processes near heat-producing waste see Stephansson et al. (2004); Lever et al. (2011); Tsang et al. (2012) and Delage (2017). Recent work by the DECOVALEX and HydroFRAME projects present a high standard of coupled modelling for radioactive waste disposal.

Thermal

The principal thermal driving force is heat-generating waste. Heat transfer will occur predominantly through conduction (Bond & Watson, 2012). Advective heat transfer and buoyancy driven flow are a thermal-hydrological coupling. Concept designs maintain temperature below 100 °C and buoyancy driven flow is unlikely because of low permeability (NDA, 2010a). Advective heat transfer will occur because of pore pressure gradients and will increase in significance with temperature as the fluid becomes less viscous (Hooman & Gurgenci, 2007; Zhao et al., 2008). Heat transfer is satisfactorily calculated in soils and rocks (e.g. ANDRA, 2005; Gens et al., 2007).

Thermal expansion of rock, fluid and backfill materials will increase thermal stresses, strains and pore pressure. The backfill material may dry at early high temperatures, therefore, undergo thermal shrinkage and reduced swelling pressure which would reduce its performance. Drying additionally affects the thermal properties by removing the fluid contribution, therefore, decreasing the bulk thermal heat capacity and increasing the thermal diffusivity (Abu-Hamdeh, 2003). THM simulations of the backfill material and pressures generated are reported in Thomas et al. (2014). Thermal expansion in a crystalline rock may cause microcracking (Siegesmund at al., 2018) which could induce spalling (Hökmark et al., 2010). In a granular material, thermal expansion may reduce the material strength by reducing the mean effective stress as observed in Zhang et al. (2004a). Mean effective stress is reduced because the thermal expansion of the fluid is greater than the grain (Seyedi et al., 2018).

Fine grained soils undergo thermal consolidation, which corresponds to the rearrangement of the grains during heating (Monfared et al., 2011). Drained heating under constant effective stress causes thermo-plastic contraction in normally consolidated clays and thermo-elastic expansion in overconsolidated clays (Hueckel & Baldi, 1990). Claystones thermo-elastic expansion changes to thermo-plastic contraction at the maximum temperature previously experienced, indicating thermal hardening (Belmokhtar et al., 2017). In the context of potential radioactive wate disposal host rocks, lower strength sedimentary rocks are typically overconsolidated clays with a range of maximum temperatures previously experienced depending on burial history.

Hydrological

Radionuclide migration from a GDF is dependent on groundwater flow and may be facilitated by coupled biological processes (Altmann, 2008) and mechanical processes, e.g. colloids (Möri et al., 2003). Furthermore, groundwater flow affects waste package corrosion and other gas-generating reactions (Galson & Crawford, 2013).

For simplification, models presented in this work are fully saturated with a single fluid phase. The fully saturated with a single fluid phase assumption is accurate for radioactive waste disposal away from ventillated excavations (Garitte et al., 2017) and is typical in THM modelling (Cui et al., 2018). Models presented in this work simulate host rock permeability, hydraulic gradients and temperature-dependent viscosity which are the main parameters controlling groundwater flow rates (Zhang et al., 2007a). The hydrological system drivers are construction-related stress perturbations, operation stage ventilation, resaturation and thermal expansion.

The operational period and groundwater flow rates determine the degree of host rock desaturation. Resaturation of the GDF post-closure and formation pressure recovery are distinct issues. Resaturation of a higher strength host rock GDF depends on the connectivity and hydraulic conductivity of the fracture network and may take decades (Watson et al. 2009). Resaturation of a lower strength sedimentary host rock GDF will be slower and may take up to a 100,000 years (NAGRA, 2002; Davies & Bernier, 2005). Formation pressure recovery will be perturbed beyond the resaturation of the GDF and is further perturbed by thermal contraction during cooling.

The thermal expansion coefficient of water (Spang, 2002) is higher than clay (McTigue, 1986) and heat is transferred faster than water in low permeability rocks. Therefore, heating causes thermal pressurisation which also depends on the compressibility (Verruijt, 2013). Thermo-consolidation experiments show the increased pore pressure is then dissipated because the fluid viscosity decreases with an increase in temperature whilst the permeability is unaffected (Delage et al., 2000). The fluid viscosity decreases from 1.00×10^{-9} Pa.s at 20 °C to 2.67×10^{-10} Pa.s at 100 °C. Modelling thermal pressurisation in clay rock requires THM calculations in which the material is poro-elastic (Gens et al., 2007).

Mechanical

The depth, spacing and orientation of excavations in GDF concepts consider rock mass characteristics and anisotropic in situ stress (RWM, 2016a). Disposal tunnel alignment will depend on the local stress state. Excavations perturb the stress field by dynamically creating free surfaces. The stress perturbation often causes rock mass failure creating an excavation damage zone.

The behaviour of the excavation damage zone in lower strength sedimentary rocks has been reported in several projects (e.g. TIMODAZ; Li, 2013). The excavation damage zone may propagate during the operation stage of a GDF as the host rock desaturates (Galson & Crawford, 2013). The excavation damage zone in indurated clays may self-seal, however, this is complex and uncertain (Davies & Bernier 2005). URL experiments are advancing knowledge in this area (e.g. Aranyossy et al., 2008). Simulating the excavation damage zone is most significant in higher strength host rocks (Winpenny et al., 2012). Finite element method (FEM) with an elasto-plastic material model is appropriate for lower strength sedimentary host rocks (EA, 2009).

Elastic parameters are temperature independent (Mohajerani et al., 2014; Menaceur et al., 2015). Whereas, the yield envelope contracts (i.e. weakening) with temperature (Cekerevac & Laloui, 2004). The strength decreases more in undrained conditions than in drained conditions because there is an effective stress drop as pore pressure increases (Hueckel & Borsetto, 1990). Increasing temperature above the maximum temperature previously experienced causes thermal consolidation and hardening which counter-balances the weakening. Volumetric creep is enhanced by temperature (Belmokhtar et al., 2017) and shear planes can be reactivated by increasing temperature (Armand et al., 2014; Menaceur et al., 2016). However, shear planes have no affect on permeability due to the excellent self-sealing properties of hydrating layered clay minerals (Menaceur et al., 2016).

In numerical modelling, constitutive models describe the material response to loading. In rock mechanics, the term constitutive models typically refers to strength models which relate the deviatoric stress to deviatoric strain and failure criterions to identify the onset and evolution of material failure (Zhang et al., 2016). The most common constitutive model in rock mechanics is the Mohr-Coulomb model which is defined in normal stress–shear stress space. The Mohr-Coulomb parameters (friction and cohesion) have clear physical meaning and can be determined in most geotechnical laboratories.

The Mohr-Coulomb model does not consider the influence of the intermediate principal stress on the material strength. Therefore, it is most appropriate for materials in which the compressive strength far exceeds the tensile strength, e.g. fracture behaviour and hard intact rock (Jaeger et al., 2007). However, critical state theory in mean effective stress (p')–deviatoric stress (q) space shows that the intermediate principal stress affects soil strength (Wood, 1990). Furthermore, constitutive models that consider the intermediate principal stress fit experimental data from triaxial tests on lower strength rocks (Crook et al., 2003; Rockfield Software Limited, 2013a).

The most common constitutive models for lower strength rocks are Drucker-Prager (Drucker and Prager, 1952) and (modified) Cam-Clay (Roscoe & Burland, 1968; Wood, 1990). The Cam-Clay model is often used in conjunction with porous elasticity, as opposed to linear elasticity. Porous elasticity introduces a logarithmic relationship between stress and strain and uses the κ material parameter from consolidation tests. Poro-elastic-plastic behaviour is typically observed for lower strength rocks (e.g. Zhang et al., 2004b). The SR3 model is similar to Cam-Clay and additionally includes cap-plasticity which simulates pore collapse at high mean effective stress (Crook et al., 2003).

2.2.2 Numerical modelling methods

Numerical modelling methods are traditionally categorized as continuum or discontinuum (Figure 2.4). Hybrid methods, however, demonstrate that continuum and discrete methods are not mutually exclusive (Lorig & Brady, 1982). They are typically a combination of FEM and discrete element method (DEM) which can capture both strain within blocks and discrete component movement (e.g. Xiang et al., 2009; Latham et al., 2013).

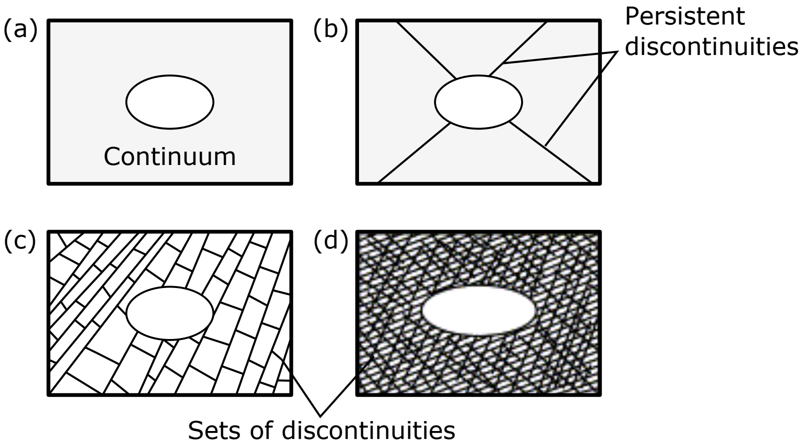

Figure 2.4: Numerical methods for an excavation in a rock mass (edited from Jing, 2003): (a) continuum method; (b) continuum with fracture elements; (c) discrete method; and (d) continuum method with equivalent properties.

Continuum methods use the mathematical assumption of an infinitesimal element, implying an infinite number of components (Jing & Hudson, 2002). This is approximated by sub-dividing the domain into a finite number of elements. The collective elements are called the mesh and the vertices of the elements are called nodes. The nodes maintain original contacts during deformation. Each element must satisfy the governing differential equations which are a mathematical approximation of the system behaviour (Jing & Hudson, 2002). FEM is a continuum method. FEM element behaviour is described by local algebraic equations that are approximations of the governing partial differential equations, calculated by polynomial trial functions (Munjiza, 2004). Local algebraic equations and their topological relationship with elements form a global system that can be solved using the initial and boundary conditions. The number of nodes is proportional to the number of degrees of freedom, therefore, increasing the number of nodes will increase the model computation time (Paszyński et al., 2010). Finite difference methods discretize the domain with a grid which is easy to implement in simple geometries. FEM is more versatile for handling material heterogeneity, non-linearity and boundary conditions (Jing, 2003).

DEM describes a system of well-defined finite components, where the behaviour of such components can be independently treated mathematically (Jing & Stephansson, 2007). Global system behaviour is calculated through interrelations between the components. In geomechanics, a discrete fracture network separates the domain into an assemblage of intact blocks between connected fractures (Cacas et al., 1990; Fu et al., 2012). Initial and boundary conditions, and contact detection and contact conditions with constitutive models for point contacts and fractures are applied. The solution uses rigid body motion (Hart et al., 1988), which does not produce strains within the blocks. DEM may allow for fracture initiation and propagation, detachment, rotation and large displacements (Guo et al., 2017).

Continuum and discontinuum methods are relative and problem specific concepts which require an understanding of discontinuities at different scales in the rock mass (Latha & Garaga, 2012). The discrete method is not always appropriate for discrete systems because representing many small elements individually is not mathematically possible or necessary (Jing, 2003). Geomechanical software most commonly uses the FEM (e.g. Hawkins et al., 2007; Herwanger et al., 2009; De

Gennaro et al., 2010) because it is flexibile and relatively computationally efficient. The DEM has also been used successfully (e.g. Alassi, 2008; Thomas et al., 2018) and is particularly appropriate for fractured, higher strength rock masses.

Simulating fluid flow through porous rock has been advanced primarily in hydrocarbon reservoir simulation. Iske & Randen (2006) described different numerical techniques for hydrocarbon reservoir simulation. Reservoir simulation software most commonly use the finite difference method (e.g. Kasiri & Bashiri, 2010) because of ease of application to simple 3D geometries and compatibility with multiphase (e.g. water and gas) flow problems (Zhou et al., 2014). However, FEM and finite volume method have been successfully applied to modelling fluid dynamics and production scenarios (e.g. Jackson et al., 2015). Fluid flow is particularly difficult in DEM because of the change in flow mechanism between porous flow (Darcy fluid flux) and laminar fracture flow (Salimzadeh et al., 2017). Heat transfer is similar to fluid flux in that it is complicated by discrete contact (Joulin et al., 2017). Therefore, it is easier to couple THM processes in FEM than DEM.

Early hydro-mechanical models used a modular approach to coupling pre-existing geomechanical and reservoir software. A modular approach treats the different fields individually and couples them by passing information between them (Angus et al., 2015). Increasing demand for coupled models driven by high temperature high pressure reservoirs, CO_2 storage (e.g. Görke et al., 2011) radioactive waste disposal (e.g. Nowak et al., 2011), hydraulic fracturing and geothermal energy (e.g. Kolditz, 1995; Watanabe, 2012) has seen a growth in standalone software providing geomechanical, fluid flow and thermal simulation. Settari & Walters (2001) and Dean et al. (2006) discuss modular and fully integrated approaches to coupling geomechanical and reservoir modelling. A fully integrated approach unifies the physical equations into one formulation. A modular approach may still be applied within standalone software allowing a preferred combination of explicit solvers for geomechanical simulations and implicit solvers for fluid flow and thermal simulations (Profit et al., 2016).

2.3 Rock mass uncertainty

URLs provide access to the rock mass in situ and resultantly tend to be situated in the most characterized underground rock masses in the world (e.g. Jalali et al., 2017). Models presented in this work use Opalinus Clay characterized at the Mont Terri Rock Laboratory because quality data was obtained for a benchmark test to validate the modelling. Opalinus Clay is an analogue for a generic lower strength sedimentary rock (Towler et al., 2008). Opalinus Clay is over-consolidated, low porosity, and clay-rich (Bock, 2001), similar to Callovo-Oxfordian Clay (Yven et al., 2007).

2.3.1 Rock mass characterization

Geological surveys were carried out at the Mont Terri Rock Laboratory and observed the Opalinus Clay as homogeneous, weakly disturbed and not intersected by faults (Nussbaum et al., 2004a; 2004b). Triaxial tests (Figure 2.5) use different confining pressures to calculate the failure envelope. For example, the modified Cam-Clay model (Roscoe & Burland, 1968) can be calibrated using deviatoric stress versus strain curves from triaxial tests. The hardening parameters are used to fit the model to the volume strain which is critical for modelling pore pressures. Brazilian disc tests calculate indirect tensile strength. This is typically scaled to a greater true tensile strength (Matthew & Diederichs, 2013). Scaling must be taken into account when applying laboratory characterizations to in situ rock mass (e.g. Stavrou & Murphy, 2018).

Characterizing the anisotropic in situ stress state is difficult and uncertain. The vertical stress can be estimated as an overburden pressure. At the Mont Terri Rock Laboratory, two in situ stress tensors were derived from borehole slotter and undercoring methods (Nussbaum et al., 2014). These were used in numerical modelling to predict the observed borehole breakouts (Martin & Lanyon, 2003). Furthermore, hydraulic fracturing tests constrained the minimum principal stress (Evans et al., 1999). The determined in situ stress state is dependent on the lithology and will be different in formations with different strength.

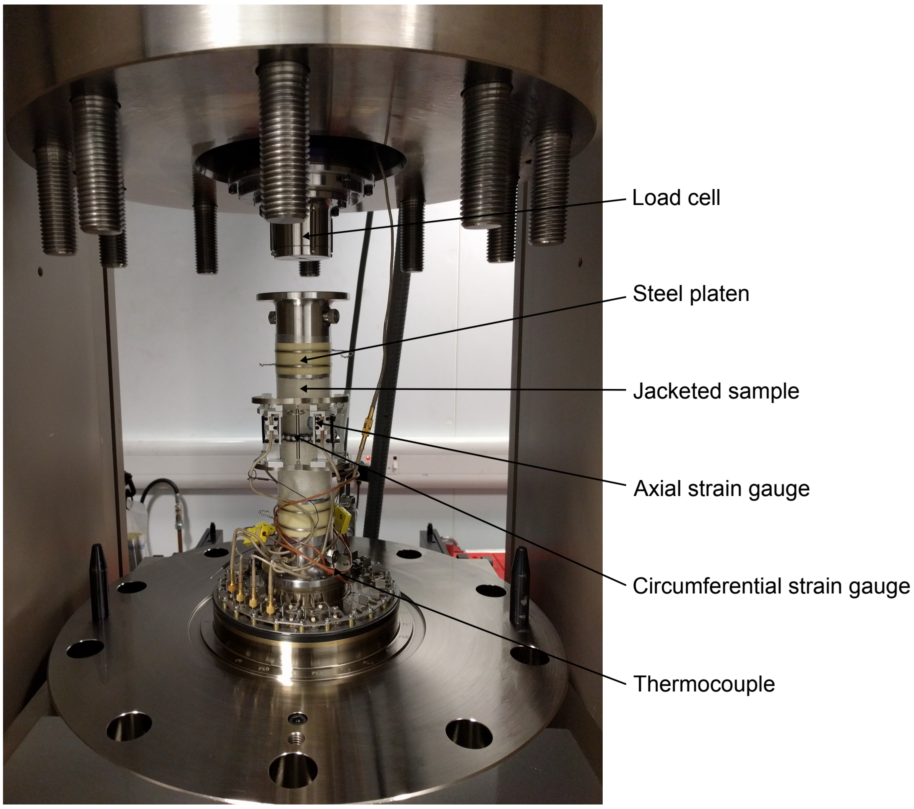

Figure 2.5: Photograph of a prepared sample fitted with axial and circumferential strain gauges ready for triaxial testing at the BGS (from Woodman et al., 2017).

2.3.2 Sensitivity analysis

Saltelli et al. (2019) presents a damning analysis of the quality of sensitivity analyses in applied sciences, which is particularly damning for earth sciences. Whilst earth sciences produce the second highest density of papers mentioning sensitivity analysis, it was found to have the second lowest ratio of global sensitivity analyses. The former is unsurprising because earth sciences are model-intensive subjects. However, the latter is of particular concern because the discipline relies heavily on large computer models and large-budget models are used for making significant decisions. This concern is being discussed for climate models in policy-making (Saltelli et al., 2013) but also requires addressing for radioactive waste disposal, not least because the safety case requires uncertainty analyses (Kozak, 2017; Hudson et al., 2017).

Despite being well characterized at test sites there is still significant uncertainty reported in rock properties (Bock, 2001). Modelling and monitoring for reducing uncertainty in aspects of geological disposal of radioactive waste is a paramount aim for the community (IAEA, 2011b; NDA, 2010a). Gens et al. (2007) investigate this by running additional model evaluations with one-at-a-time changes to end-member values within the uncertainty for selected 'important' input factors. However, one-at-a-time approaches are flawed because coupled models are complex and highly nonlinear. There has been a lack of investigation into the uncertainty in rock properties beyond this, which is diagnostic of a broader lack of investigation into the uncertainty in rock properties in geomechanical models.

Notable cutting-edge work on the uncertainty in rock properties has been presented in Jobmann et al., 2016. The authors use the software tool optiSLang (optiSLang, 2010) for sensitivity analysis and optimization that automatically fit input factors and analyse the importance of individual input factors for the general system development. However, no results are presented towards the robustness or validity of the sensitivity analysis and the sample size of 80 for 29 input factors is an order of magnitude less than the recommended values for similar aims (Sarrazin et al., 2016).

The low number of model evaluations is because THM coupled finite element models are computationally expensive. The high number of input factors for a geomechanical model are because of the THM coupling. This is addressed in Jobmann et al. (2016) by removing input factors that have a negligible influence during the analysis. Here the authors neglect input factor screening as a distinct topic with more appropriate sensitivity analysis approaches available. Input factor screening must be achieved using global sensitivity analysis methods that account for input factor interactions which rules out common approaches for input factor ranking (Saltelli et al., 2008).

Input factor screening is identifying input factors that have negligible influence on the model output (Sarrazin et al., 2016). If uncertainty in an input factor has negligible influence on the model output, the input factor can be fixed to any value within its uncertainty range (e.g. Vanuytrecht et al., 2014). Screening can inform uncertainty reduction by identifying parameters which do not need to be characterized further, and increase uncertainty and sensitivity analysis efficiency by decreasing the number of uncertain parameters.

Global sensitivity analyses investigate the whole input factor uncertainty space using Monte Carlo style simulation (Iooss & Lemaitre, 2015). It provides a coherent mathematical methodology to determine important input factors and their influence on the model output. The variance-based sensitivity analysis total effects indices and the Elementary Effects Test (EET) indices account for input factor interactions (Saltelli et al., 2008). EET can provide a good approximation of the screening given by variance-based sensitivity analysis for fewer model evaluations (Sarrazin et al., 2016). Petropoulos & Srivastava (2016) present a credible, computationally efficient multi-method global sensitivity analysis approach for ranking input factors based on their influence. Three approaches measure the sensitivity indices differently and presented together provide a more credible input factor ranking result. The approach is computationally efficient because the three approaches use the same generic input-output dataset (McKay et al., 1979; Johnson et al., 1990; Petropoulos & Srivastava, 2016) and so no additional model evaluations are required.

Global sensitivity analysis methods have not been applied to coupled THM models with an assessment of the number of evaluations required to achieve convergence for any given aim. Furthermore, screening thresholds have not been investigated for any outputs.

2.4 Seismic monitoring methods

The GDF site will undergo extensive characterization and monitoring during construction, operation and closure (RWM 2016a). There is no commitment to monitor the GDF site post-closure (Allan & Nuttall, 1997; NEA & RWM, 2010). Characterizing large areas (e.g. 4400 m by 2600 m for a GDF) and accounting for spatial heterogeneity requires extensive sampling (Fjaer & Kristiansen, 2009) and laboratory testing which is expensive (Herwanger & Horne, 2009). Remote sensing is a largely non-intrusive and cost effective way of providing 3D subsurface information (BGS, 2015).

2.4.1 Microseismic monitoring

Microseismic monitoring is a passive remote sensing technique that uses geophones to record microseismic events. Unlike active seismic monitoring which uses a source, microseismic monitoring provides a continuous (4D) record of seismicity. The geophones convert velocity from microseismic events into voltage. The waves (deviation of voltage from the base line) recorded at geophones in different locations are analysed for the spatial, temporal and mechanism data of the microseismic events (Onajite, 2013).

The seismic moment, M_0, can be calculated using Equation 2.1.

$$M_0 = muA \tag{2.1}$$

where m is the failure surface shear modulus, u is the total slip and A is the failure surface area. Microseismic modelling with continuum models cannot estimate true seismic moment because the failure surface is not modelled. Other approaches have been successful by estimating the pseudo scalar seismic moment (Silver & Jordan, 1982) based on the differential stress tensor (Angus et al., 2010).

Monitoring of microseismic events is used to understand fracture initiation and propagation for mining-induced, producing reservoir-induced (e.g. Angus et al., 2010) and CO_2 injection-induced microseismicity applications (Figure 2.6). Microseismic monitoring has been used during mechanical disturbances to monitor excavation damage zones (Lockner, 1993) and predict rock bursts (e.g. Dou et al., 2009; Wang et al., 2017). Microseismic events are found to cluster around fractures and to peak in abundance and magnitude before rock bursts. Gonidec et al. (2014) used microseismic monitoring during an excavation in the clay-rich facies of Opalinus Clay at the Mont Terri Rock Laboratory. Ahead of the excavation front, double-couple seismic sources were interpreted as shear movement along pre-existing features oriented sub-parallel to the major principal stress.

Microseismic monitoring might be used to monitor the construction and operation of a radioactive waste disposal facility for which there are precedents from other industries. However, there is no precedent for using microseismic monitoring during backfilling, heating, resaturation and backfill swelling.

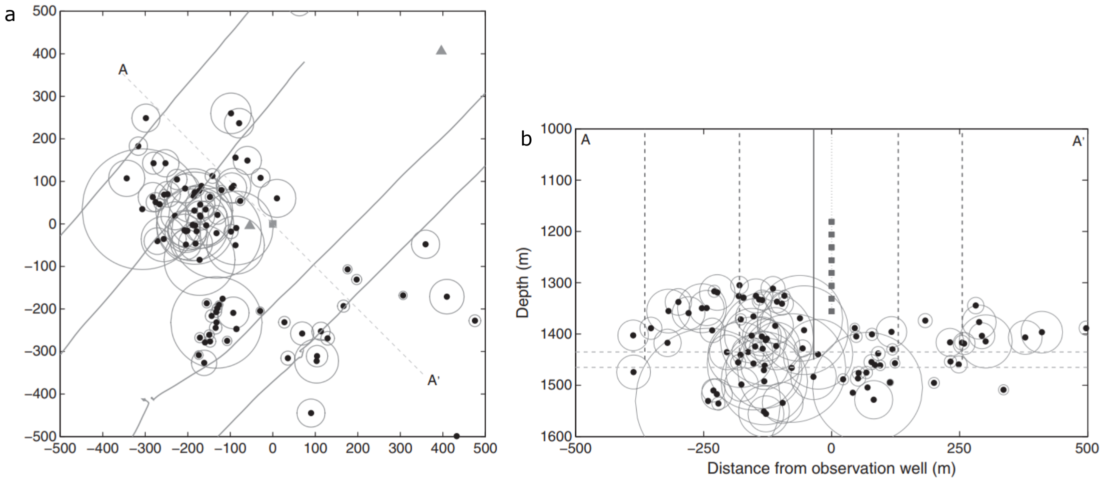

Figure 2.6: Microseismic event location in (a) map view and (b) cross-section view after CO_2 injection (from Verdon et al., 2011). Ellipses are 95% confidence limits.

2.5 Summary

Microseismic methods exist for characterizing and monitoring a GDF during construction and operation for which there are industry precedents and current research. However, there is no precedent for using these methods to monitor heat-producing waste. Generic concepts and analogue materials can be used to explore potential GDF scenarios before they exist. Sensitivity and uncertainty analyses provide a statistical approach to exploring input factor spaces to provide an understanding of the potential to use microseismic monitoring methods after waste emplacement. For the results to be meaningful, the model must be a good representation of reality. Data from in situ experiments at URLs provide an opportunity to benchmark models.

Chapter 3

Numerical modelling theory and validation

3.1 Introduction

This chapter documents the creation and benchmarking of a numerical model. The model simulates the in situ heater experiment, HE-D, performed at the Mont Terri Rock Laboratory (Wileveau & Rothfuchs, 2003; Garitte et al., 2017). Heaters were emplaced into a horizontal borehole in Opalinus Clay at 350 m depth (Figure 3.1). Sensors surrounding the heaters recorded temperature, pore pressure and displacement over time. The Opalinus Clay in situ heater experiment is ideal because it is analogous to heat-producing radioactive waste in lower strength sedimentary rock and it is supported by data that can be used in numerical modelling benchmark tests.

Several publications present simulations of the HE-D experiment and all use a THM model (Garitte et al., 2017). THM models are required to capture the coupled processes occurring in the solid and fluid components of the rock during heating. The fluid component is important in lower strength sedimentary rocks because of poroelasticity (Verruijt, 2013). Specifically, thermally increased pore pressure reducing the effective stress and a tendancy towards failure at low mean effective stress (Cosgrove & Hudson, 2016).

The HE-D experiment was simulated by creating and analysing a THM model using ELFEN. ELFEN has a modular approach to coupling with multiple fields including mechanical, single phase porous flow and thermal. The thermal and flow simulations are performed within a fully coupled implicit solver and the geomech-

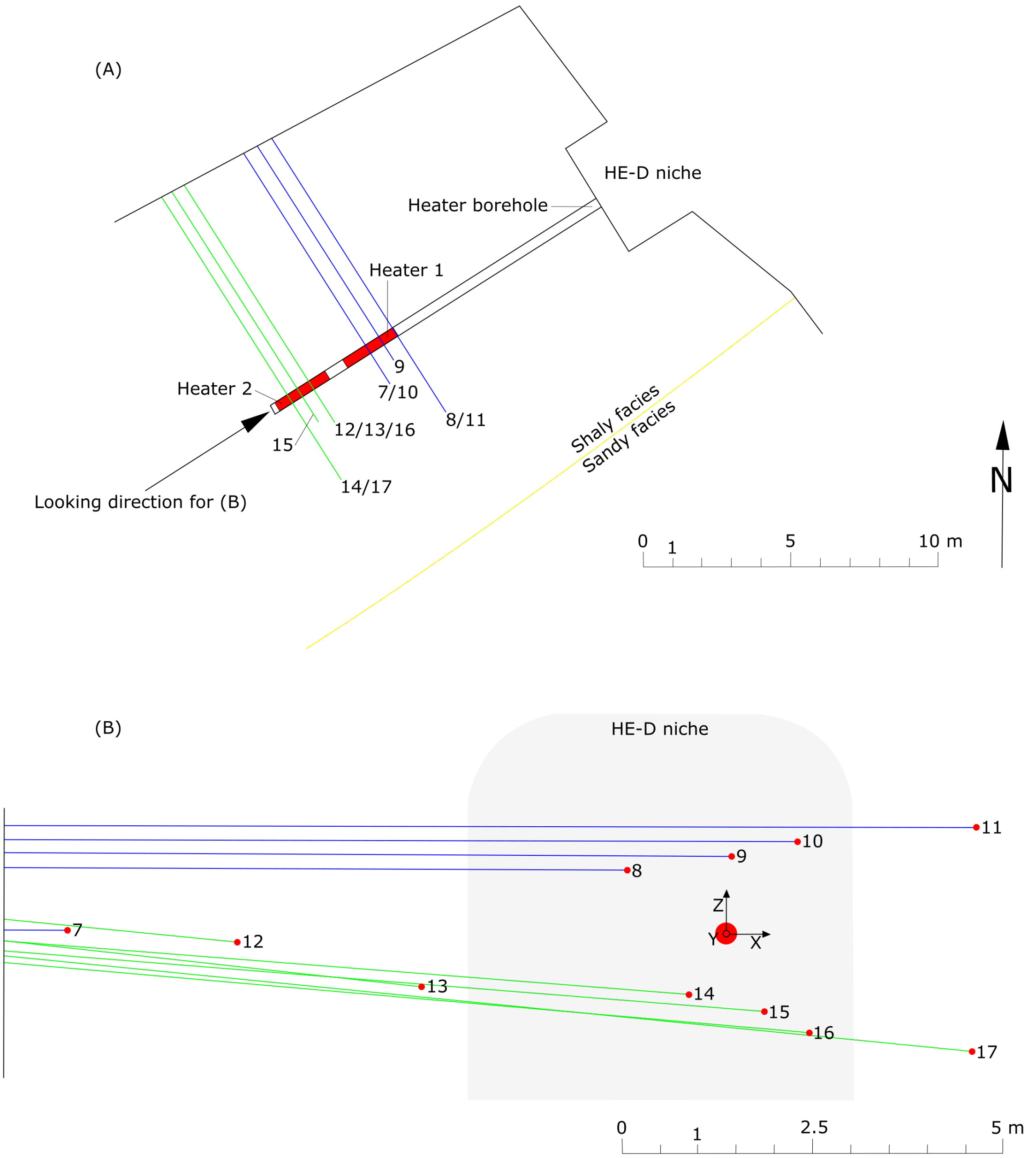

Figure 3.1: Layout of the HE-D experiment with heater and measuring boreholes (from Zhang et al., 2007a). (a) Plan view and (b) flattened cross-section view. Six measuring boreholes are not depicted because they did not contribute data to this study.

anical simulations are performed within an explicit solver. The implicit and explicit solvers are iteratively coupled using a two-way scheme mediated by a message passing interface. Iterative or loosely coupled flow-deformation algorithms maintain the sophistication of commercial flow and geomechanical simulation algorithms without being overly computationally expensive (Rutqvist et al., 2002; Settari & Sen, 2007). ELFEN was selected because it is commercial software that has been verified at multiple scales, from laboratory to sedimentary basin and from milliseconds to millions of years (Hamdi et al., 2014; Wang et al., 2019).

3DEC software (Itasca Consulting Group, Inc.) was also considered for modelling. 3DEC can perform thermo-mechanical simulations and THM simulations with the fluid restricted to the fractures (Huang et al., 2018). However, 3DEC does not simulate porous flow or pore pressure within the intact rock, which is crucial for THM processes in lower strength sedimentary rock (Section 2.2.1).

Each stage of model building is discussed in detail in this chapter and the results are compared with the HE-D experiment results for validation. Additional models were used to determine appropriate input factors relating to the Opalinus Clay material properties, if they were not determined for the HE-D test site.

3.2 Multifield modelling theoretical formulation

The following is a summary of the applicable theory from the ELFEN manuals (Rockfield Software Limited, 2013a; 2013b). The following assumptions were made for the THM coupled calculations. Heat transfer mechanisms are conduction (Fourier's law) through porous medium and advection of liquid water. Fluid transport is controlled by porous flow (Darcy's law). A THM model is used for the description of the mechanical behaviour of the clay rock with the main features of thermal expansion and poroelasticity. The clay rock is assumed to be homogeneous and isotropic because of the model geometry constraints. These assumptions are consistent with the previous publications on simulating the HE-D experiment (Wang & Kolditz, 2013; Garitte et al., 2017).

3.2.1 Thermal field

The governing equation for heat transfer is expressed in Equation 3.1 as the sum of the conduction and advection terms.

$$(\rho c)_b \frac{\partial T}{\partial t} = div(\kappa_b \nabla T) + \rho_f c_f q_f . \nabla T \tag{3.1}$$

where ρ is density, c is specific heat capacity, T is temperature, t is time, κ is thermal conductivity, q_f is Darcy fluid flux and the subscripts b and f denote bulk and fluid values.

The bulk volumetric heat capacity, $(\rho c)_b$, is calculated using Equation 3.2. The bulk thermal conductivity, κ_b, for the conduction term is calculated using Equation 3.3. The Darcy fluid flux for the advection term is calculated using Equation 3.4.

$$(\rho c)_b = \rho_s c_s (1 - \phi) + \rho_f c_f \phi \tag{3.2}$$

$$\kappa_b = \kappa_s (1 - \phi) + \kappa_f \phi \tag{3.3}$$

$$q_f = -\frac{k(\phi)}{\mu_f} (\nabla p_f - \rho_f g) \tag{3.4}$$

where ϕ is porosity, $k(\phi)$ is porosity dependent permeability, μ_f is viscosity, p_f is pore pressure, g is acceleration due to gravity and s denotes solid grain values.

Conduction is the primary heat transfer mechanism. Advection may be significant if alternative fluid migration drivers exist or in high permeability fracture networks (Fraser Harris et al., 2015). Convection would require solving in conjunction with the Navier-Stokes equation to take into account any pressure or density changes in the fluid (Rockfield Software Limited, 2013b). This is not implemented in ELFEN. Therefore, porous flow and advection are driven by pore pressure gradients resulting from thermal expansion/contraction, pore compaction/dilation and groundwater pressure gradients. This is appropriate when pore pressure is dominant over density for pore fluid movement.

3.2.2 Porous flow field

The governing equation for the fluid flow is expressed in Equation 3.5.

$$div(\frac{k(\phi)}{\mu_f(T)}(\nabla p_f - \rho_f(T)g)) = (\frac{\phi}{K_f} + \frac{(\alpha(\phi)-\phi)}{K_s})\frac{\partial p_f}{\partial t} - \frac{\alpha(\phi)}{1-\phi}\frac{\partial \phi}{\partial t} + \alpha_{sf}(\phi, T)\frac{\partial T}{\partial t} \tag{3.5}$$

where K is stiffness, α is the Biot coefficient and α_{sf} is thermal expansion coefficient. The Biot coefficient is the ratio of fluid volume change to bulk volume change with a drained condition (Müller & Sahay, 2016).

The final term is the aquathermal pressure which is dependent on the temperature from the thermal field as a function of the thermal expansion coefficients. The other terms are dependent on the geomechanical field and consolidation properties. The volume strain rate term, $-\frac{\alpha(\phi)}{1-\phi}\frac{\partial \phi}{\partial t}$, defines the effective rate of pore volume change due to either compaction or dilation. Volume strain, ϵ_v, is a function of effective stress, σ', which is defined in Equation 3.6. In this work negative values denote compressive stress.

$$\sigma' = \sigma + \alpha(\phi)mp_f \tag{3.6}$$

where σ is the stress tensor and m is the vector $\{111000\}^T$ where the superscript T denotes transpose.

Permeability is discussed in relation to a fully saturated porous medium with a single fluid phase (i.e. intrinsic permeability). The permeability, k, is a function of porosity (Figure 3.2) as defined by the Kozeny-Carman parameters, k_0, n and m, in Equation 3.7 (Kozeny, 1927; Carman, 1937). Porosity dependent permeability is consistent with other modelling approaches for the HE-D experiment (Wang & Kolditz, 2013; Garitte et al., 2017). Clastic rocks typically have 2 to 10 times higher bedding parallel permeability (Hantschel & Kauerauf, 2009).

$$k = k_0\left(\frac{\phi^n}{(1-\phi)^m}\right) \tag{3.7}$$

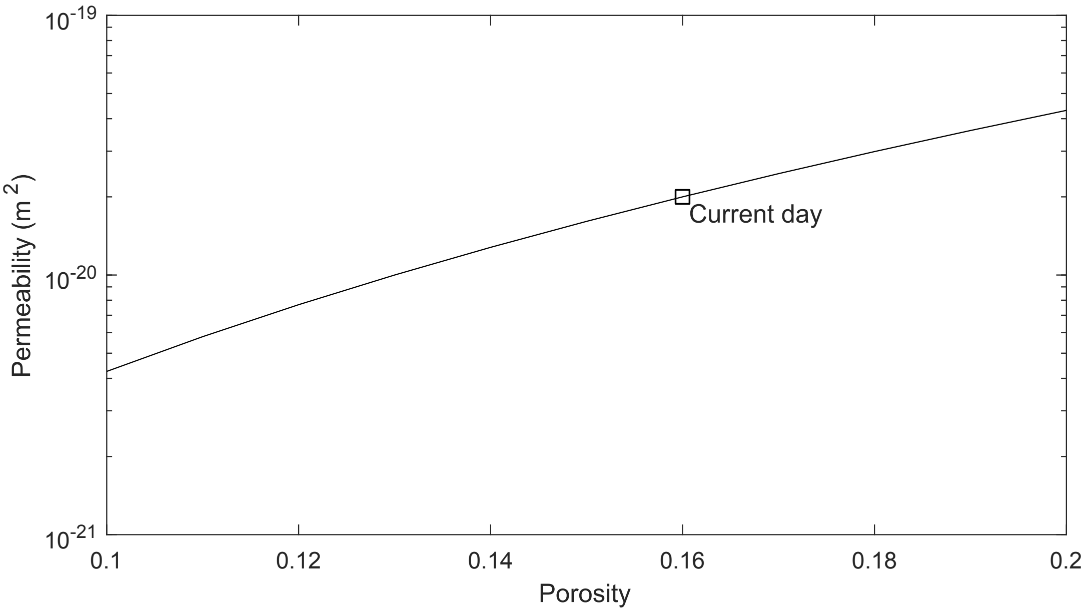

Figure 3.2: Non-linear dependence of intrinsic permeability on porosity according to the Kozeny-Carman model. The curve uses Kozeny-Carman parameters, $k_0 = 1.67 \times 10^{-19}$, $n = 3$ and $m = 2$. These calculate the current day porosity, 0.16, and permeability, 2.00×10^{-20} m^2, determined for Opalinus Clay in the HE-D test site.

3.2.3 Geomechanical field

Equation 3.8 is the linear momentum balance equation (Rockfield Software Limited, 2013a).

$$L^T \sigma' + \rho_b g = 0 \tag{3.8}$$

where L is the standard continuum mechanics differential operator and bulk density, ρ_b, is calculated using Equation 3.9.

$$\rho_b = \rho_s(1 - \phi) + \rho_f \phi \tag{3.9}$$

An empirical poro-elastic model defines nonlinear Young's modulus, E (Equation 3.10), as a function of mean effective stress, p' (Figure 3.3). Mean effective stress is defined in Equation 3.11. When the minimum effective stress, σ_3', is tensile, the mean effective stress is omitted from Equation 3.10.

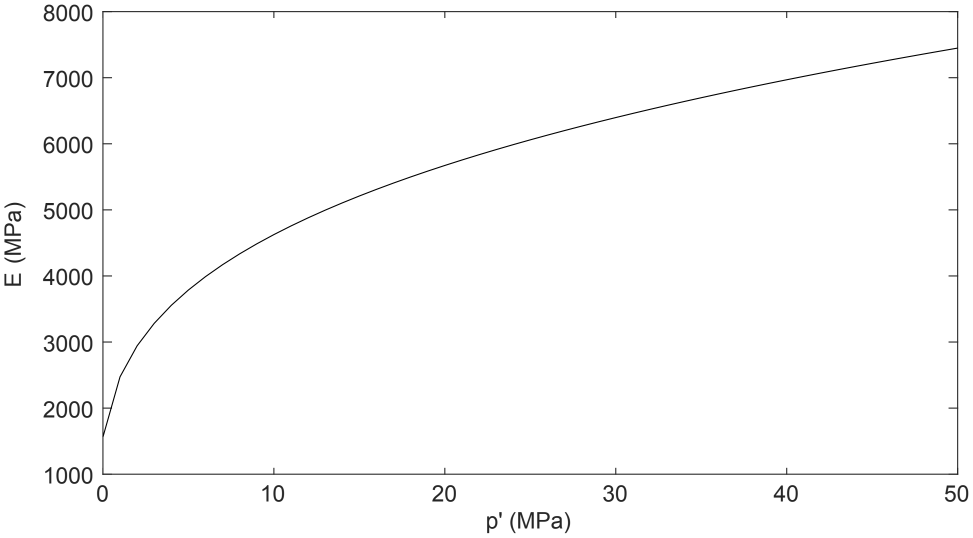

Figure 3.3: Nonlinear dependence of Young's modulus on mean effective stress. The curve uses E_{ref} = 40 MPa, A = 0.2758, B = 0.2758, n = 0.3 and c = -2. The power law relationship has been observed in laboratory testing on Opalinus Clay samples cut normal to bedding (Hertzsch & Graesle, 2015).

$$E = E_{ref}\left[\frac{p' + A}{B}\right]^n \phi^c \tag{3.10}$$

$$p' = (\sigma'_1 + \sigma'_2 + \sigma'_3)/3. \tag{3.11}$$

where E_{ref} is the reference Young's modulus, A and B are constants used to prevent problems near zero values of σ'_3, n and c are optimized material constants that fit the Young's modulus pressure curves to data and subscripts 1, 2 and 3 refer to the principal stresses. The data may be ultra-sonic velocity-stress core measurements (Angus & Price, 2016). The principal stress directions and magnitudes (for Equation 3.11) are given by the eigenvalues and eigenvectors of the effective stress tensor, σ' (Jaeger et al., 2007).

The stress at which the rock will begin to deform plastically is defined by the state boundary surface (also known as the yield envelope). Investigations presented in this work use the Soft Rock model (SR3) state boundary surface proposed by Crook et al. (2003) for weakly cemented rock and defined by Equation 3.12. The surface is defined in p'-q space, where p' is mean effective stress (Equation 3.11) and q is deviatoric stress (Equation 3.13). The surface (Figure 3.4) intersects the p' axis in both tension, p_t (tensile intercept), and compression, p_c (pre-consolidation pressure, also known as compressive intercept of the yield surface with the hydrostatic axis).

$$\phi(\sigma\epsilon_v^p) = g(\theta, p')q + (p' - p_t)\tan\beta\left(\frac{p' - p_c}{p_t - p_c}\right)^{\frac{1}{n}} \tag{3.12}$$

$$q = \sigma_1' - \sigma_3'. \tag{3.13}$$

where ϵ_v^p is the volumetric plastic strain, $g(\theta, p)$ is the deviatoric plane correction term that controls the shape of the yield surface in the deviatoric plane, θ is the lode angle, β and n are material constants. Typically $g(\theta, p) = 1$ so the strength in compression is the strength calibrated using triaxial compression tests (Crook et al., 2008).

The SR3 yield surface is non-associated with a plastic flow, $\dot{\epsilon}^p$, rule defined in Equation 3.14.

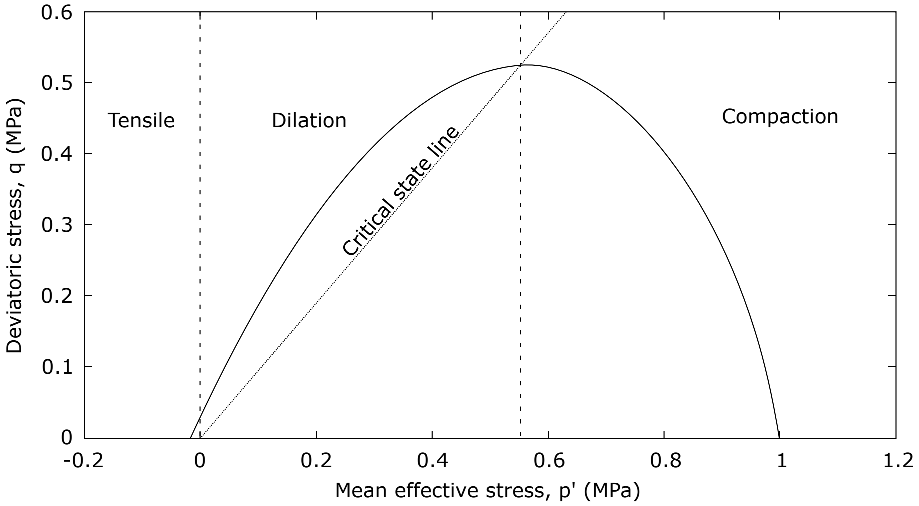

Figure 3.4: Soft rock (SR3) yield surface, where p_c = 1 MPa, p_t = -0.018 MPa, β = 60°, n = 1.3. The tensile, shear and compaction sections indicate the yield type. Hardening changes the size of the smooth, three-invariant surface along the critical state line without changing the shape (Crook et al., 2003).

$$\dot{\epsilon}^p = \dot{\lambda}\frac{\partial \Psi}{\partial \sigma} \tag{3.14}$$

where $\dot{\lambda}$ is the plastic multiplier and Ψ is the plastic potential (Equation 3.15). The direction of the plastic strain vector, $\dot{\epsilon}^p$, is normal to the plastic potential, Ψ.

$$\Psi(\sigma, \epsilon_v^p) = g(\theta, p')q + \tan\psi\left(\frac{p' - p_c}{p_t - p_c}\right)^{\frac{1}{n}} \tag{3.15}$$

where ψ is the dilation parameter. The plastic potential equation is in the same form as the yield surface, however, the plastic potential is in terms of the dilation parameter.

The yield surface is defined for a reference porosity at the surface and scaled to the initial (also known as current-day) porosity using the hardening functions. Similarly, ongoing yield surface evolution uses the hardening/softening functions. The hardening/softening functions define the relationship between the pre-consolidation pressure and volumetric plastic strain, ϵ_v^p.

The SR3 Model uses a smooth hardening law that approximates to the Cam Clay hardening model (Wood, 1990). The relationship is defined by hardening constants κ and λ which define approximate slopes of the elastic unloading-reloading line and hardening normal compression line respectively (Figure 3.5). The hardening range, $\epsilon^p_{v(min)}$ and $\epsilon^p_{v(max)}$, should be compressive and tensile respectively.

The hardening/softening functions are defined in Equation 3.16 and Equation 3.17 and examples are illustrated in Figure 3.6.

$$p_c = p_c^0 + A\left[e\left(-\frac{V({}^t\epsilon_v^p + \Delta\epsilon_v^p)}{\lambda - \kappa}\right) - 1\right] \tag{3.16}$$

$$p_t = p_t^0 + B\left[e\left(-\frac{V({}^t\epsilon_v^p + \Delta\epsilon_v^p)}{\lambda - \kappa}\right) - 1\right] \tag{3.17}$$

where p_c^0 is the initial pre-consolidation pressure, p_t^0 is the initial tensile intercept, V is specific volume and A (Equation 3.18) and B (Equation 3.19) are constants that ensure that the yield surface is always of finite size. If p_t is less than p_t^0 then p_t^0 is used instead.

$$A = p_c^0 - p_{c(resid)} \tag{3.18}$$

$$B = p_t^0 - p_{t(resid)} \tag{3.19}$$

where $p_{c(resid)}$ and $p_{t(resid)}$ are the residual values. The residual values are typically equal to $\frac{p_c^0}{100}$ and $\frac{p_t^0}{100}$.

The porosity is updated according to Equation 3.20.

$$\phi = 1 - \frac{1}{\epsilon^{\delta v}}(1 - \phi_0) \tag{3.20}$$

where ϕ is the updated porosity, ϕ_0 is the preceding porosity and $\epsilon^{\delta v}$ is the change in volumetric strain. Equation 3.20 is also rearranged to calculate the initial volumetric strain where ϕ is the initial porosity (ϕ_{init}) and ϕ_0 is the reference porosity.

The incremental volumetric strain, $\Delta\epsilon^{\delta v}$, is calculated using Equation 3.21.

$$\Delta\epsilon = \frac{\Delta\sigma'}{D_T} \tag{3.21}$$

where $\Delta\sigma'$ is the incremental effective stress and D_T is the constitutive matrix.

The effective stress at time t may be considered as the sum of the effective stress at time $t - \Delta t$ and the incremental effective stress. Furthermore, the porosity is

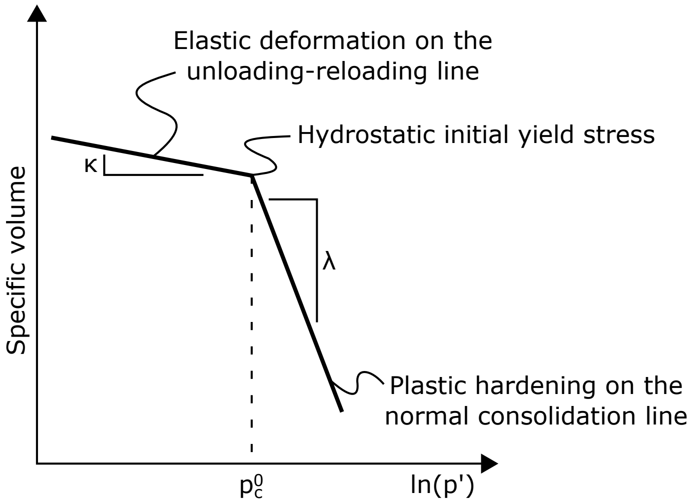

Figure 3.5: Unloading-reloading line and normal compression line. Hardening constants κ and λ define approximate slopes of the unloading-reloading line and normal compression line respectively (edited from Rockfield Software Limited, 2013a). The specific volume, V, is defined as $V = (1 - \phi)^{-1}$.

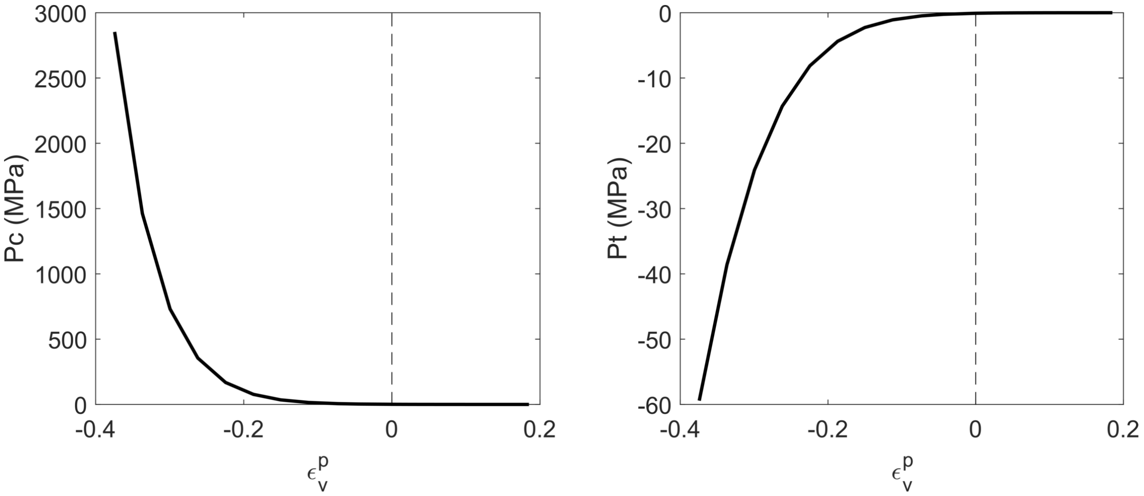

Figure 3.6: Examples of the hardening/softening evolution functions showing p_c and p_t varying with volumetric plastic strain ε^p_v. The size of the yield envelope changes with p_c and p_t.

updated by the incremental volumetric strain. The incremental logarithmic strain, $\Delta\epsilon$, may be additively decomposed into elastic strain, $\Delta\epsilon_e$, short-term mechanical plastic strain, $\Delta\epsilon^p_{mech}$, and thermal strain, $\Delta\epsilon^T$, shown in Equation 3.22, since creep and chemical effects are not modelled.

$$\Delta\epsilon = \Delta\epsilon_e + \Delta\epsilon^p_{mech} + \Delta\epsilon^T \tag{3.22}$$

3.3 Case study: HE-D experiment

The first step in model building is conceptualization. In this instance the HE-D experiment (Wileveau & Rothfuchs, 2003; Wileveau, 2005) is being used as a benchmark test and provides a detailed concept (Figure 3.1).

The principal stresses at the Mont Terri Rock Laboratory are 6–7 MPa 70°/210° (dip/azimuth), 4–5 MPa 10°/320° and 2–3 MPa 20°/050° (Martin & Lanyon, 2003; Nussbaum et al., 2014). The pore-water pressure away from openings is 2.1 MPa and there is negligible water circulation because of the very low permeability of the Opalinus Clay (2.00×10^{-20} m^2). Prior to heating the test field temperature varied between 14 °C and 19 °C. The variation in temperature is caused by the higher variable temperatures in the niche. The test field is not intersected by faults (Nussbaum et al., 2004a; 2004b).

The main gallery at the Mont Terri Rock Laboratory was excavated parallel to the intermediate principal stress in 1998 (Thury & Bossart, 1999). The perpendicular niche from which the sensor boreholes for the HE-D experiment were later drilled was excavated parallel to the minimum principal stress, also in 1998 (Thury & Bossart, 1999). The HE-D niche was excavated from the main gallery in October 2003. The heater borehole was drilled horizontally and equipped in March 2004. The heater borehole has a 0.3 m diameter and 14 m length. Cores from the heater borehole were compact and homogeneous, which justifies the homogeneous model representation. At 0–6.5 m depth the diameter was enlarged to 0.335 m and equipped with a metal tube with an inner diameter of 0.31 m. Two connected electric heaters were installed at 6.5–14 m depth. The effective heating length of both heaters was 5.16 m while the total length was 6.2 m (Wileveau, 2005). The sensors were installed between November 2003 and January 2004 in 24 0.02–0.101 m boreholes drilled using compressed air.

The heater packer was inflated to 1 MPa and heating was initiated with 650 W power on 6th April 2004. On 7th July 2004 heater power was increased to 1950 W. Technical issues included the heater packer deflating to 0 MPa on 21st to 28th July 2004 and no thermal power on 17th December 2004 for a short period of time. Heating stopped on 16th March 2005. The following cooling phase was monitored up to 1st November 2005.

Predictive calculations were reported before the experiment (Wileveau & Rothfuchs, 2003; Wileveau, 2005; Kull et al., 2005; Zhang et al., 2005; Zhang et al., 2006) and further calculations have been reported after the experiment finished (Gens et al., 2007; Zhang et al., 2007a; Wang & Kolditz, 2013; Garitte et al., 2017).

3.3.1 Comparability of other heater test methods

The PRACLAY (Li et al., 2010) and ATLAS III (Chen et al., 2011) experiments in the plastic Boom Clay induced similar THM coupled processes to the experiments in the indurated clays. The thermal diffusion of heat flux and thermal consolidation were the same, being predominantly by conduction, increasing pore pressure by thermal expansion, decreasing viscosity and rapid pore pressure dissipation post-heating. Thermal anisotropy was also observed with higher temperatures recorded parallel to bedding than normal to bedding.

In situ heater tests are also used for higher strength host rocks. The FEBEX experiment in fractured granite emplaced a heater in the centre of a 2.27 m diameter tunnel and backfilled the tunnel with bentonite blocks (Garcia-Sineriz et al., 2005). This is different to the RWM generic design for higher strength fractured rock which has vertical emplacement in 1.75 m diameter boreholes drilled downwards from a tunnel (RWM, 2016a). Rutqvist & Tsang (2004) simulate the FEBEX experiment in ROCMAS (Noorishad & Tsang, 1996) with similar theoretical formulation for the same coupled processes as simulations of the HE-D and TER experiment. The benchmark test was successful, predicting temperature and pore pressure, despite using FEM with no discrete fracture network representation. Therefore, the results presented here may be applicable to higher strength fractured rock.

The TER, PRACLAY and FEBEX experiments all install two heaters into horizontal drifts. The TER experiment layout is similar to the HE-D experiment layout (Wileveau et al., 2009). The PRACLAY and FEBEX experiments used wider tunnels which were backfilled with blocks of compacted bentonite and plugged. The PRACLAY heaters were emplaced into a 1.9 m diameter tunnel and backfilled with fully saturated, high permeability material (Li et al., 2010). The FEBEX heaters were emplaced into a 2.28 m diameter circular tunnel, backfilled with blocks of compacted bentonite and sealed with a 2.70 m long concrete plug (Gens et al., 2009). The FEBEX experiment used 4.54 m long and 0.90 m diameter heaters more closely resembling waste package dimensions (RWM 2016c). The PRACLAY heaters length was designed to limit the effect of the heater ends on the central length, the heaters were a combined 30 m which provided a central zone of 10 m unaffected by the heater ends after 10 years (Sillen & Weetjens, 2004).

3.4 Model setup

The model setup is discussed in three parts: geometry, conditions (initial conditions, boundary conditions and loading) and host rock (material) properties.

3.4.1 Geometry

The HE-D experiment layout (Figure 3.1) is centred on a tubular cavity with a circular cross-section. Different geometric representations of a drilled hole with a circular cross-section are illustrated in Figure 3.7. Different geometric representations should be considered in modelling because they can simplify a problem and reduce computation time.

The 3D and axisymmetric models can simulate the heaters as finite lengths. Figure 3.7a and 3.7d simulate the borehole end which is important for the HE-D experiment because of the drained condition on the borehole. Both geometries have been used in published benchmark tests of the HE-D experiment and shown to be able to reproduce the experiment data (Gens et al., 2007; Zhang et al., 2007a).

An axisymmetric model is used in the benchmark test because a low computation time is a requirement for the sensitivity analysis in the following chapter. An axisymmetric design approximates a 3D problem using rotational symmetry. This is achieved by assuming a unit radian out-of-plane depth and zero out-of-plane strain. Therefore, axisymmetric models may only have vertical transverse isotropy if the symmetry axis is vertical. The isotropic assumption is accurate for the initial temperature distribution because the geothermal temperature and facility temperature are similar (Wileveau, 2005). It is not accurate for the initial pore pressure distribution or boundary conditions because the heater experiment has a ventilated niche 8 m away on one side. Furthermore, the Opalinus Clay is an anisotropic material. However, previous publications (Gens et al., 2007) conclude that anisotropic models calculate accurate pore pressures for the HE-D experiment.

The sensor locations are included as points at which the model outputs results at a higher frequency. This is more efficient than increasing the results output frequency for the whole model. The sensor coordinates are converted to a depth and radial distance to the borehole for the axisymmetric representation (Figure 3.8).

An efficient structured mesh of rectangular elements is used with progressive lengthening towards the boundaries. The total number of elements is 2024. The element within which a sensor is located determines the accuracy of the sensor location in the model. The smaller the element, the more accurate the sensor location. It would be possible to represent the exact location of the sensors within the model

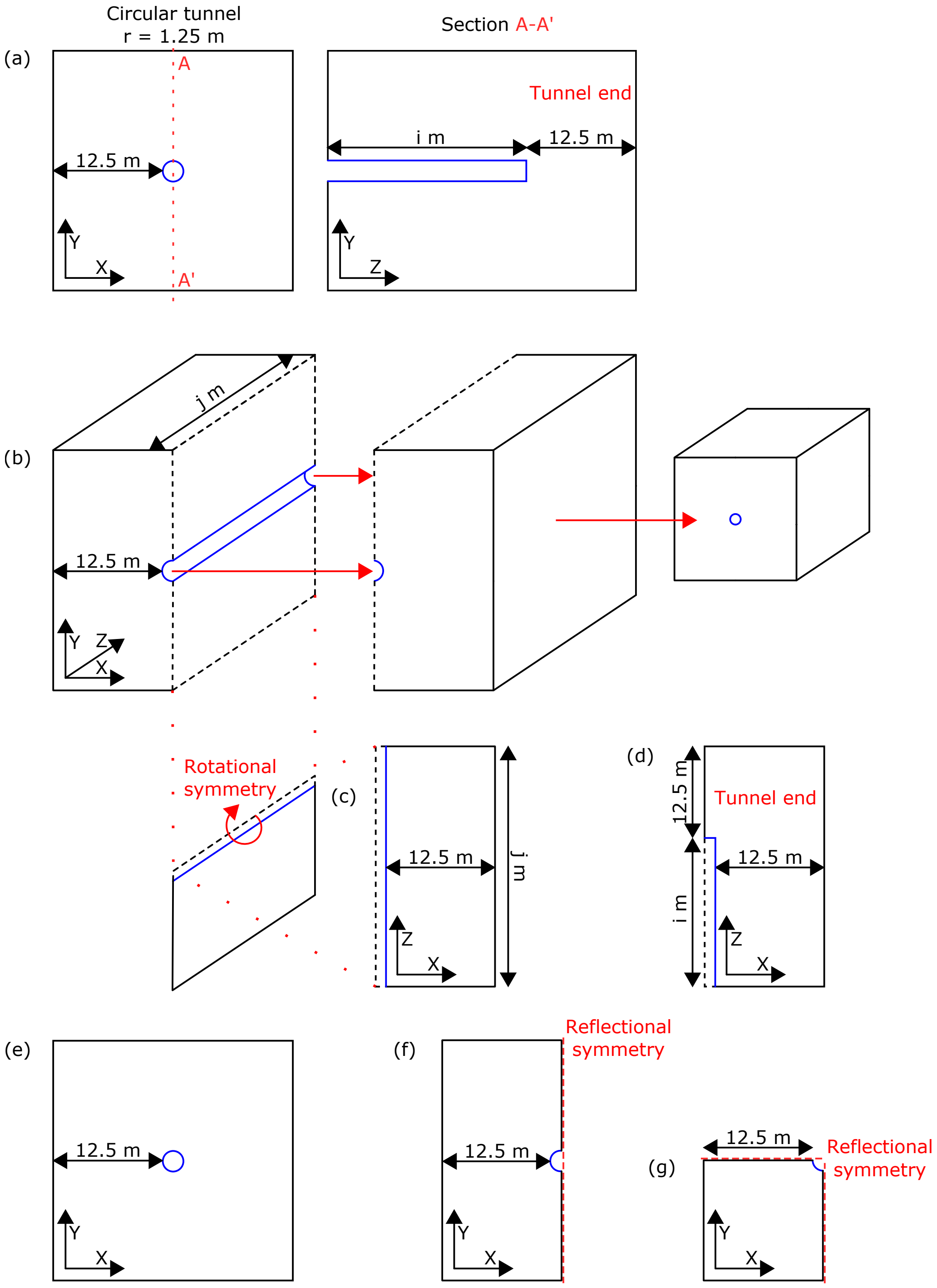

Figure 3.7: Various geometric representations of the disposal tunnel. Tunnel walls are blue. Solid black lines are zero-normal-displacement boundaries in 2D and surround surfaces that are zero-normal-displacement boundaries in 3D. Visual guides are red. (a) and (b) are 3D; (c) and (d) are axisymmetric; (e), (f) and (g) are 2D plane strain. (a) and (d) include the tunnel end.

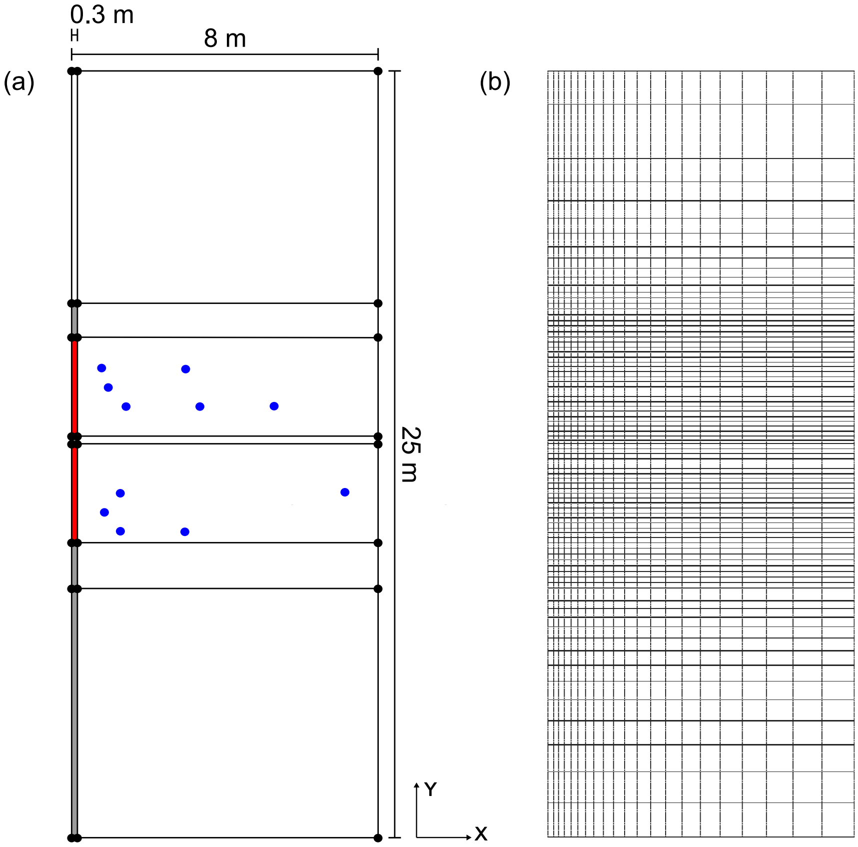

Figure 3.8: Model geometry (a) and mesh (b). The heater locations are illustrated in red, the borehole in grey, and sensor locations for high temporal resolution results are illustrated in blue.

using an unstructured mesh. A structured mesh is preferred because of the later sensitivity analysis in which computational time is more important than the difference in sensor locations for the benchmark test.

3.4.2 Conditions

The model uses 4.8 MPa, 15 °C and 0.9 MPa as homogeneous, initial mean stress, temperature and pore-water pressure. 0.9 MPa pore-water pressure is reduced from the in situ value of 2.2 MPa because of the influence of tunnels and niches (Gens et al., 2007). Zhang et al. (2007a) simulate a niche with a prescribed 0.1 MPa pore-water pressure and allow the pore pressure to approach equilibrium in a pre-heating stage. The models presented here apply the reduced initial homogeneous pore pressure approach (Gens et al., 2007) because it is more efficient than simulating a pre-heating stage.

Garitte et al. (2017) recommend a drained condition for the heater borehole but find the niches have a negligible effect. The model presented here has a 0.1 MPa load applied to the heater borehole to simulate that it is drained (similar to Gens et al., 2007; Zhang et al., 2007a). Note that 0.1 MPa is close to 0 MPa and applied because it is not possible to apply a 0 MPa load. Also that near-zero pore pressure approximates a drained condition under the fully saturated assumption (Rockfield Software Limited, 2013b).

The thermal load is simulated by an internal heat generation load applied to the surfaces representing the cylindrical heaters. The thermal load is the maximum heater output of 975 W which is applied over the load curve shown in Figure 3.9.

The excavation and packer pressure are not simulated because the thermal load must be applied to a surface rather than a line in the axisymmetric model. This

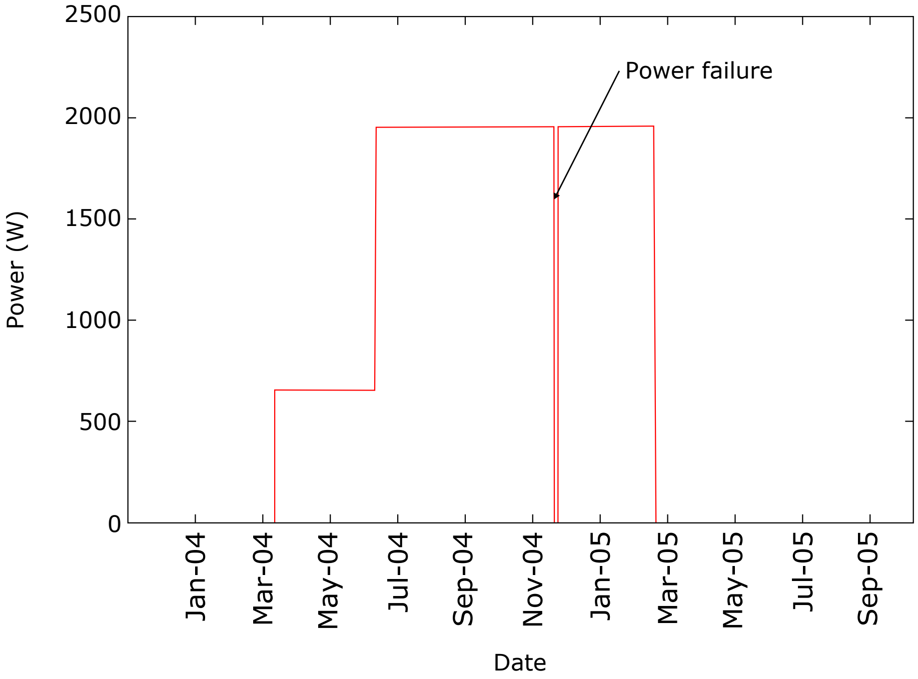

Figure 3.9: HE-D model thermal load. The HE-D experiment started on 06/04/2004, the power failure occurred on 17/12/2004 and the heating ended on 16/03/2005.

has a local effect of 3.8 MPa higher compressive stress at the heater interface. No failure was observed in the experiment (Zhang et al., 2007a) or modelling (Garitte et al., 2017), therefore, this is expected to have limited effect. The 3.8 MPa error decreases exponentially towards negligible at 1.5 m (i.e. 10 radii) from the heater interface (Jaeger et al., 2007). The main effect of the heater borehole on the nearest sensor is the drained condition (Garitte et al., 2017) which is simulated.

3.4.3 Host rock properties

The material model uses the hydraulic and thermal properties of the Opalinus Clay characterized at Mont Terri (Table 3.1). The temperature dependent fluid viscosity, μ, is defined by Equation 3.23.

$$\mu = A \exp\left(\frac{B}{273.15 + T}\right) \tag{3.23}$$

where A and B are empirical constants and T is temperature. This is Vogel's equation (Vogel, 1921) in the form of the Arrhenius equation (Arrhenius, 1889). A is 2.1×10^{-12} MPa.s and B is 1808.5 K (Zhang et al., 2007a).

The material model uses the geomechanical properties of the Opalinus Clay that have been characterized at Mont Terri (Bock, 2001). However, the SR3 model (Crook et al., 2003) properties have not been previously determined for the Opalinus Clay. The undetermined properties were predicted using one-dimensional consolidation (e.g. Mohamedelhassan & Shang, 2002) and triaxial tests (e.g. Wolfs et al., 2019) models which are discussed here.

Rockfield Software Ltd provide generic SR3 material characterizations for clays (Rockfield, 2012). Twelve generic clays are described by their depositional state and three primary dependencies: porosity against mean effective stress, residual friction angle and cohesion (Figure 3.10). These clays can be initialized with a current-day porosity which is used with the depositional porosity (Crisci et al., 2019) to determine the volumetric plastic strain (Equation 3.20). Then the volumetric plastic strain describes the position of the yield envelope on the hardening curve (Figure 3.6).

Parameter	Value	Unit	Citations
Grain, parallel thermal conductivity	1.0	W/m.K	Mugler et al. (2006); Zhang et al. (2007a).
Grain, perpendicular thermal conductivity	2.1	W/m.K	Mugler et al. (2006); Zhang et al. (2007a).
Grain, isotropic thermal conductivity	1.7	W/m.K	Zhang et al. (2007a).
Fluid, thermal conductivity	0.58	W/m.K	National Physical Laboratory, 2018.
Grain, thermal heat capacity	800	J/kg.K	Weber (1997); Knill (1998); Bock (2001).
Fluid, thermal heat capacity	4184	J/kg.K	National Physical Laboratory, 2018.
Rock, linear thermal expansion	1.7×10^{-5}	/K	Zhang et al. (2007a).
Grain, volumetric thermal expansion	6.0×10^{-6}	/K	Noynaert et al. (2000); Zhang et al. (2007a).
Fluid, volumetric thermal expansion	3.4×10^{-4}	/K	National Physical Laboratory, 2018.
Permeability at 0.16 porosity	2.00×10^{-20}	m^2	Marschall et al. (2005); Gens et al. (2007).
Fluid viscosity	Equation 3.23	Pa.s	Zhang et al., 2007a

Table 3.1: Hydraulic and thermal properties of the Opalinus Clay as characterized at Mont Terri. The fluid viscosity and heat capacities are scaled from seconds to days, by dividing by seconds in a day, to reduce the computation time. The isotropic thermal conductivity is the mean of the orthotropic values. The permeability has a Kozeny-Carman relationship which is illustrated in Figure 3.2.

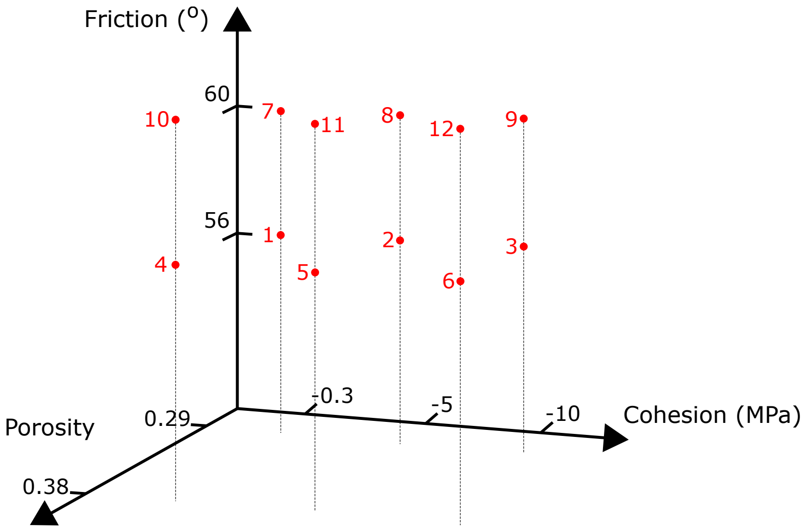

Figure 3.10: The twelve generic clays (red points) are permutations of two porosities, two friction angles and three cements, describing the original sediment properties.

Hydrostatic grain crushing processes are controlled by micro-structural parameters, such as porosity and grain size (Zhang et al., 2000) which influence the compactive yield envelope (Figure 3.4). Therefore, it is valid to use the consolidation behaviour in terms of porosity to initialize constitutive models.

One-dimensional consolidation

A one-dimensional consolidation model (Figure 3.11) was used to evaluate the preconsolidation pressures with respect to deposition via compaction under gravity. The results are used to compare the generic clays to Opalinus Clay in terms of porosity with respect to burial history.

The sediment was assumed to be deposited in a laterally continuous layer with laterally continuous burial and geostatic loading only. These assumptions provide the simplest possible deposition and post-depositional history (e.g. Terzaghi, 1943). This can be represented as a 1D column and was modelled as a stack of square elements (Figure 3.11). The width of the column was 10% of the height which ensured that the mesh elements were not undesirably elongated. The mesh was structured with 20 equally distributed vertical divisions and was one element wide.

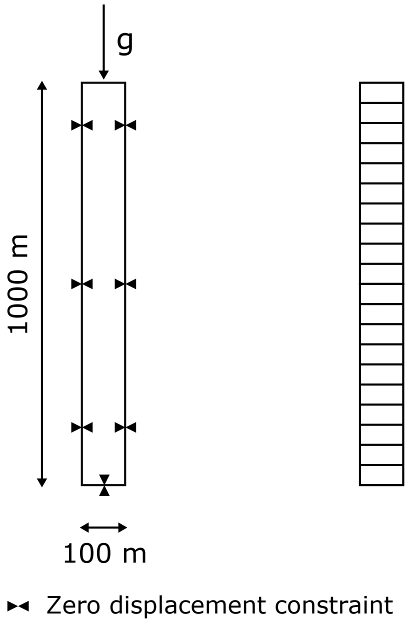

Figure 3.11: Column test conceptual model and model mesh. The mesh is structured with 20 equally distributed vertical divisions and is one element wide.

Gravity loading was used and a horizontal stress factor of 0.6 was assumed. 0.6 is reasonable because the intermediate principal stress at Mont Terri is 0.69 of the major principal stress. The minimum principal stress is 0.385, which is lowered by a valley in the topography (Nussbaum et al., 2014).

The gradient of compaction curves (porosity against mean effective stress or depth) depends upon the plastic response of the clay. Clay compaction curves often transition between flatter and steeper regions indicating that they are over-consolidated (Nygard et al., 2004a; 2004b). This has an important effect on the compressibility and shear behaviour. The transition point indicates the pre-consolidation stress, which is the maximum level of stress experienced by the clay during its post-depositional history. The pre-consolidation stress is also considered as a ‘yield stress’ within the framework of critical state theory (Xiong et al., 2019).

The depth relationship results for the twelve column models are presented in Figure 3.12. The generic clays have variable porosity compaction behaviours which represent varying particle size distributions and diagenetic processes.

Opalinus Clay has a porosity of 0.16 and an estimated maximum burial depth of

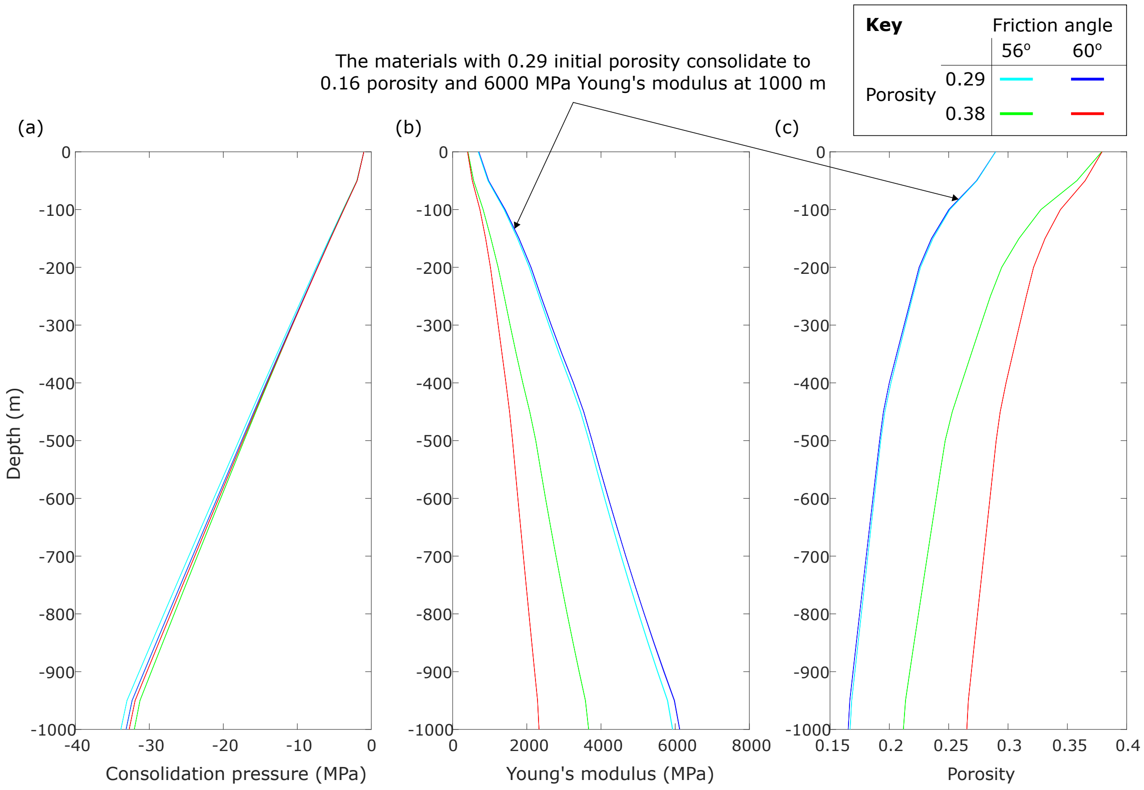

Figure 3.12: Depth relationships of consolidation pressure, Young's modulus and porosity (compaction curve) predicted by the column models for the twelve generic material models (Figure 3.10).

at least 1000 m (Bossart et al., 2017). The column models predict that the generic materials with 0.29 depositional porosity have a porosity of 0.16–0.17 at 1000 m depth.

Triaxial test

Triaxial tests (Figure 2.5) are modelled to demonstrate the behaviour of an SR3 material model that has been initialized for current day porosity. The six clays with 0.29 depositional porosity (Figure 3.10) are initialized with a current-day porosity equal to the Opalinus Clay at Mont Terri.

Only the sample is geometrically represented (Figure 3.13a and Figure 3.13b) because the triaxial rig is simulated as loading conditions. The sample height is

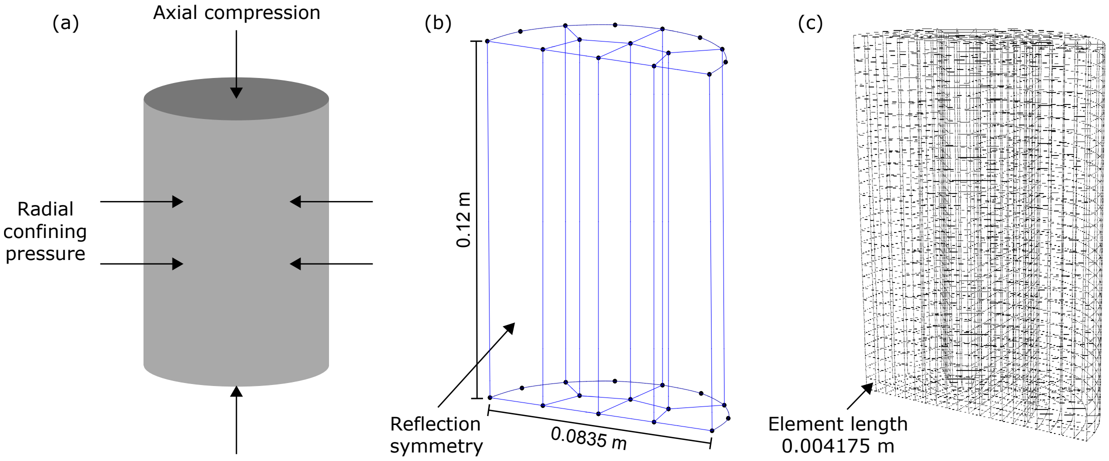

Figure 3.13: Triaxial test (a) conceptual model, (b) model geometry and (c) mesh. The internal geometry is divided into hexahedrons for improved structured meshing.

120 mm and radius is 41.75 mm. The geometric model uses reflection symmetry to half the size of the model. A zero-normal-displacement boundary condition is assigned to the surface on the reflection plane. The shear plane that develops will be reflexively normal to the reflection plane ensuring that it is the reflection plane.

An ideal triaxial test specimen geometry and equally distributed structured mesh are unrealistically perfect. The simulation result is a specimen that cannot shear asymmetrically as expected. Therefore, very small geometric imperfections are introduced to the model.

The meshing approach is structured and uses equally spaced element divisions. The mesh is illustrated in Figure 3.13c. The characteristic length for regularisation should be smaller than the mesh element length. The characteristic length for regularisation is 0.001 m. This is appropriate for laboratory scale specimens (Rockfield Software Limited, 2013a).

The axial compression is simulated using equal and opposite loads applied normal to the planar top and bottom surfaces of the sample. Points on each top and bottom surface are coupled together to ensure they remain planar. The loads are applied over linear loading curves which control the maximum axial strain. The solution is static, therefore, strain rate has no effects.

The confining pressure is simulated using a constant face load applied normal to the curved surface of the sample. This magnitude is either 2 MPa, 5 MPa or 8 MPa in each model which are comparative to laboratory tests presented in Zhang et al. (2004b). The initial effective stress is also set to the confining pressure.

The stress/strain behaviours of the six generic material models are presented in Figure 3.14. Clay 3 and Clay 9 with high cementation fail with no plastic strain. Otherwise, the samples exhibit a typical poro-elastic-plastic response. Linear axial compression and radial extension until the onset of dilatancy. Yield strains with hardening until the peak strength. Then plastic-flow until failure.

The same behaviour was observed in triaxial tests with Opalinus Clay specimens (Figure 3.15; Zhang et al., 2004b). Peak strength in the Opalinus Clay specimens was typically 18 MPa at 5 MPa confining pressure and 6 MPa at 1 MPa confining pressure. Clay 7 with lower cohesion and higher friction angle (Figure 3.10) is most similar to the Opalinus Clay.

The calibrated geomechanical properties for the Opalinus Clay SR3 material model are described in Table 3.2.

Symbol	Parameter	Value	Unit
ρ_f	Fluid density	1000	kg/m^3
ρ_s	Grain density	2700	kg/m^3
ϕ_{ref}	Reference porosity	0.29	
E_{ref}	Reference Young's modulus	40	MPa
n	Exponent	0.3	
c	Exponent	-2	
ν	Poisson's ratio	0.295	
P_c	Pre-consolidation pressure	1	MPa
P_t	Tensile intercept	-0.018	MPa
β	Friction	60	°
Ψ	Dilation	51	°
κ	Hardening constant	0.012	
λ	Hardening constant	0.077	
l_c	Regularisation characteristic length	0.001	m

Table 3.2: Geomechanical properties of the Opalinus Clay determined through one-dimensional consolidation tests and triaxial tests on a range of generic clays.

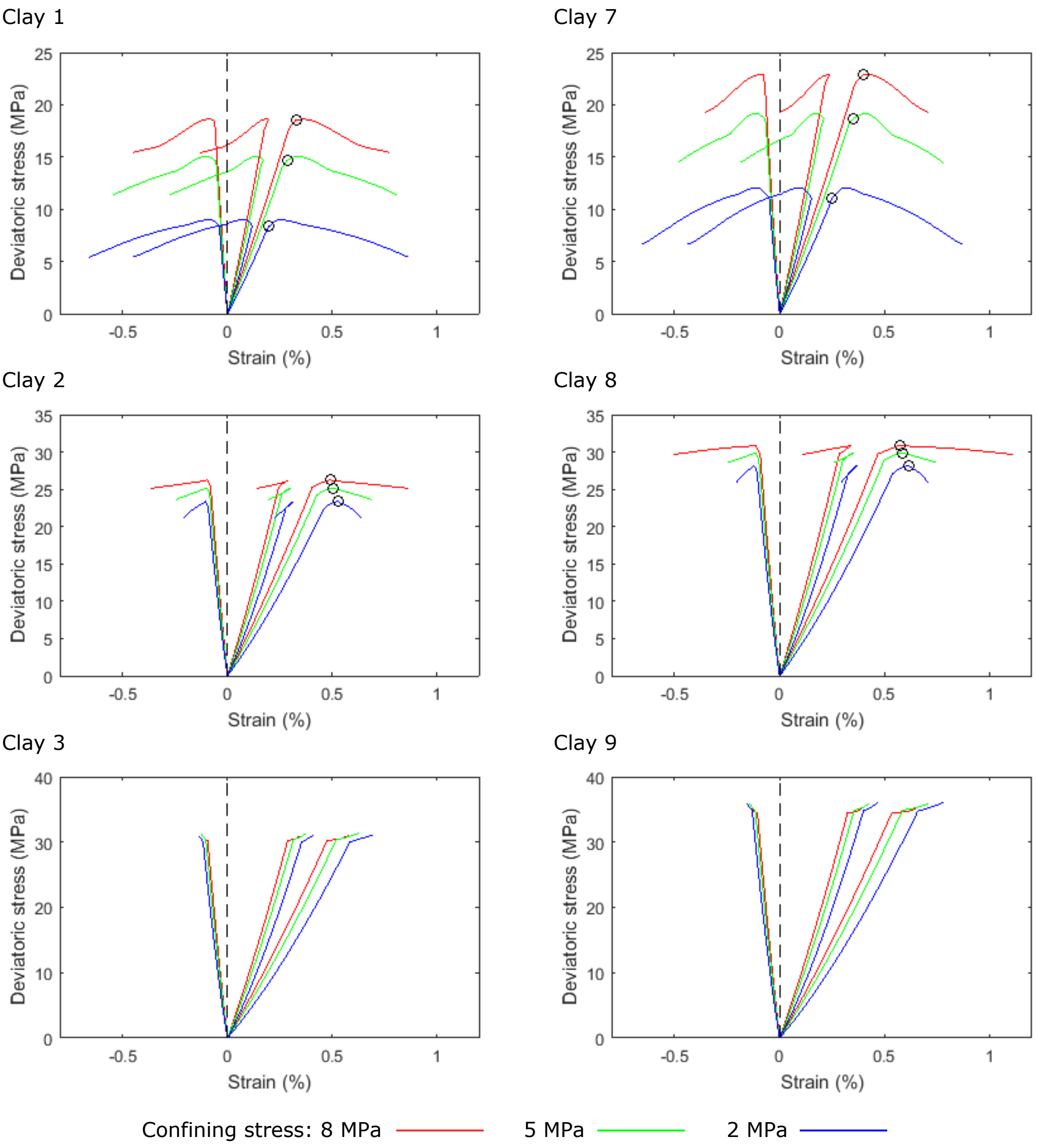

Figure 3.14: Axial, radial and volumetric stress-strain behaviour in the triaxial tests on the generic clays (Figure 3.10) with different confining pressures. The subplots are ordered so that cohesion increases from top to bottom and friction angle increases from left to right. Circles indicate the onset of dilatancy which is determined as the axial strain at peak volumetric strain. Clay 3 and Clay 9 do not undergo volumetric expansion.

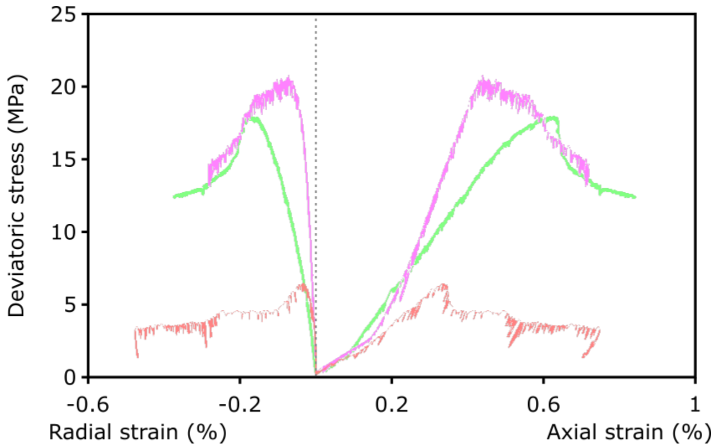

Figure 3.15: Representative axial and radial stress-strain behaviour from triaxial tests with different confining pressures on Opalinus Clay from the HE-D test site (edited from Zhang et al., 2004b). Peak strength in the Opalinus Clay specimens was typically 18 MPa at 5 MPa confining pressure (green) and 6 MPa at 1 MPa confining pressure (red).

3.5 HE-D benchmark test results

The axisymmetric HE-D experiment model was run on an Intel(R) Core (TM) i5-4430 CPU @ 3.00GHz processor with 16.0 GB RAM. The CPU time was 35 minutes. The modelling results are compared with the HE-D experiment temperature and pore pressure data.

3.5.1 Temperature

Figure 3.16 shows the temperature and pore pressure perturbation predicted by the axisymmetric model after 114 days. The 3 month heating phase caused a temperature increase of 28 °C at the heater/rock interface. The following 8 month heating phase caused a further increase of 62 °C. A 2 °C increase extends to 3 m after 3 months and 6.5 m after 11 months.

Figure 3.17 compares the model and experiment temperature data at three representative sensor locations showing an error up to 2 °C. The heater power failure is less significant in the model prediction than the laboratory data. The heater power failure duration is not reported accurately in literature, therefore, the discrepancy may be because the duration applied by the model power load curve is not accurate.

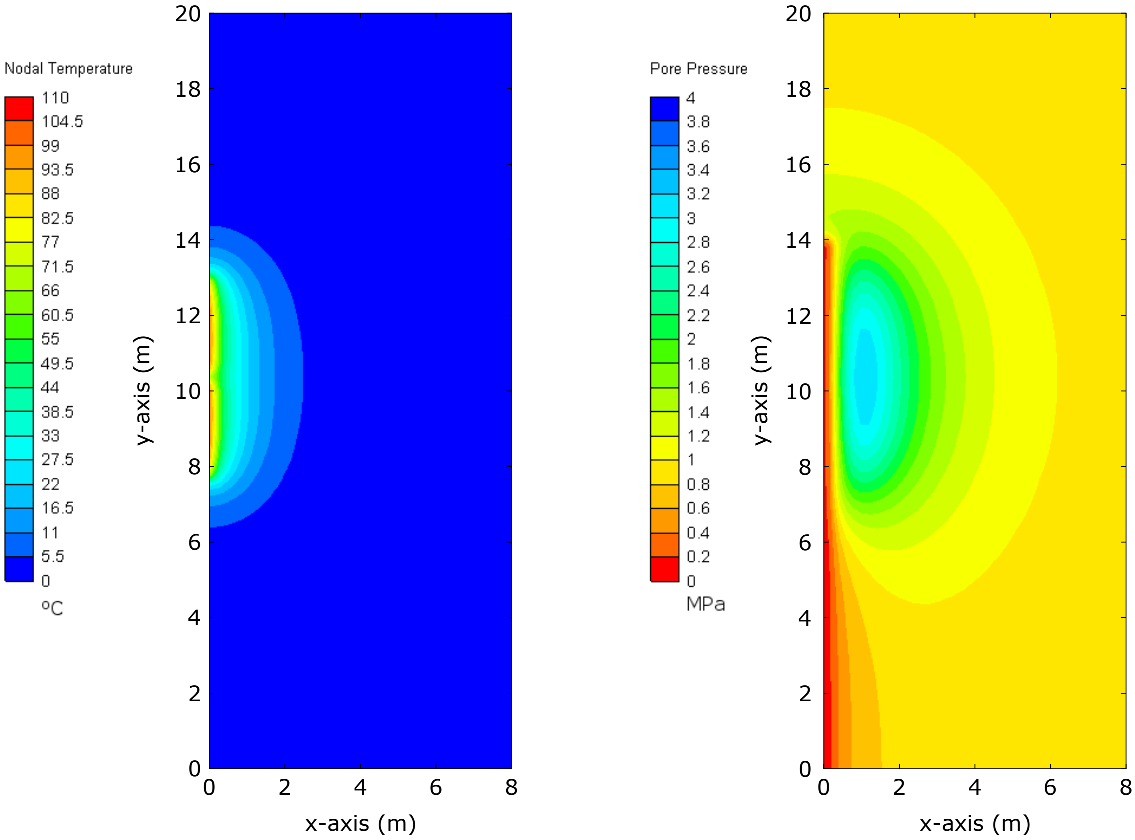

Figure 3.16: Temperature and pore pressure contour plots for the axisymmetric model taken after 114 days of heating. The temperature scale maximum is higher than the maximum temperature in the rock because of the higher temperature of the heaters.

Elsewhere at other sensor locations, the error is up to 6 °C. The sources of error are the isotropic material properties, an initial temperature range of 4 °C and sensor location accuracy dependence on the mesh element size. Overall, the temperature perturbation is well simulated.

3.5.2 Pore pressure

Increasing temperature causes a high pore pressure zone (Figure 3.16). The zone decreases towards the far-field as expected and decreases towards the heater because the borehole has a drained condition. The 3 month heating phase caused pore pressure to increase to 2.5 MPa at 1.2 m from the heater. The following 8 month

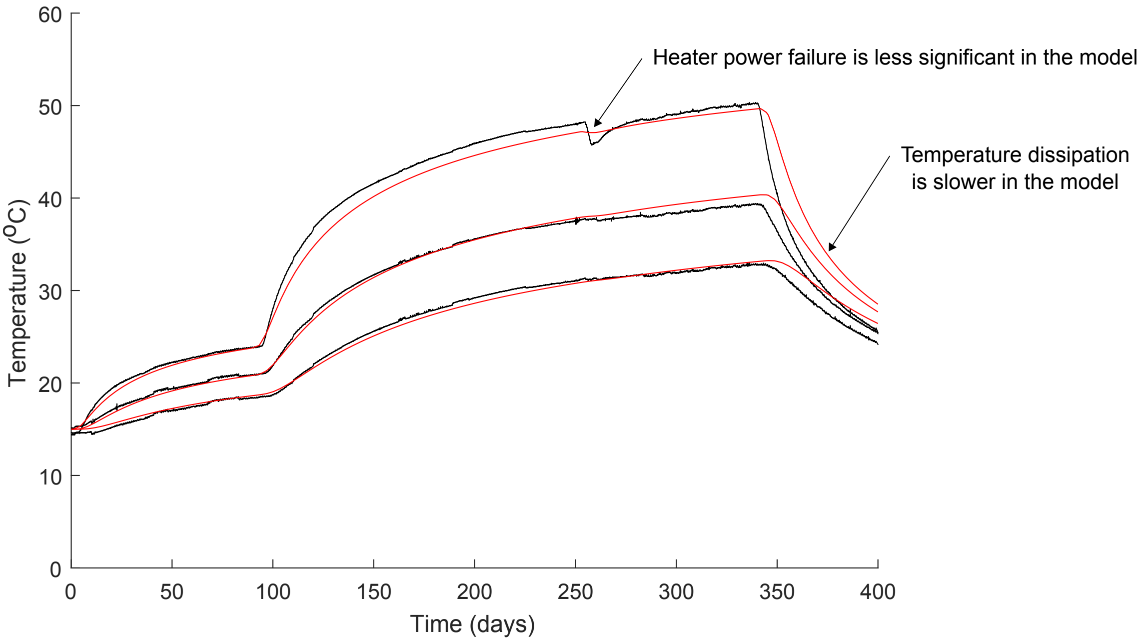

Figure 3.17: Temperature benchmark test where laboratory data is black and model prediction is red. Sensor coordinates (radial distance, longitudinal distance) are (0.85 m, 8.50 m), (1.27 m, 8.00 m) and (2.95 m, 12.24 m), where the higher temperatures are observed at lower radial distances.

heating phase caused pore pressure to increase up to 4 MPa. The pore pressure evolution is controlled primarily by the temperature evolution. As the temperature versus time gradient decreases, the pore pressure reaches a maximum and then begins to dissipate. The hottest area nearest the heater does not have the highest pore pressure because the heater borehole has a drained condition.

Figure 3.18 compares the model and experiment pore pressure data at representative sensor locations. Initial pore pressure discrepancies exist because the complicated test site conditions are simplified to a homogeneous initial pore pressure. The heater power failure is less significant in the model prediction than the laboratory data as discussed previously. The experiment and model observe a rapid decrease in pore pressures during the cooling phase. The experiment and model diverge after 0 MPa. The model predicts negative pore pressures near the heaters during cooling, however, the piezometers used in the experiment do not measure negative pore pressures (Marques & Leroueil et al., 2015). Negative pore pressures in the near-field

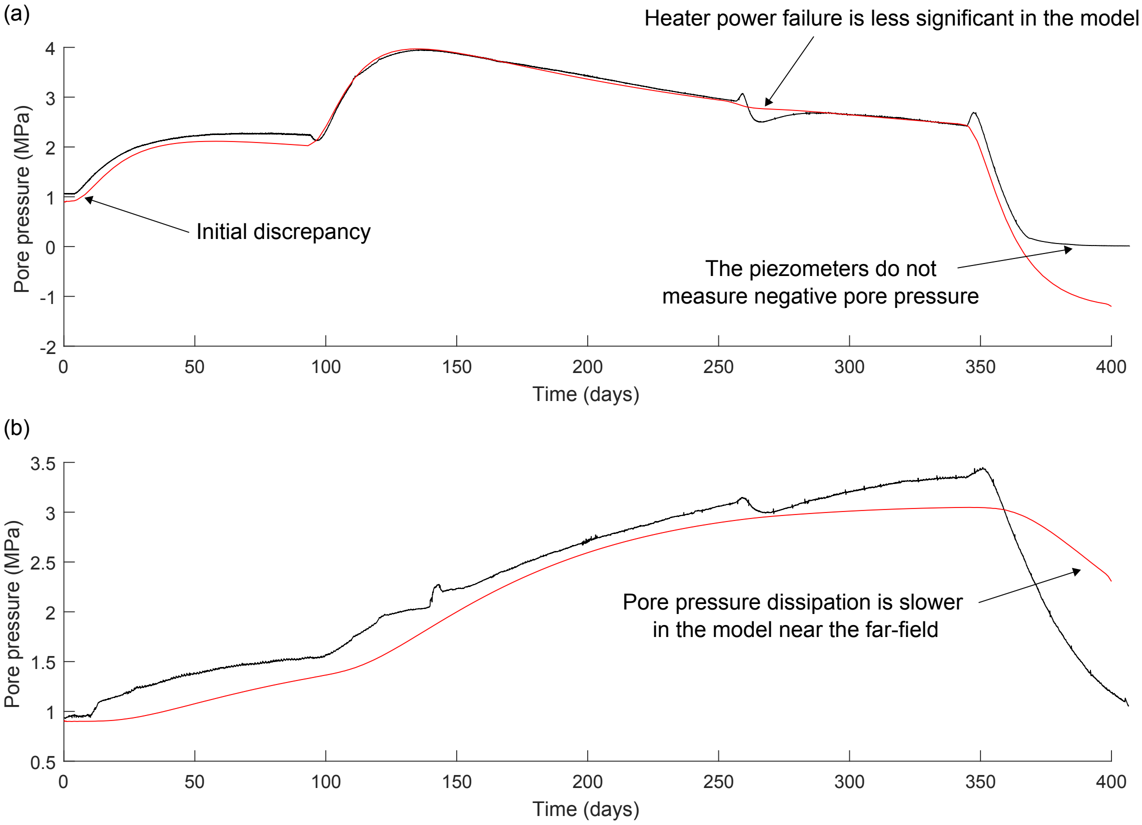

Figure 3.18: Pore pressure benchmark test where laboratory data is black and model prediction is red. (a) 0.85 m radial distance and 8.50 m longitudinal distance. (b) 1.27 m radial distance and 8.99 m longitudinal distance.

indicate desaturation. The model predicts pore pressure dissipation less accurately further from the heaters because of the insulating effect of the model boundary condition. Other sources of error are the isotropic material properties and sensor location accuracy dependence on the mesh element size.

The rock expands within the pore pressure perturbation because of the expansion of the pore fluid. The rock is compressed ahead of the pore pressure perturbation because of the rock expansion within the pore pressure perturbation. Porous flow gradually dissipates the pore pressure. When the heaters are switched off, the temperature decreases and the pore fluid contraction rapidly decreases the pore pressure. The associated increase in effective stress compresses the rock.

Transient pore pressure anomaly

In the experiment, a temporary decrease in pore pressure is measured in all of the piezometers at the start of each heating phase, before the expected increase in pore pressure is measured (Figure 3.18). This immediate, opposite reaction is also observed as a temporary increase in pore pressure when switching off the heaters and when the heaters failed. The phenomenon was most significant at the sensor closest to the heater. The reason for the behaviour is unknown (Zhang et al., 2007a). This response was not seen in any published numerical models of the experiment or in the predicted pore pressure presented here.

3.6 Discussion

The broader implications of these results for THM modelling of GDFs are discussed in Section 6.2. In particular, the coupled processes that are controlling the temperature, pore pressure and displacement perturbations which should be expected around heat-producing waste in lower strength sedimentary host rock GDFs.

3.6.1 Transient pore pressure anomaly

The transient pore pressure anomaly was observed in other in situ heater tests including ATLAS III (Chen et al., 2011) and FEBEX (Rutqvist & Tsang, 2004). Therefore, the behaviour is not a quirk of the experimental field or setup but a physical phenomenon that might be expected with improved understanding.

Chen et al. (2011) provide the most detailed investigation into the transient pore pressure anomaly, finding that the expected pore pressure reaction occurs when the local temperature reacts to the power change and that the opposite reaction occurs in the time between the power change and the local temperature reaction. The authors attribute this to indirect evidence for the mechanical anisotropy in Boom Clay. However, no further explanation for the actual mechanism is provided and there is no directional dependence of the phenomenon observation at the sensor locations. The phenomenon is not modelled in other 3D anisotropic models (Gens et al., 2007). Furthermore, the phenomenon is observed in the FEBEX experiment in fractured granite where the hydraulic conductivity is controlled by the fracture network (Martinez-Landa & Carrera, 2005) and which is usually modelled as isotropic (Rutqvist & Tsang, 2004; Nguyen et al., 2005).

The oversight in previous publications has been assuming that the fluid flux is away from the heaters because the pore pressure gradient is caused by the temperature gradient (Garitte et al., 2017). This is despite previous publications finding that simulating the heater borehole as drained is crucial for accurately modelling the pore pressure behaviour (Zhang et al., 2007a).

Figure 3.19 progresses understanding of the transient pore pressure anomaly by showing that it coincides with reverses in the direction of movement of the peak pore pressure. The peak pore pressure is not next to the heater because the heater borehole is drained. The peak pore pressure generally translates away from the heaters in the x-direction over time as the temperature increases. However, the immediate response to heater changes is for the peak to move towards the heater and it is during this time that the transient pore pressure anomaly is observed.

The mechanism, therefore, is suction towards the drained borehole which is supported by the desaturation in the test field. The suction reaction occurs faster than the local temperature reaction, then when the local temperature reacts it becomes the driving process and the expected pore pressure reaction is achieved. When the heating stops, the direction of peak pore pressure movement reverses and the pore pressure measures a short increase. This has implications for heat-producing waste disposal because the backfill material will be a sink for fluid until it is saturated (Tripathy et al., 2004; Shirazi et al., 2010).

3.6.2 Summary

A benchmark test was used to validate a model of an in situ heat test in Opalinus Clay. The in situ heat test in Opalinus Clay is an analogue for heat-producing waste emplaced in lower strength sedimentary rock. The model building process, theoretical formulation and assumptions behind the models in this work were demonstrated and validated.

Firstly, a simple 2D column model was used to demonstrate the behaviour of the material model during burial. Twelve clays were simulated and six with comparable

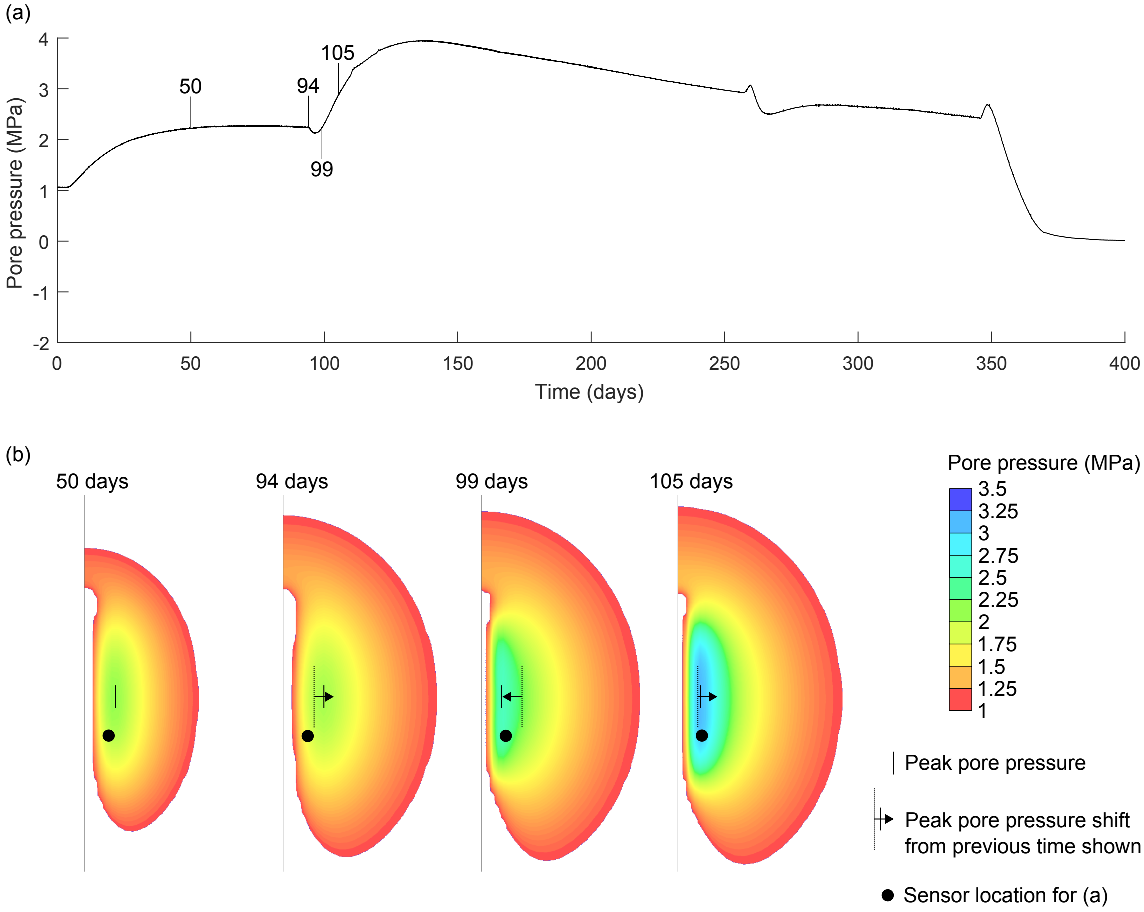

Figure 3.19: Peak pore pressure shift analysis for opposite effect diagnosis. (a) Temporal pore pressure laboratory data from 0.85 m radial distance and 8.50 m longitudinal distance. (b) Predicted pore pressure contours after 50, 94, 99 and 105 days. The peak pore pressure generally shifts away from the heaters during heating. However, the peak pore pressure shifts towards the heaters for 5 days after the heater output is increased. This reversal coincides with the opposite effect observed in the laboratory data.

porosity to Opalinus Clay at its maximum burial depth were selected. Secondly, a 3D triaxial test model was used to demonstrate the behaviour of the material model when initiated at a current-day porosity. Triaxial test laboratory data from literature was used to compare the six clays to the Opalinus Clay and one was selected as analogous to the lower strength sedimentary rock. The final model integrated hydraulic and thermal coupling to the soft rock material model. The parameter values used were recommended values for the Opalinus Clay from literature. Data from an in situ heater experiment in literature was used as a benchmark test. The material model behaved similar to the Opalinus Clay in the experiment which additionally validates the THM coupling and thermal loading.

An axisymmetric representation was used, to reduce computation time (to 35 minutes), so that the model could be used in a computationally expensive sensitivity analysis (Chapter 4).

Chapter 4

Global sensitivity analysis

4.1 Introduction

This chapter presents global sensitivity analyses on the benchmarked heater test model. The model is used because it is a good analogue for heat-producing waste (Wileveau & Rothfuchs, 2003; Wileveau, 2005) emplaced in lower strength sedimentary rock (Towler et al., 2008) and because it is reasonable to assume that the uncertainty in rock properties (Bock, 2001) will be similar to the uncertainty in rock properties at a GDF. Whereas a real case study does not yet exist (Gens, 2018). These are prerequisites for a meaningful sensitivity analysis. The analyses might be considered uncertainty analyses because they use the uncertainty to define the input factor ranges, however, they do not aim to address the question 'How uncertain is the prediction?'.

There are three complimentary objectives. Method demonstration for computationally expensive, coupled, FEM models. Input factor screening and convergence analysis for decreasing the number of parameters that are considered uncertain and informing the sample size of future, similar global sensitivity analyses. Finally, input factor ranking to improve understanding of the processes occurring around heat-producing waste in lower strength sedimentary rocks (diagnostic evaluation) and to support model calibration.

4.2 Global sensitivity analysis approach

Global sensitivity analyses investigate the whole input factor uncertainty space using Monte Carlo style simulation (Iooss & Lemaitre, 2015). Investigating the parameter space globally is important because of interactions between input factors. Global sensitivity analyses provide a coherent mathematical methodology to determine important input factors (x) and their influence on the model output (y). SAFE toolbox (Pianosi et al., 2015) functions are used to estimate sensitivity indices for input factor screening and ranking given x and y. The sensitivity indices are assigned to the inputs and are a measure of an inputs influence on the output. Note that this means the input with the highest sensitivity indices is most sensitive for the output and does not mean the input is affected by the output.

The objective of screening is to separate the input factors into a sensitive group and a non-influential group, x_0. The non-influential group are input factors that are completely insensitive and also the ones that have a small and negligible effect (Sarrazin et al., 2016). Typically a threshold value, T, is assumed for the sensitivity index, below which the input factors are considered as non-influential (e.g. Cosenza et al., 2013; Vanrolleghem et al., 2015). The global sensitivity analysis method used for input factor screening is the EET (Petropoulos & Srivastava, 2016). Sarrazin et al. (2016) demonstrate that screening converges with less model evaluations than other sensitivity analyses objectives. Therefore, screening was performed first so that the non-influential input factors could be removed from the ranking analyses for efficiency (Pianosi et al., 2016).

The global sensitivity analysis method used for input factor ranking is the multi-method approach designed in Petropoulos & Srivastava (2016). The approach enhances the credibility of the study by using three sensitivity analyses in unison to estimate three indices for each input factor instead of one. This is achieved without increasing the computational expense of the study because the methods use the same generic input-output dataset. Therefore, no additional model evaluations are required. The three sensitivity analyses are the regional sensitivity analysis (Spear & Hornberger, 1980), PAWN (Pianosi et al., 2015), and an estimate of the main effects indices from the variance-based sensitivity analysis (Petropoulos & Srivastava, 2016).

4.2.1 Elementary Effects Test

An elementary effect (EE) is calculated for the i^{th} input factor, x_i, at baseline point, x^j, for a predefined perturbation, Δ, using Equation 4.1.

$$EE_i^j = \frac{y(x_1^j, x_2^j, ..., x_{i-1}^j, x_i^j + \Delta, ...x_k^j) - y(x_1^j, x_1^j, ..., x_{i-1}^j, x_i^j, ...x_k^j)}{\Delta} \tag{4.1}$$

EEs are computed at n baseline points. The mean of the absolute values of the EEs, μ_i^*, is a measure of the total effects of the i^{th} input factor (Equation 4.2) and the standard deviation of the EEs, σ_i, indicates the intensity of the interactions of the i^{th} input factor with other input factors (Figure 4.1). Absolute values are used to prevent opposite sign compensations (Campolongo et al., 2007).

$$\mu_i^* = \frac{1}{n} \sum_{j=1}^{n} |EE_i^j| \tag{4.2}$$

The baseline points and perturbation are defined using the radial design strategy (Campolongo et al., 2011). The random baseline points are associated with random auxiliary points and the perturbation is the difference between the i^{th} coordinate of the baseline and auxiliary point. The baseline and auxiliary points are the samples generated by the Latin hypercube sampling.

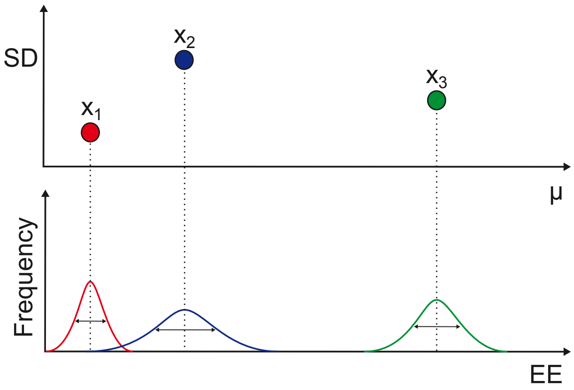

Figure 4.1: The mean, μ, and standard deviation, SD, of the EE distributions of input factors x_1, x_2 and x_3 are projected onto an EE $\mu - SD$ plot. The mean is a measure of the total effects of the i^{th} input factor and the standard deviation is a measure of the intensity of the interactions of the i^{th} input factor with other input factors.

4.2.2 Regional sensitivity analysis

The regional sensitivity analysis (Spear & Hornberger, 1980) sensitivity indices are the Kolmogorov-Smirnov (KS) statistics between behavioural and non-behavioural regions (Figure 4.2). The input factor sample matrix is separated into behavioural and non-behavioural regions using Equation 4.3.

$$x_b = \{x | y_i = f_i(x) \leq \bar{y}_i \text{ for all i}\} \tag{4.3}$$

where x_b is the set of behavioural inputs, $x = [x_1, ..., x_k]$ is the vector of k input factors, y_i is the output function and $\bar{y}_i$ is a predefined threshold value. Behavioural samples are defined as those which show absolute differences from the data of less than the average absolute difference seen across all model evaluations. The sensitivity index, S_i, for the i-th input factor, x_i, is the KS statistic calculated using Equation 4.4.

$$S_i = \max_{x_i} |F_i^B(x_i) - F_i^{\bar{B}}(x_i)| \tag{4.4}$$

where $F_i^B(x_i)$ and $F_i^{\bar{B}}(x_i)$ are the behavioural and non-behavioural Cumulative Distribution Functions (CDFs) respectively.

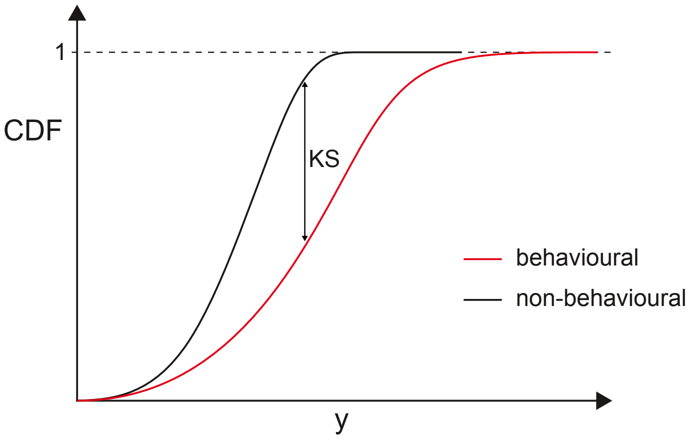

Figure 4.2: Cumulative distribution functions (CDFs) of behavioural and non-behavioural samples. The regional sensitivity analysis indices is the maximum distance between the two CDFs, i.e. the Kolmogorov-Smirnov (KS) statistic.

4.2.3 PAWN sensitivity analysis

PAWN (Pianosi et al., 2015) is a density-based method where sensitivity is measured by estimating the variation to the output distribution when removing the uncertainty (i.e. fixing the value) in one or more input factors. This variation is calculated from the measure of distance between the unconditional (when all inputs vary simultaneously) and conditional (when all inputs vary but x_i) CDF. The PAWN sensitivity index for the i-th input can then be calculated using Equation 4.5.

$$S_i = \max_{x_i} \max_{y} |F_y(y) - F_{y|x_i}(y|x_i)| \tag{4.5}$$

where $F_y(y)$ and $F_{y|x_i}(y|x_i)$ are the unconditional and conditional CDFs of the output. The inner maximum of Equation 4.5 is the KS statistic. The KS statistic depends on the fixed value of x_i. The outer maximum of Equation 4.5 extracts the maximum KS statistic over all the values of x_i (Figure 4.3).

However, a generic input-output dataset does not contain multiple samples with the same value of x_i. Therefore, conditional distributions are conditioned on similar values of x_i using Equation 4.6.

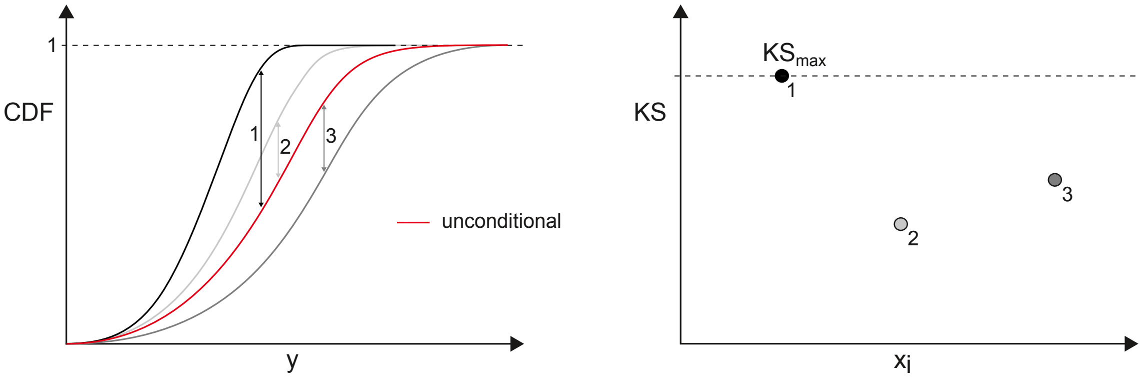

Figure 4.3: CDFs are plotted for y when all input factors are varied, i.e. unconditional (red), and when all input factors except x_i are varied, i.e. conditional (greyscale). There are multiple conditional CDFs because x_i is fixed at incremental values. The PAWN sensitivity analysis indices for x_i is the maximum KS statistic from the unconditional-conditional pairs.

$$S_i = \max_{j=1,\ldots,n} \max_y |F_y(y) - F_{y|x_i}(y|x_i \varepsilon \alpha_j)| \tag{4.6}$$

where α_j are n equally spaced intervals over the range of variation of x_i.

4.2.4 Variance-based sensitivity analysis

In variance-based sensitivity analysis (Sobol, 1993) the direct contribution of the i-th input factor to the variance of the output is defined by Equation 4.7.

$$S_i = \frac{V_{x_i}[E_{x_{\sim i}}(y|x_i)]}{V(y)} \tag{4.7}$$

where S_i is the sensitivity index, E is the expected value, V is the variance and $x_{\sim i}$ is a vector of all inputs factors but the i-th. An analytic solution to Equation 4.7 is typically impossible, therefore, numerical approximations are often used. Petropoulos & Srivastava (2016) approximate Equation 4.7 using a generic input-output dataset. They approximate $E_{x_{\sim i}}(y|x_i)$ as a linear combination of radial basis functions using Equation 4.8.

$$\hat{E}_i = \sum_{j=1}^{n} [a_j \exp\Big(-(x_i - w_j)^2\Big)] \tag{4.8}$$

where α_j and w_j are parameters that define the shape of the radial basis functions. The variance $V_{x_i}[E_{x_{\sim i}}(y|x_i)]$ is then approximated by the sample variance of $\hat{E}_i$ (Figure 4.4) and $V(y)$ is approximated by the variance of the sample output, y.

4.2.5 Assessing convergence

The non-influential group of input factors for a given screening threshold is defined by $x_0 = \{x_i \text{ when } \mu_i < T\}$ where x_i is the i-th input factor and μ_i is its (mean) sensitivity index. The threshold is calculated as $T = 0.05\Big(\max_{x_i}(\mu_i)\Big)$.

Screening convergence is assessed by measuring the stability in the partitioning. A summary statistic for the stability is the maximum width of the 95% confidence intervals across the non-influential input factors (Equation 4.9).

$$Stat_{screening} = \max_{x_i \epsilon x_0}(S_i^{ub} - S_i^{lb}) \tag{4.9}$$

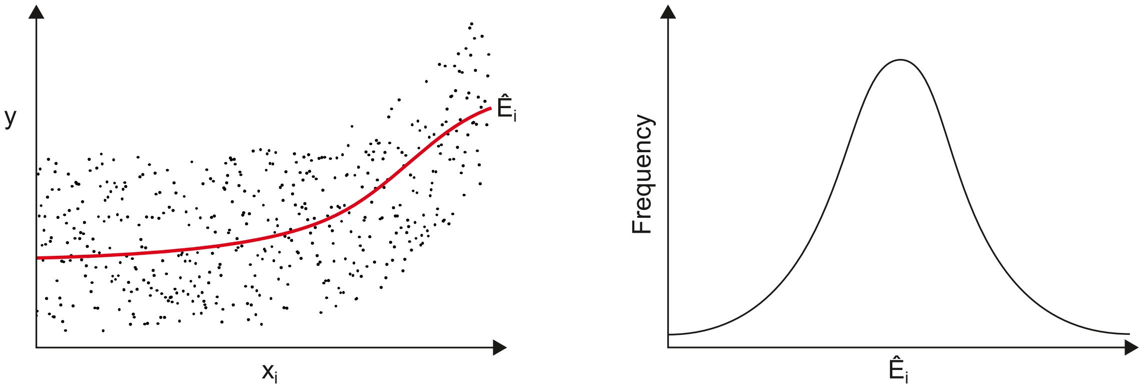

Figure 4.4: $Y - x_i$ plot with a linear combination of radial basis functions, $\hat{E}_i$, as a regression function (red). The variance of the regression function over all values of x_i is used as an approximation of $V_{x_i}[E_{x_{\sim i}}(y|x_i)]$ in Equation 4.7 to calculate the variance-based sensitivity analysis indices.

Screening convergence is reached when $Stat_{screening} < T$. This assumes screening convergence has been reached when the sensitivity indices for the non-influential input factors have converged. Finally, the screening of input factors into the non-influential group is validated using an Andres test (Andres, 1997).

4.3 Experimental setup

The experimental setup is discussed in four parts: the model, model output for the sensitivity analyses (y), uncertainty in rock properties (input factor space) and sampling the input factor space (x).

4.3.1 Model

An appropriate model is required for the global sensitivity analysis, that simulates the coupled processes occurring in the geosphere around heat-producing radioactive waste; uses an analogue for lower strength sedimentary rock; has appropriate uncertainty for a rock characterized as a GDF host rock; and is computationally efficient. Altogether, these criteria ensure that the results are applicable to understanding the THM processes surrounding heat-producing radioactive waste in lower strength sedimentary rocks.

The complex THM processes occurring in the geosphere around heat-producing radioactive waste are simulated by in situ heating experiments (e.g. Conil et al., 2012; Zhang et al., 2007a). Furthermore, the Opalinus Clay is an analogue for lower strength sedimentary rock (Towler et al., 2008). Therefore, the benchmarked in situ heating experiment model in Chapter 3 provides a realistic representation of heat-producing radioactive waste in lower strength sedimentary rock. The model is ideal because the experiment site is well characterized with uncertainty in rock properties similar to what would be expected in a lower strength sedimentary GDF host rock. The work is complimentary to the in situ experiment (Wileveau & Rothfuchs, 2003; Wileveau, 2005) and associated modelling (e.g. Gens et al., 2007; Zhang et al., 2007a; Wang & Kolditz, 2013; Garitte et al., 2017).

The axisymmetric model is preferred over a 3D model because its relatively short, approximately 35 minutes, computation time is appropriate for 1000s of model realizations. The computation time is expected to vary according to the sampled densities and Young's modulus because of the explicit time step, Δt (Equation 4.10). Further computation includes automatically reading and manipulating the results from text files into data structures appropriate for the sensitivity analysis. This is dependent on the number of elements in the model mesh. Adequate storage is also a constraint for 1000s of larger models.

$$\Delta t = \min \left| l^e \sqrt{\frac{\rho^e}{E^e}} \right| \tag{4.10}$$

where l^e is the mesh element lengths, ρ^e is the element density and E^e is the element Young's modulus.

4.3.2 Defining the model output

The fundamental structure of a global sensitivity analysis is to have input data, x $(k - by - n)$ and output data, y $(1 - by - n)$. Where k is the number of input factors and n is the number of model evaluations. The output data is typically envisioned as an observable property at a point in space and time. The analysis is fast and repeatable so the output vector can be translated spatially and temporally. More complex metrics can also be used, for example, model performance through time determined by the mean squared error compared with laboratory data.

In the analysis presented in this work, the outputs were defined as the mean effective stress, temperature, pore pressure and displacement at the sensor locations and through time. The mean effective stress was investigated because it is an important parameter for microseismicity and rock physics modelling. The temperature, pore pressure and displacement were investigated because these were the observable properties that the original laboratory experiment measured. Therefore, the sensitivity analysis ties the uncertainty in rock properties to the potential measurements.

4.3.3 Uncertainty in the rock properties

Modelling requires characterising the rock according to material parameters. The independent material parameters and their uncertainty ranges are referred to as the input factor space and described in Table 4.1. The characterization includes extensive laboratory testing and in situ experiments as would be expected for a GDF host rock during its pre-construction, construction and operation phases. This was an important consideration because it ensures that the uncertainty in rock properties used in the sensitivity analysis is appropriate.

Permeability, thermal conductivity and thermal expansion coefficient are typically described using vertical transverse isotropy values (e.g. Bock, 2001). However, an axisymmetric model with isotropic properties is used for the sensitivity analysis. The uncertainty ranges for the vertical transverse isotropy properties should be for isotropic rock, otherwise the uncertainty will be exaggerated by applying the relatively very large anisotropic range.

The probability distribution must also be considered before sampling. The default probability distribution in global sensitivity analyses is uniform (Pianosi et al., 2015). A uniform probability distribution is appropriate when both ends are bounded and no information regarding the probability between the ends is known (Iooss & Lemaitre, 2015). Other probability distributions that are appropriate when both ends are bounded are beta, binomial and triangular. A uniform probability distribution is assumed for the rock and fluid properties because laboratory testing is sparse (Bock, 2001; Mugler et al., 2006; Willeveau, 2005) and cannot be used to form a reliable probability distribution.

Input factors		Recommended	Minimum	Maximum	Unit	Citations
Fluid density	ρ_f	1000	998	1034	kg/m^3	De Wilde et al. (2010).
Grain density	ρ_g	2710	2680	2740	kg/m^3	Bock (2001).
Poisson's ratio	υ	0.295	0.24	0.33		Bock (2001); Willeveau (2005).
Friction angle	β	60	56	60	°	Chapter 3.
Tensile intercept	P_t	-0.018	-0.02	-0.018	MPa	Chapter 3.
Porosity	ϕ_{init}	0.16	0.1165	0.1625		Zhang et al. (2002); Zhang et al. (2004b).
Permeability	k_0	5.00×10^{-20}	4.08×10^{-20}	9.17×10^{-20}	m^2	Marschall et al. (2005); Gens et al. (2007).
Fluid stiffness	K_f	2012	1970	2310	MPa	Millero & Huang (2011); Rockfield, 2013b
Grain stiffness	K_g	7300	2000	9100	MPa	Zhang et al. (2007a).
Biot's coefficient	α	0.6	0.42	0.78		Willeveau (2005).
Viscosity	μ	1.00×10^{-9}	1.00×10^{-9}	1.085×10^{-9}	MPa.s	Rockfield Software Limited, 2013b.
Fluid heat capacity	c_f	4184	3985	4184	J/kg.K	National Physical Laboratory, 2018.
Solid heat capacity	c_s	800	800	1000	J/kg.K	Weber (1997); Knill (1998); Bock (2001). Zhang et al. (2007a).
Fluid thermal conductivity	λ_f	0.5846	0.563	0.609	W/m.K	National Physical Laboratory, 2018.
Solid thermal conductivity	λ_s	1.7	1.537	1.863	W/m.K	Mugler et al. (2006); Zhang et al. (2007a).
Rock linear thermal expansion coefficient	α_{lin}	1.7×10^{-5}	1.2×10^{-5}	2.1×10^{-5}	K^{-1}	Zhang et al. (2007a).
Fluid volumetric thermal expansion coefficient	$\alpha_{f,vol}$	3.4×10^{-4}	2.5×10^{-4}	3.4×10^{-4}	K^{-1}	National Physical Laboratory, 2018.
Solid volumetric thermal expansion coefficient	$\alpha_{s,vol}$	6.0×10^{-6}	4.5×10^{-6}	7.5×10^{-5}	K^{-1}	Noynaert et al. (2000); Zhang et al. (2007a).
Initial stress	θ_{init}	-4.8	-5.3	-4.3	MPa	Bossart & Wermeille (2003).
Initial pore pressure	p_f	0.9	0.163	1.055	MPa	Gens et al. (2007).
Initial temperature	T_{init}	15	14.43	18.15	°C	Zhang et al. (2007a).

Table 4.1: Input factor space for the Opalinus Clay in the experiment test site. The recommended values were used in the benchmark test (Chapter 3). Citations are provided for exact values. Complimentary data is reported in Thury & Bossart (1999); Floria et al. (2002) and Munoz et al. (2003).

4.3.4 Sampling the input factor space

Monte Carlo simulations represent uncertainty by randomly sampling the input factor space. Stratified sampling, e.g. Latin Hypercube sampling (LHS), provides improved coverage of the input factor space compared to random sampling (Forrester et al., 2008). The resultant sample is called a generic sample.

LHS splits each input factor uncertainty range into n non-overlapping, equal intervals and randomly samples each interval independently. Therefore, the sample consists of n sets of factor values with one sample in every interval across all input factors. A LHS forms a k-by-n matrix, x.

A number of LHS are generated and the one with the largest distance between the closest pair of points is used (Morris & Mitchell, 1995). This method is called maximin LHS and further improves the space filling properties of the design. Figure 4.5 demonstrates the space coverage of random sampling, LHS and maximin LHS.

A limitation of LHS is the size adaptability because of the stratification. If the sample size needs to be changed after a first series of computations, then it must be changed by multiples of two or three to maintain stratification. This can intuitively be done using hierarchical LHS (Garg & Stogner, 2017).

Input factor ranking methods may use a generic sample. However, input factor screening requires a one-at-a-time (OAT) based sample to isolate parameter interactions. Campolongo et al. (2011) show that a radial design OAT sample is superior for the EET. A radial design is one whereby starting from a random point in the generic sample hyperspace, one step in turn is taken for each input factor. The procedure is iterated a number of times with a different starting random point as to collect a sample of elementary shifts for each factor.

The EET uses an initial Latin hypercube sample with a chosen base sample size, n, to generate n one-at-a-time sample matrices which are described in Equation 4.11. These are concatenated to create a total sample size of N calculated in Equation 4.12.

$$B_{k+1,k} = \begin{bmatrix} b_{11} & b_{12} & \dots & b_{1k} \\ b_{21} & b_{22} & \dots & b_{2k} \\ \vdots & \vdots & \ddots & \vdots \\ b_{k+1,1} & b_{k+1,2} & \dots & b_{k+1,k} \end{bmatrix} \tag{4.11}$$

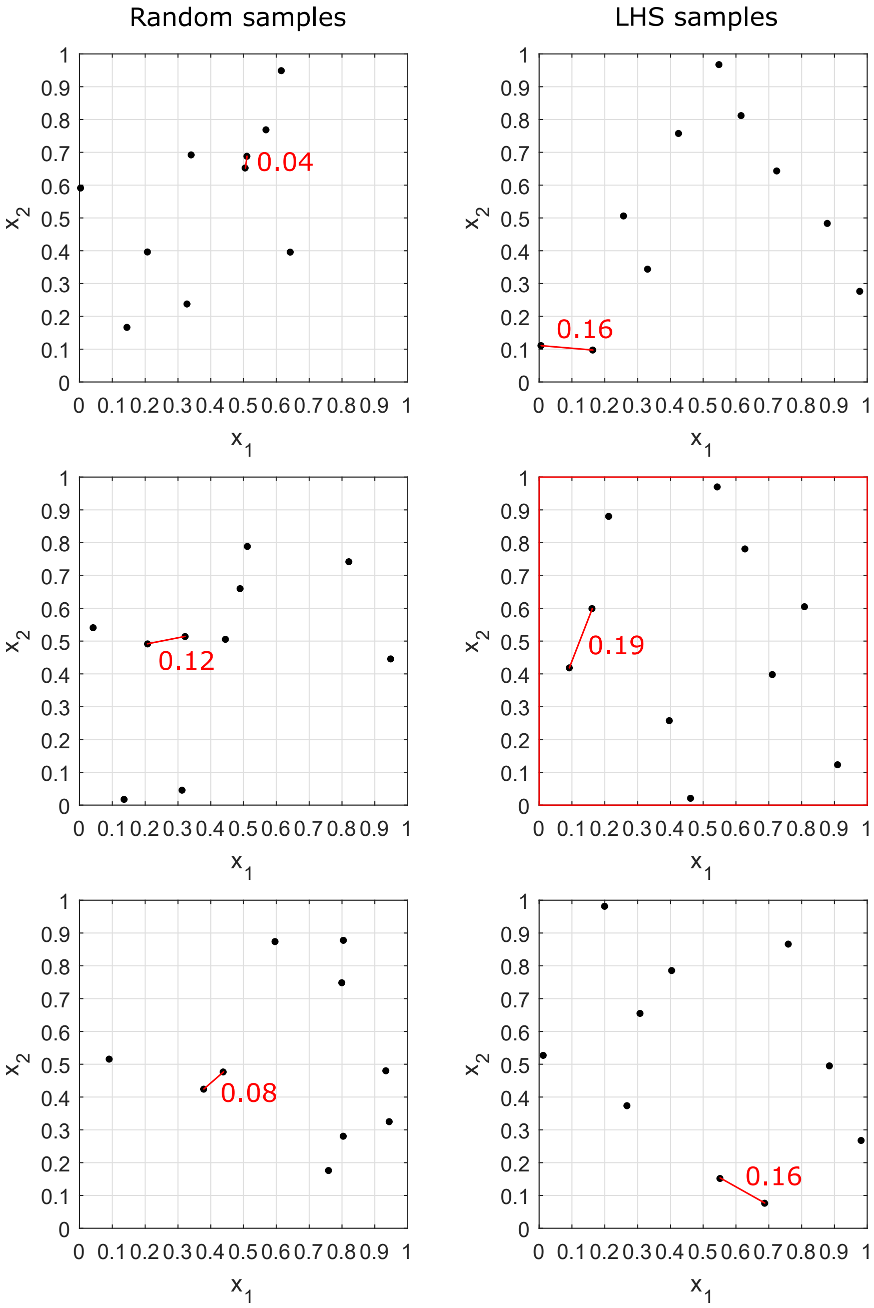

Figure 4.5: Three normalized random samples and three normalized LHS samples of x_1 and x_2. The LHS samples show a sample point within each grid line. The nearest neighbours and their separation (red lines and text) are used to assess the space coverage of the samples. The LHS samples show greater nearest neighbour separations than the random samples, therefore, better space coverage. The LHS sample with the maximum separation of nearest neighbours is selected as the maximin LHS sample (red box).

$$N = n(k+1) \tag{4.12}$$

The sample matrix is ordered such that its i^{th} row differs from some row above it in only the $(i-1)$ element. Each row is an independent sample describing a different model run. The one-at-a-time sample is generated using the SAFE toolbox (Pianosi et al., 2015).

Maximin LHS with $n = 100$ calculated the EET base sample. The final one-at-a-time sample matrix for the EET was 21-by-2200. Maximin LHS with $n = 1000$ calculated the multi-method approach sample matrix which was 11-by-1000. The 21 input factors were reduced to 11 input factors by input factor screening which is presented first. Convergence analyses are used to justify these sample sizes.

The screening was validated with an Andres test which requires two equally sized generic samples. An unconditional generic sample varies all of the input factors and a conditional generic sample varies the sensitive input factors only. The conditional generic sample would also be used for the multi-method approach, therefore, a large sample size of 1000 was selected as discussed above.

ELFEN data files are automatically generated using the sampled input factor values. A script was written to monitor CPU usage and submit models to maximise computational efficiency. Thus, the entire process from taking an ELFEN model and an uncertainty space to having x and y for the sensitivity analyses was automated.

4.4 Results

The primary focus is the mean effective stress output because it is a THM model prediction used in the following chapter to predict microseismic events. The temperature, pore pressure and displacement outputs are also investigated because these were the observable properties recorded in the HE-D experiment. Two general objectives are considered for each output: screening and ranking (Saltelli et al., 2008). Both of the objectives can support robust decision making assuming the model is a reliable representation of reality (Norton, 2015; Pianosi et al., 2016; Song et al., 2015), which is why the benchmarked model is used.

4.4.1 Mean effective stress

Figure 4.6 shows the EET results for a single location and time to illustrate a discrete component of the results. Figure 4.6a and Figure 4.6b show the input factors in the $\mu - \sigma$ plane (4.2.1). σ_{init} plots exactly as expected, having a total effect (μ) of 1 MPa, given its uncertainty range is 1 MPa and the input factor directly changes the mean effective stress. K_g has a relatively high σ value indicating a strong nonlinear effect on mean effective stress.

Figure 4.6a shows that higher indices have larger confidence bounds and Figure 4.6c shows that higher indices take longer to converge. As discussed in Section 4.2.5, screening convergence is reached when the input factors have converged around the threshold. Screening convergence typically occurs in significantly less model evaluations than ranking and indices convergence (Sarrazin et al., 2016). Input factors are shown to have converged to either above or below the screening threshold within the available dataset (Figure 4.6c).

The sensitivity analysis is spatial and temporal by repeating computations for the experiment sensor locations and through time. Figure 4.7 summarizes this data. The x-axis shows temporal variations and the intensity reflects the spatial variation. The observed spatial and temporal variations are related to the pore pressure. The greater the pore pressure perturbation, due to proximity to the heaters or duration of heating, the greater the sensitivity of the input factors. The input factors that define the initial conditions are an exception and decrease in sensitivity. The automatically calculated screening threshold is 50.0 KPa. The ρ_f, ρ_g, β, P_t, K_f, μ, c_f, λ_f, α_g, and T_{init} are screened. The bottom row shows that screening convergence is reached at all locations and times.

The screening result is validated using Figure 4.8 which is an Andres test. The strong correlation and orientation shows that the output variability is the same when varying all input factors and when varying all input factors but those in x_0.

The Andres test has limitations as a validation method which are addressed in Sarrazin et al. (2016). However, the method proposed therein proved too computationally expensive due to the requirement of multiple times more model evaluations. The first limitation of the Andres test is that it is a visual analysis open to misinterpretation and bias. Secondly, the procedure only considers one screening threshold,

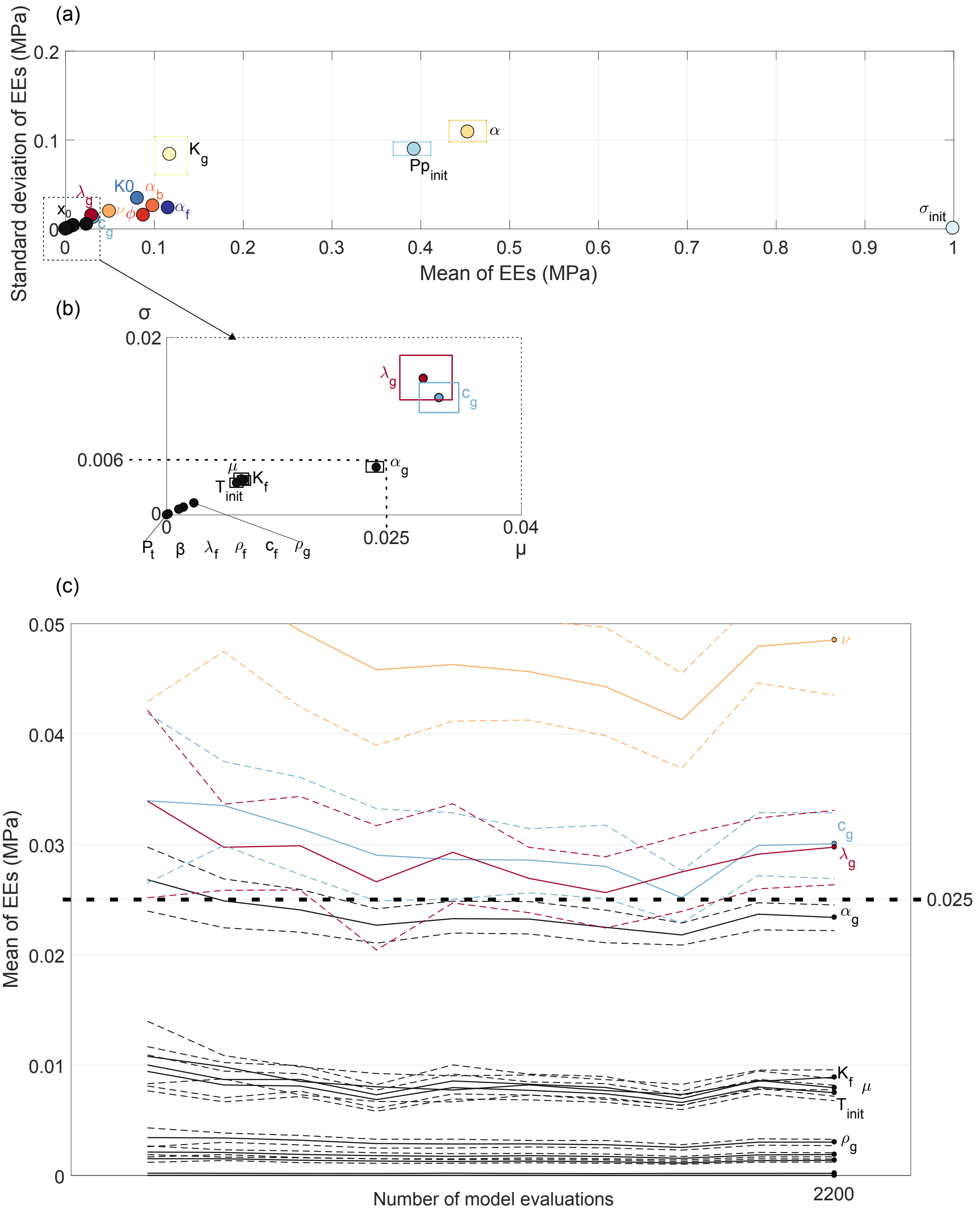

Figure 4.6: (a) Mean (μ) - standard deviation (σ) plane plot of the EEs computed for mean effective stress at sensor 5 (radial distance 3.34 m and depth 11.26 m) and 152 days after heating started. Confidence bounds are derived using bootstrapping and plotted as boxes. (b) is zoomed towards the screening thresholds. (c) Convergence plot of μ computed by repeating calculations using a decreasing number of samples. Confidence bounds are derived using bootstrapping and plotted as dashed lines.

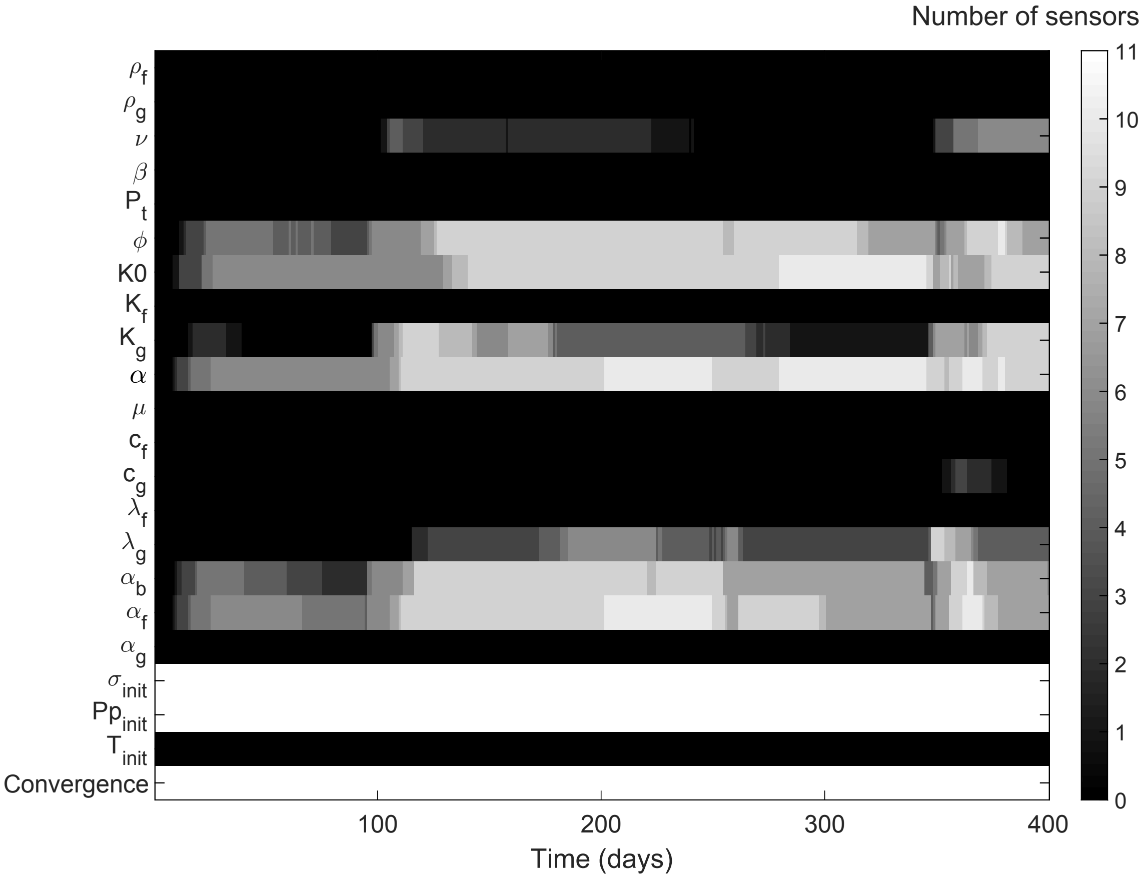

Figure 4.7: Time varying heat map of input factors where intensity indicates the number of sensors at which the input factor is not screened and EEs are computed for mean effective stress. Only the initial stress and initial pore pressure are not screened during the first 8 days because heating has not started. 10 input factors are screened at all sensors and times. The bottom row represents screening convergence which is achieved at all sensors and times.

therefore, a positive result does not determine whether more input factors could have been screened.

The conditional LHS model evaluations from the Andres test, with 1000 samples across the sensitive input factor space, is reused in the multi-method approach for input factor ranking. Figure 4.9a is a spatial and temporal summary of the multi-method sensitivity indices. Clustering of the input factors against the y-axis shows that the spatial variation in input factor indices is minimal. The most sensitive

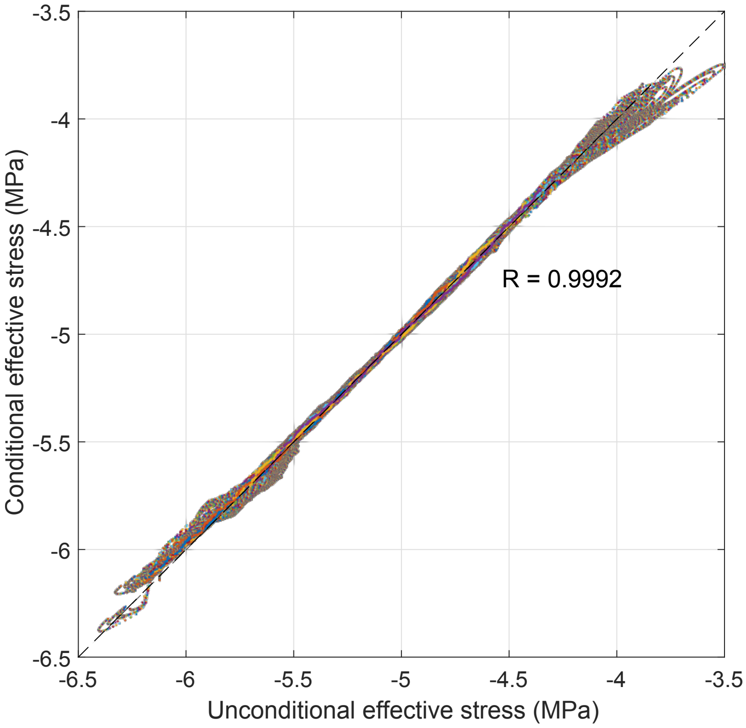

Figure 4.8: Visual validation strategy (Andres, 1997; Tang et al., 2007; Nossent et al., 2011) for assessing the adequacy of the screening. The mean effective stress output at all sensors and times of an unconditional group of 1000 LHS samples across the whole input factor space is compared to a conditional group of 1000 LHS samples across the sensitive input factor space. The correlation coefficient (R) is 0.9992 and the alignment is along a 45° line indicating that the output variability in both groups is the same.

input factors for mean effective stress are σ_{init}, then p_f, and α.

The sensitivity indices of these three most sensitive input factors are plotted over time in Figure 4.9b. σ_{init} and p_f decrease in sensitivity as the system is perturbed, whereas α increases in sensitivity. The other input factors increase in sensitivity similar to α. This is expected because the input factors affecting the initial conditions should be most sensitive at the beginning.

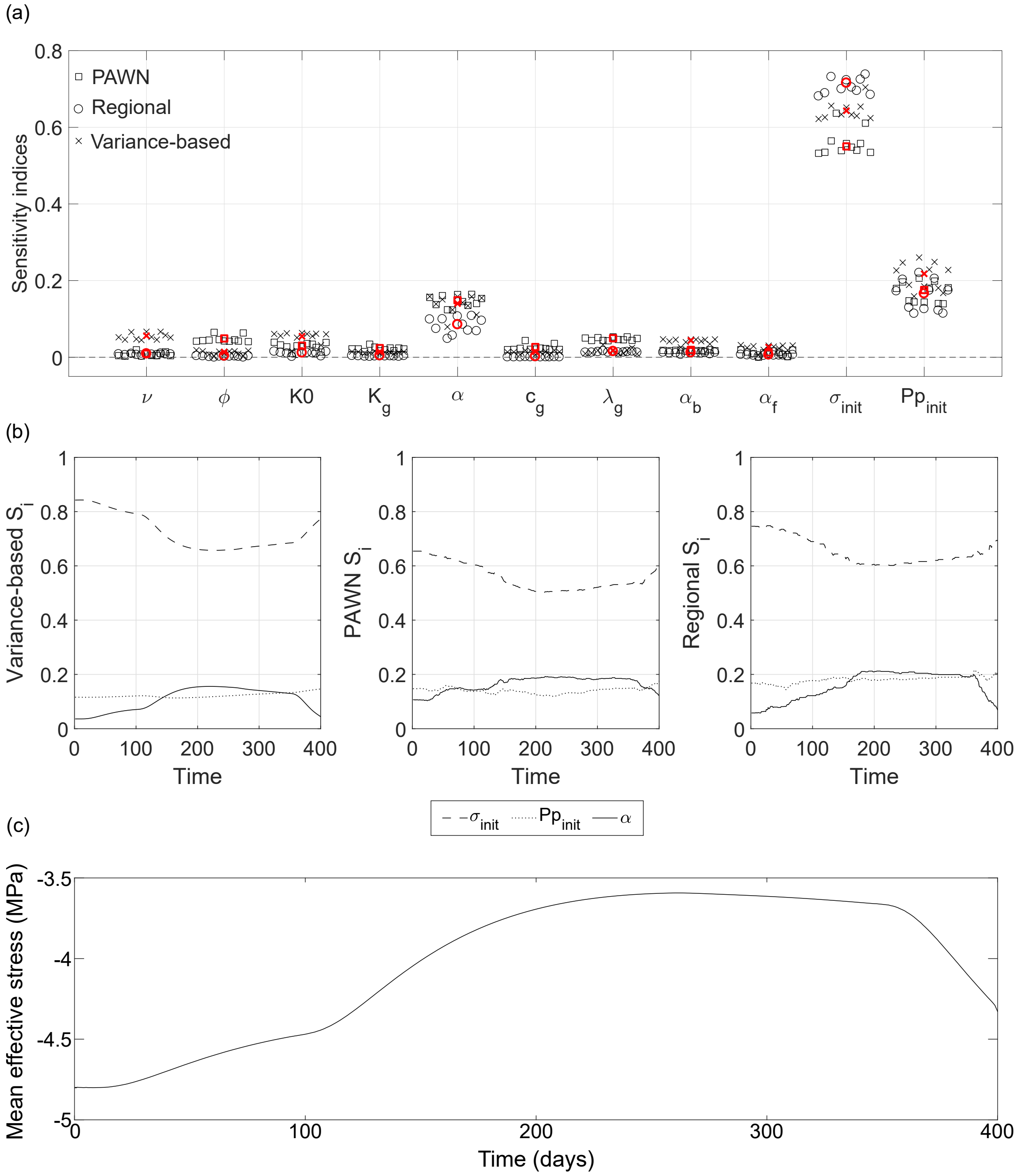

Figure 4.9: (a) Multi-method sensitivity indices (averaged over time) of the reduced set of input factors for the mean effective stress output. Black markers distinguish each sensor and red markers indicate the mean of the sensors. Clustering indicates that there are no spatial effects (the horizontal separation is for visualization purposes). (b) Variance-based sensitivity indices of the three most sensitive input factors for mean effective stress over time at a representative sensor (5: radial distance 3.34 m and depth 11.26 m). For all sensors, the temporal trend is the mean effective stress trend shown in (c). The PAWN and regional indices show the same trends.

4.4.2 Temperature

Figure 4.10 is a summary of the global sensitivity analysis for the temperature output. Figure 4.10a is a summary of the screening and Figure 4.10b is a summary of the ranking. The automatically calculated screening threshold is 0.186 °C. Only four input factors are not screened for temperature: ϕ, c_g, λ_g, T_{init}. Screening convergence is reached at all locations and times.

T_{init} cannot be screened for the temperature output but can for the mean effective stress output indicating the importance of an output focus when modelling uncertainties. Advection related input factors and ρ_f, ρ_g, c_f and λ_f are insensitive for temperature, despite being associated with the thermal field calculations.

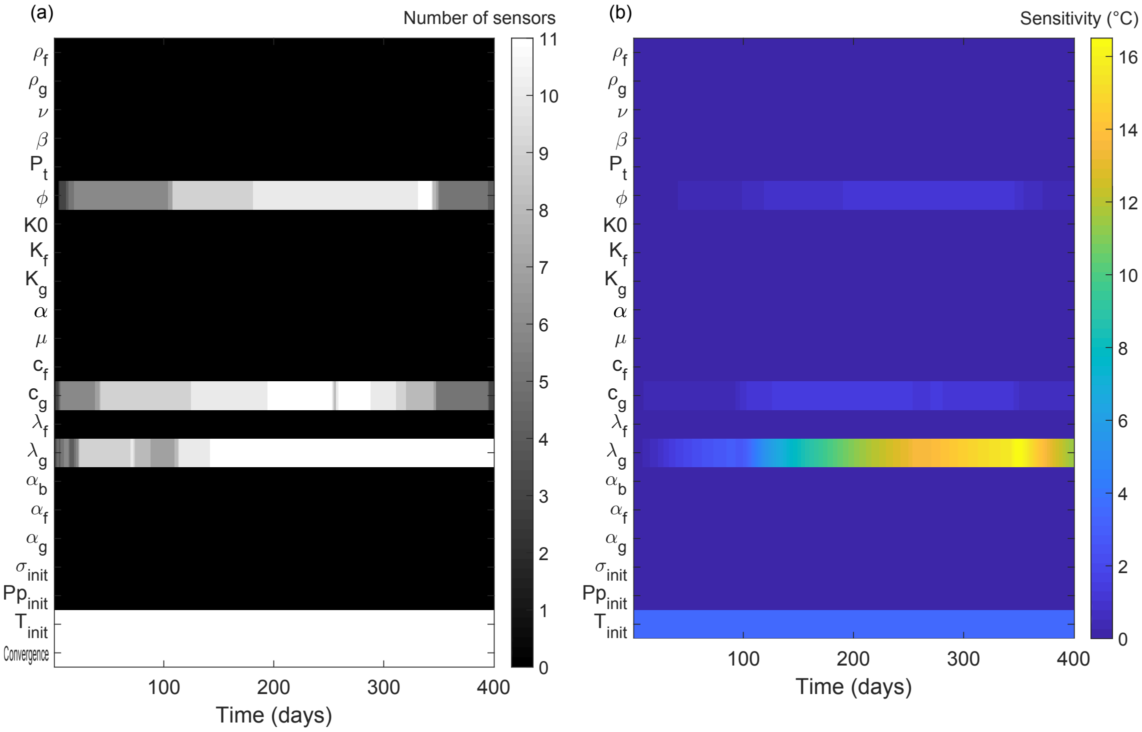

Figure 4.10: EEs computed for temperature. (a) Time varying heat map of input factors where intensity indicates the number of sensors at which the input factor is not screened. The bottom row represents screening convergence which is achieved at all sensors and times. (b) Time varying heat map of input factors where intensity indicates the combined mean and standard deviation sensitivity indices averaged over all sensors.

λ_g is the most sensitive input factor for temperature. T_{init} is the second most sensitive, however, the model assumes a homogeneous initial temperature field which is more uncertain than reality.

4.4.3 Pore pressure

Figure 4.11 is a summary of the global sensitivity analysis for the pore pressure output. Figure 4.11a is a summary of the screening and Figure 4.11b is a summary of the ranking. The automatically calculated screening threshold is 42.0 KPa. Seven input factors are screened: ϕ_f, ϕ_g, β, P_t, c_f, λ_f and σ_{init}. Screening convergence is reached at all locations and times.

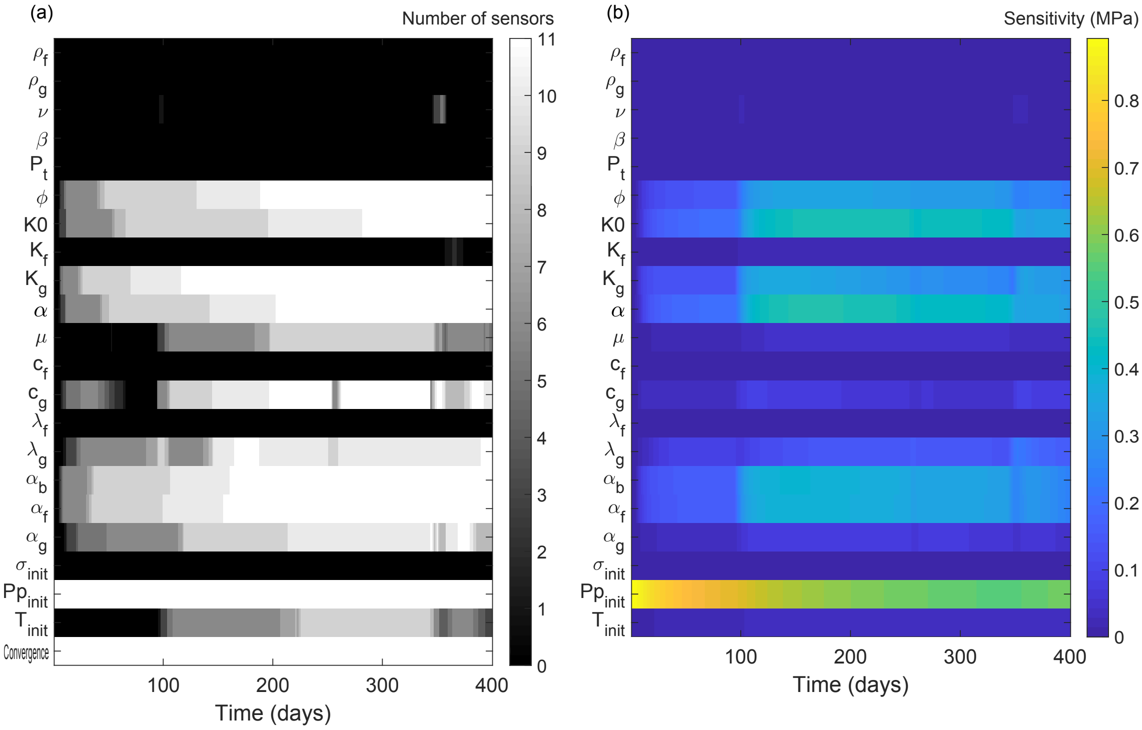

Figure 4.11: EEs computed for pore pressure. (a) Time varying heat map of input factors where intensity indicates the number of sensors at which the input factor is not screened. The bottom row represents screening convergence which is achieved at all sensors and times. (b) Time varying heat map of input factors where intensity indicates the combined mean and standard deviation sensitivity indices averaged over all sensors.

These are also screened for mean effective stress, except for σ_{init} which directly influences the mean effective stress but is not sensitive for pore pressure. Input factors that are screened for mean effective stress but not in this analysis for pore pressure are K_f, μ, α_g and T_{init}. Note that the screening threshold is 8 KPa less than the mean effective stress screening threshold because the pore pressure output range has less uncertainty.

The most sensitive input factors for pore pressure are p_f, then α and $K0$. The least sensitive input factor (after screening) is υ, which can be screened at all locations and times except for a maximum of five sensor locations over 17 days.

4.4.4 Displacement

The displacement output range was low and the automatically picked threshold was lower than any realistic significance level. A new threshold (1.2×10^{-5} m) was selected based on the extensometer accuracy in the anchored displacement system used in the field test (Zhang et al., 2007a). Figure 4.12 is a summary of the global sensitivity analysis for the displacement output. Figure 4.12a is a summary of the screening and Figure 4.12b is a summary of the ranking. Eight input factors are not screened for displacement: ϕ, $K0$, K_g, α, λ_g, α_b, α_f and p_f. Screening convergence is reached at all locations and times. All of these were also sensitive for mean effective stress.

The most sensitive input factors for displacement are α, then ϕ, then $K0$. This shows that hydro-mechanical coupling is important for simulating heating driven displacement in lower strength sedimentary rocks.

4.5 Discussion

Table 4.2 summarizes the screening and ranking results for the different outputs. The ρ_f, ρ_g, β, P_t, K_f, c_f and λ_f are screened for all of the investigated outputs. The μ, α_g and T_{init} are additionally screened for mean effective stress.

$\alpha_{f,vol}$ is sensitive for mean effective stress, pore pressure and displacement; and μ is sensitive for pore pressure. This demonstrates that the fluid properties cannot be entirely assumed for a GDF. However, ρ_f, K_f, c_f and λ_f should be.

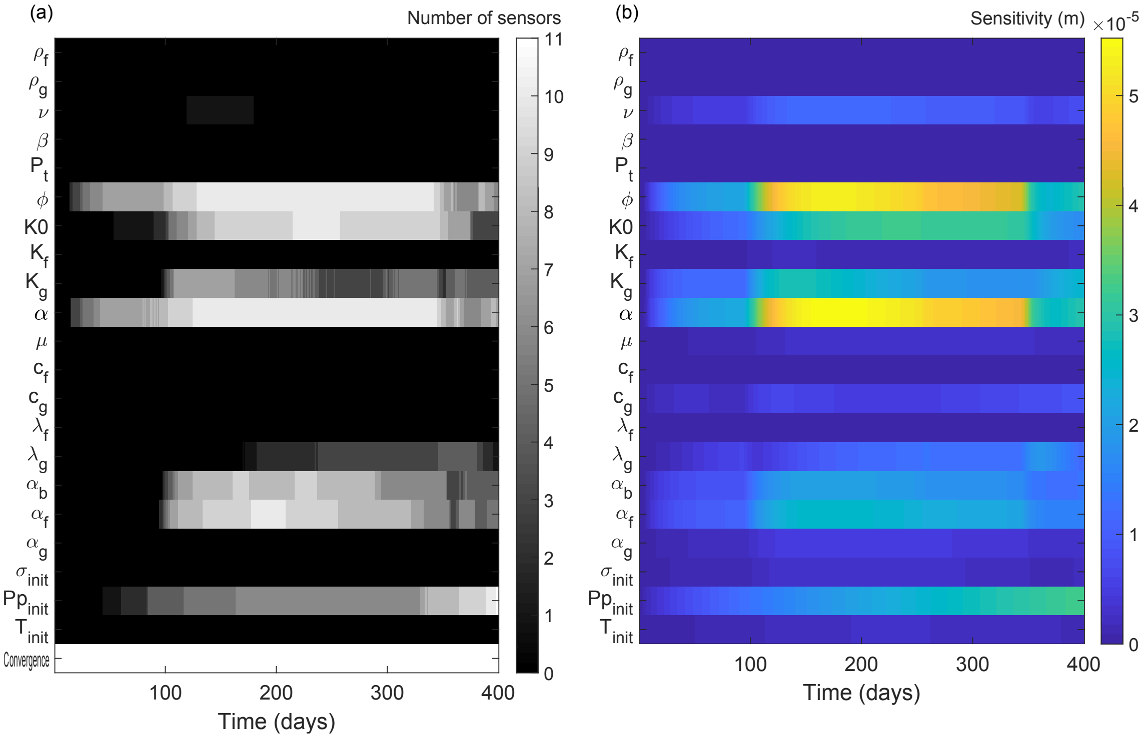

Figure 4.12: EEs computed for x-displacement. (a) Time varying heat map of input factors where intensity indicates the number of sensors at which the input factor is not screened. The bottom row represents screening convergence which is achieved at all sensors and times. (b) Time varying heat map of input factors where intensity indicates the combined mean and standard deviation sensitivity indices averaged over all sensors.

The initial conditions rank amongst the most sensitive input factors for two reasons. Firstly, in situ stress and pore pressure are difficult to measure (Martin & Lanyon, 2003; Nussbaum et al., 2014). Secondly, it is efficient to assume homogeneous initial conditions in a model despite the excavation and borehole perturbations.

α also ranks amongst the most sensitive input factors. The reason is that the uncertainty in the value is relatively high compared with other normalized input factor uncertainties. Therefore, Biot's coefficient is a prime candidate for uncertainty reduction efforts. Permeability is often the focus of uncertainty reduction (Marschall et al., 2005), however, whilst $K0$ ranks highly it is less sensitive than α for all outputs.

Convergence was reached for the base sample size of 100 with 21 input factors

Rank	Mean effective stress	Temperature	Pore pressure	Displacement
1	θ_{init}	λ_g	p_f	α
2	p_f	T_{init}	α	ϕ_{init}
3	α	c_s	$K0$	$K0$
4	λ_g	ϕ_{init}	α_{lin}	p_f
5	α_{lin}		$\alpha_{f,vol}$	K_g
6	$K0$		ϕ_{init}	$\alpha_{f,vol}$
7	υ		K_g	α_{lin}
8	$\alpha_{f,vol}$		λ_g	λ_g
9	K_g		$\alpha_{s,vol}$	
10	ϕ_{init}		c_s	
11	c_s		μ	
12			T_{init}	
13			υ	

Table 4.2: Summary table of the screened and ranked input factors for mean effective stress, temperature, pore pressure and displacement outputs.

(total sample size of 2200). Convergence demonstrates that the sample size was large enough to calculate a robust result. However, the exact sample size within which convergence is achieved varies. Therefore, a sample size of less than 2200 for 21 input factors cannot be recommended for future work.

The result was validated by an Andres test that showed that the screening thresholds were not too high (Figure 4.8). Therefore, no influential input factors are screened. However, a limitation of the validation procedure is that it does not show whether the screening thresholds were is too low. It is possible that non-influential input factors are not screened. If non-influential input factors are not screened, then the screening has not been fully effective.

The methods and sample sizes used are successfully demonstrated for coupled THM finite element models and are recommended for improving the amount of data provided by geomechanical models. It is essential that the sample generation, conversion from one model to 1000's of models, submission of models to evaluation and post-processing of results are all automated. The results presented are valid for thermally driven THM coupled processes in lower strength sedimentary rocks characterized at an URL.

Chapter 5

Microseismic modelling

5.1 Introduction

Surface and subsurface geophones are used to monitor microseismic activity during mining (Dou et al., 2009; Wang et al., 2017), reservoir production (Maxwell et al., 2010) and propagation of hydraulic fracturing (Mayerhofer et al., 2006; Patterson et al., 2018). Microseismic monitoring may be used to predict rock bursts (Zhao et al., 2018b). Characterizing the spatial and temporal variations in microseismicity can be used to assess changes in the stress field (Gischig et al., 2018) and potentially perturbations in fluid pathways (Grechka et al., 2010). Furthermore, the evaluation of microseismic failure mechanisms can be used to evaluate the rock mass at the source (Hazzard & Young, 2002).

Calibrating geomechanical models with microseismicity has the potential to provide remote, 3D and temporal information. Studies linking geomechanical, fluid flow and seismic modelling are improving predictions of the sub-surface response to fluid and stress perturbations and mechanical deformation (Herwanger & Koutsabeloulis, 2011). Models can be used to predict microseismicity and improve quantitatively the link between physical processes occurring to stress changes, rock failure and seismicity (Angus et al., 2015).

Figure 5.1 is a conceptual model for shear failure in the host rock surrounding HLW and spent fuel disposal tunnels after backfilling. The hypothesis is that rising pore pressure during heating (Gens et al., 2007; Delage et al., 2000; Mohajerani et

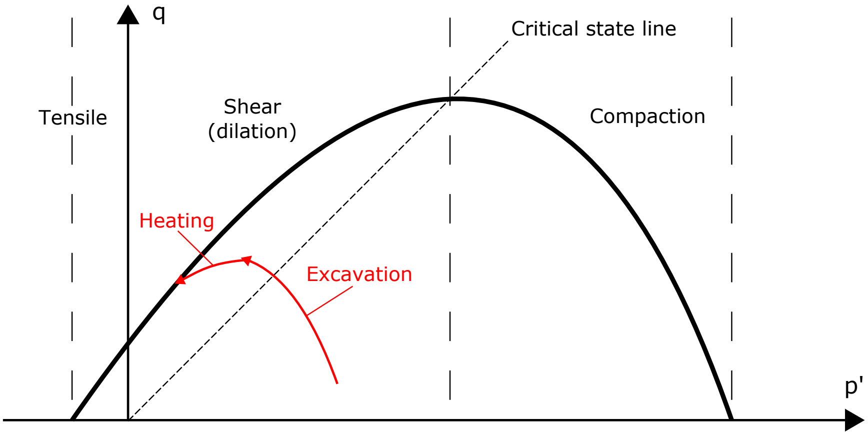

Figure 5.1: Schematic diagram illustrating an SR3 yield envelope in p'-q space. Red lines are hypothetical stress plotting describing a stress path to a potential shear-type yield event. The deviatoric stress increases when the facility is built and the mean effective stress decreases when the heating causes pore pressure to increase.

al., 2012) combined with a reduced radial stress caused by the excavation (Jaeger et al., 2007) may induce shear failure in lower strength sedimentary host rocks.

If geophones are installed to monitor microseismic activity during construction and operation, then continued microseismic monitoring of tunnels post-emplacement but still within the operation stage is feasible, because the facility will be operational for years after heat-producing waste has been emplaced (Watson et al., 2009). Microseismic monitoring may provide insights into the pore pressure, the swelling pressure of the engineered backfill material and the possibility of shear enhanced flow (Lisjak et al., 2016; Zou et al., 2017).

A key aim in this chapter is to test the hypothesis (Figure 5.1) using integrated THM modelling and microseismic modelling to identify scenarios in which it may occur. This is achieved using numerical methods similar to the previous chapters and combining them with a microseismic modelling technique from Angus et al. (2010). The calculations are repeated for scenarios that are sampled with a maximin Latin hypercube (Section 4.3.4; Morris & Mitchell, 1995). Microseismic events are then mapped onto the sample space to identify depths, in situ stress, in situ pore pressure and tunnel support pressure scenarios that may have microseismicity. It is proposed that continued microseismic modelling after backfilling HLW and spent fuel disposal tunnels in these scenarios will provide insights into the swelling pressure of the engineered backfill material and pore pressure development.

5.2 Experimental setup

5.2.1 Model

The RWM lower strength sedimentary host rock concept (Section 2.1; RWM, 2016a) is assumed (Figure 5.2). The material model determined in Chapter 3 is used to represent the lower strength sedimentary host rock.

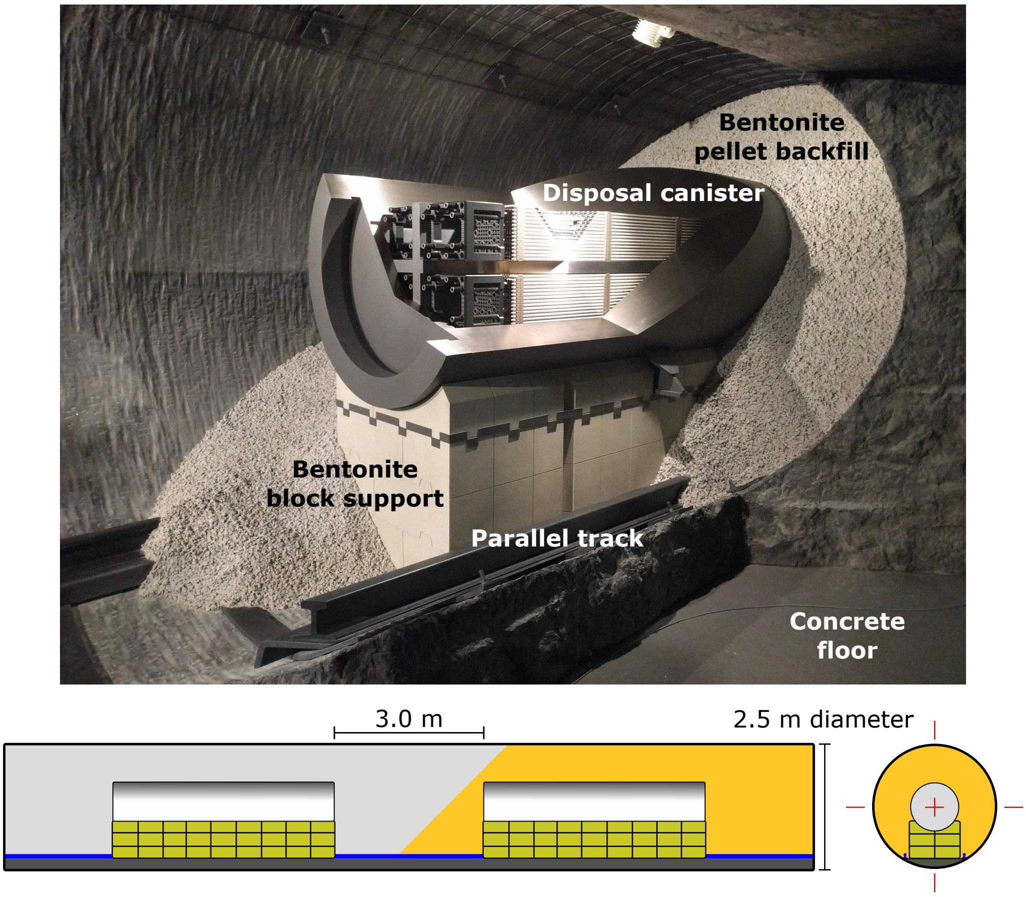

Figure 5.2: Photograph of a disposal canister on block support with pellet backfill in a circular disposal tunnel taken at Grimsel Test Site. Diagram of the RWM lower strength sedimentary host rock concept for a HLW and AGR spent fuel disposal tunnel (edited from RWM, 2016a).

The model is illustrated in Figure 5.3. The model is similar to the axisymmetric heater test model in Chapters 3 and 4. An axisymmetric model is used to reduce computation time because of the number of model runs required to represent the range of scenarios. The axisymmetric assumption is validated in Chapter 3.

The waste canisters are emplaced horizontally, therefore, the vertical stress must be applied parallel to the x-axis and the horizontal stress factor must be applied parallel to the y-axis (Figure 5.3). This is different to the axisymmetric heater test model (Chapters 3 and 4) because that had a uniform initial stress. The axisymmetric assumption means that the out of plane horizontal stress factor is 1.

A section of the 800 m long tunnel is simulated assuming the ends of the tunnel do not affect the entirety of its length. The baseline inventory has 38 % HLW canisters and 55 % AGR spent fuel canisters. There is no information on the relative positioning of different waste canisters along the disposal tunnel. Therefore, a HLW canister and an AGR spent fuel canister are simulated within the section of disposal tunnel. This model uses symmetry to simulate three possible mid-canister spaces as indicated in Figure 5.3.

The first stage in the model simulates the excavation of the tunnel. The second stage in the model simulates the placement of heat producing waste and backfilling of the tunnel. The placement of heat producing waste and backfilling are simulated as concurrent.

The excavation is simulated by removing a zero-displacement condition at the backfill-rock interface, allowing the rock to relax into a lower Young's modulus material. The material then provides some support to the excavation surface and the Young's modulus value is determined to represent the tunnel support, similar to Lisjak et al. (2015).

The heating is simulated using an internal heat generation load applied to the surfaces representing the canisters. Load curves are applied to simulate the representative power curves (Bond & Watson, 2012) of the different canisters over time (Figure 5.4). A material is required to apply the internal heat generation load (Rockfield Software Limited, 2013b). Therefore, the excavation cannot be simulated by removing the material, hence the alternative excavation method.

There are two pressures from the engineered backfill to the rock interface. The backfill emplacement pressure is a mechanical load exerted during and sustained by

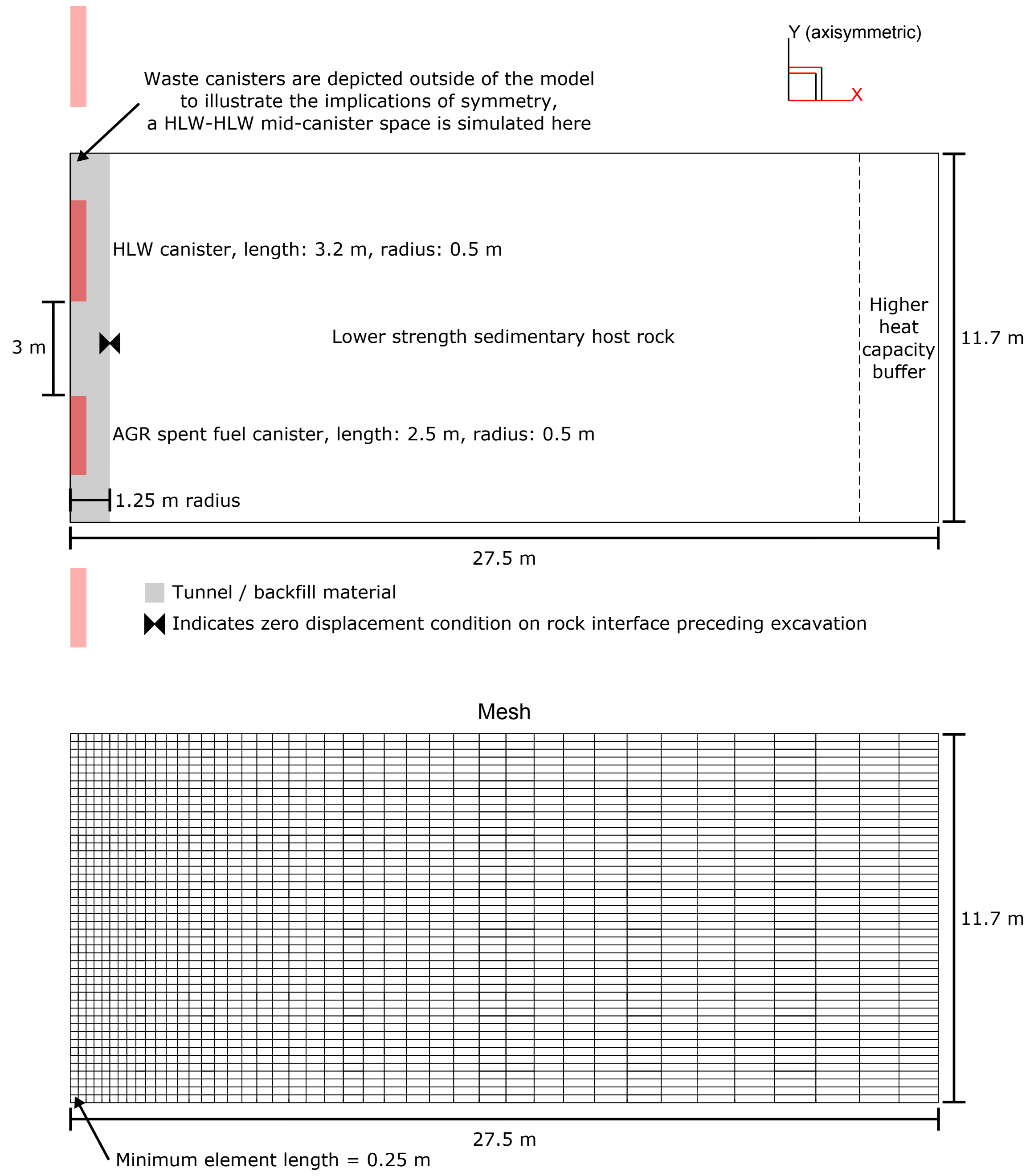

Figure 5.3: An axisymmetric model with y-axis symmetry of a 1.25 m radius, circular disposal tunnel. Boundaries are zero-displacement and temperature reflective. A higher heat capacity buffer zone is attached to the far-field to reduce the required model size. The waste canisters have 3 m spacing. Waste canisters are illustrated above and below the model to show that symmetry is used to simulate three different mid-canister spaces: HLW-HLW, HLW-AGR spent fuel and AGR spent fuel-AGR spent fuel. The mesh has square elements for the canisters and tunnel, and widens towards the far-field.

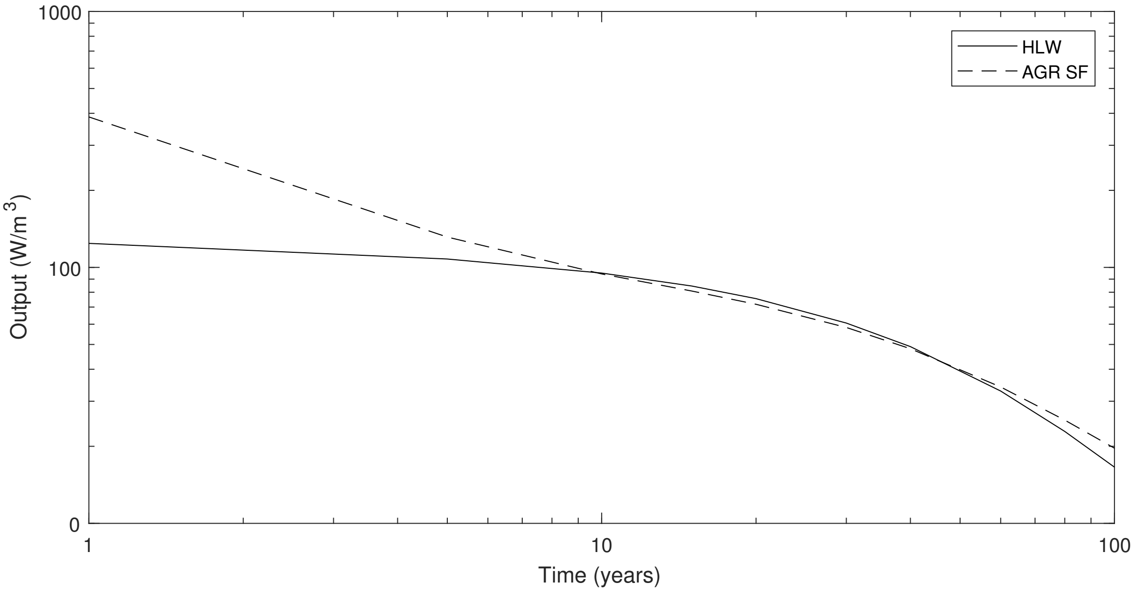

Figure 5.4: Representative power curves for the HLW and AGR spent fuel disposal canisters. The functions for these curves are in Bond & Watson (2012). Disposal canisters will be emplaced into the facility at variable and undetermined times after time = 1 year.

the pellet emplacement (Dixon et al., 2011). The backfill swelling pressure refers to the pressure exerted onto the rock interface by the backfill material as it swells during saturation (Shirazi et al., 2010). The saturation rate is uncertain and the swelling pressure is an important part of the engineered barrier system. The backfill emplacement pressure and backfill swelling pressure are simulated as forces applied from the backfill material to the rock interface. The backfill swelling pressure is applied over a logistic curve reaching a maximum at 30 years.

5.2.2 Input factor ranges for sensitivity analysis

The RWM facility concept for lower strength sedimentary host rocks has a depth range of 200 to 1000 m (RWM, 2016a). The depth range represents a range of scenarios rather than a meaningful uncertainty because the depth will be known accurately when the facility site is chosen. The following is an attempt to map microseismic events to the current range of scenarios to provide a measure of the feasibility for microseismic monitoring after backfilling the tunnels. A range of scenarios also exists for the horizontal stress factor, pore over-pressure or under-pressure, tunnel support pressure, backfill emplacement pressure and backfill swelling pressure.

The depth range is simulated as an initial vertical stress assuming overburden stress only, an average overburden density equal to the host rock and 9.81 ms^{-2} acceleration due to gravity. The in situ stress and pore pressure are explored based on possible depths, reasonable horizontal stress factors and under- and over-pressure scenarios. The horizontal stress factor uncertainty is 1.1 to 0.3, where 0.3 is the minimum horizontal stress factor at Mont Terri (Nussbaum et al., 2014). Low permeability, over-consolidated rocks may be over-pressured (Broichhausen et al., 2005; Drews et al., 2018; Liu et al., 2019). Furthermore, due to excavation ventilation and long operation times, the near-field may be under-pressured (Bond et al., 2013). The backfill emplacement pressure may be 0 to 1 MPa depending on the emplacement mechanism, e.g. blocks or pellets (Dixon et al., 2011; Garcia-Sineriz et al., 2015). Pellets are emplaced mechanically under pressures greater than 0.2 MPa (Keto et al., 2009). The support is simulated by a low Young's modulus material since a material is required in the axisymmetric model to simulate internal heat generation. Hoek (1998) shows that less than 5 % strain is expected for a 8 m radius tunnel at 500 m depth in a weak rock with 20 % of in situ stress as tunnel support pressure. The Young's modulus range was retrospectively determined to provide an effective tunnel support pressure of 1 % to 12.5 % of the initial vertical stress (Figure 5.5). 12.5 % is lower than the tunnel support investigated by Hoek (1998) but this is reasonable because the tunnel radius is only 1.25 m compared to 8 m in Hoek (1998). The backfill swelling pressure uncertainty is 0.1 to 4 MPa.

The backfill swelling pressure and its loading curve are very uncertain. The SKB Prototype Repository experiment in fractured Äspö diorite investigates the swelling pressure of MX-80 bentonite buffer over three years (Johannesson et al., 2007). One deposition hole (3) measured a swelling pressure up to 0.38 MPa and another (1) measured a swelling pressure up to 7.0 MPa, 5.5 MPa and 4.1 MPa, at three radial distances within the buffer. The measurements closest to the rock interface observe a pressure increase over a logistic curve which is also observed in simulations (Cleall et al., 2006). The measured (Johannesson et al., 2007) and simulated (Cleall et al., 2006) swelling pressures increase with proximity to the rock interface because the degree of saturation increases towards the rock interface. However, the rock interface

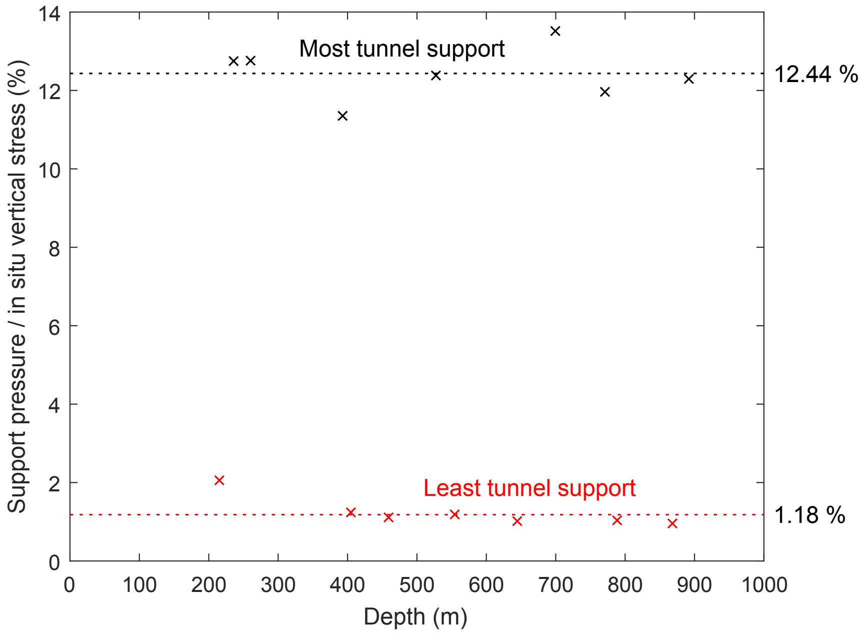

Figure 5.5: Tunnel support pressure percentage of in situ vertical stress for a range in depths for the model runs with the least tunnel support pressure (red) and most tunnel support pressure (black).

pressure is not measured and may observe a decrease relating to the quality of the buffer-rock interface contact. The fractured diorite hydraulic conductivity, 10^{-9} to 10^{-12}, is higher than Opalinus Clay hydraulic conductivity, characterized as less than 10^{-12} (Bossart et al., 2002). Therefore, the buffer will saturate significantly slower in Opalinus Clay. Furthermore, different backfill compositions will have different swelling pressures (e.g. Plötze et al., 2007).

The input factor space (Table 5.1) is sampled with a maximin Latin hypercube (Morris & Mitchell, 1995) and sample size of 1000.

5.3 Microseismic modelling

5.3.1 Thermo-hydro-mechanical and microseismic modelling

The microseismic modelling is linked to the coupled THM simulation using a static results file at a user specified output frequency. The results file contains various parameters including pore pressure, static elasticity and the stress tensor. The

Property	Minimum	Maximum	Unit
Depth	200	1000	m
Horizontal stress factor	0.3	1.1	
Pore over-pressure ratio	0.9	1.1	
Tunnel support pressure	1	12.5	%
Backfill emplacement pressure	0	1	MPa
Backfill swelling pressure	0.1	4.0	MPa

Table 5.1: The input factor ranges explored for microseismic modelling. The model initial stress and pore pressure are calculated using the depth, horizontal stress factor and pore over-pressure ratio sample values.

output frequency should be high for microseismic modelling to reflect the continuous nature of microseismic monitoring and constrain the temporal occurrence of events and related changes in stress.

5.3.2 Microseismic event distribution

Plastic deformation occurs in the simulation when the stress path reaches the yield surface in p'-q space. The mode of failure can be characterized as tensile, shear or compaction depending on the location of the stress path on the yield surface (Crook et al., 2006; Thornton & Crook, 2014). If failure occurs, its location, time and mode are flagged by the failure index parameters output to the static results file. Therefore, the spatial and temporal evolution of the various modes of failure within the rock are monitored. Based on the assumption that failure is not aseismic (Verdon et al., 2011; Angus et al., 2015) the microseismic event distribution is monitored.

5.3.3 Microseismic source magnitude and mechanism

The pre- and post-failure effective stress tensor, σ'_{ij}, are evaluated using Equation 5.1.

$$\sigma'_{ij} = \sigma_{ij} - \alpha p_f d_{ij} \tag{5.1}$$

where σ_{ij} is the stress tensor, α is Biot's coefficient, p_f is pore pressure and d_{ij} is the Kronecker delta function.

The eigen-solution of the differential effective stress tensor, $D\sigma'_{ij} = \sigma'^{post}_{ij} - \sigma'^{pre}_{ij}$, is evaluated to define the P-, T- and B-axis. Silver & Jordan (1982) show that fixing a Cartesian reference frame in 3D simplifies the moment retrieval problem. The pseudo scalar seismic moment, M_0, is calculated using Equation 5.2.

$$M_0 = \frac{(m_1^2 + m_2^2 + m_3^2)^{1/2}}{2} \tag{5.2}$$

where m_1 is M_{11}, m_2 is M_{22} and m_3 is M_{33} of the eigen-solution.

The pseudo scalar seismic moment has unit of N/m^2, whereas the actual seismic moment has unit of Nm (Hanks & Kanamori, 1979). The pseudo scalar seismic moments are analogues to earthquake stress drop rather than moment magnitude (Angus et al., 2010; McGuire & Kaneko, 2018).

5.4 Results

Integrated THM modelling and microseismic modelling was applied to a LHS of the input factor ranges described in Table 5.1. Of the 1000 sampled scenarios, 910 model runs predicted microseismicity during excavation and 155 model runs additionally predicted microseismicity after waste emplacement and backfilling.

5.4.1 Stress plotting

Figure 5.6 shows the stress paths and locations for the microseismic events that were predicted after backfilling in a model (576 m depth, 5.6% over-pressure, 0.93 horizontal stress factor, 1.2 % tunnel support pressure, 0.3 MPa backfill emplacement pressure and up to 0.5 MPa backfill swelling pressure). As hypothesised in Figure 5.1, the excavation increases the differential stress and the heating decreases the mean effective stress causing yielding in shear. This is seen in all of the events predicted after waste emplacement and backfilling in the 155 model runs.

Stress path and yield surface plotting in Figure 5.6 shows that the differential stress, mean effective stress and yield surfaces decrease towards the tunnel before

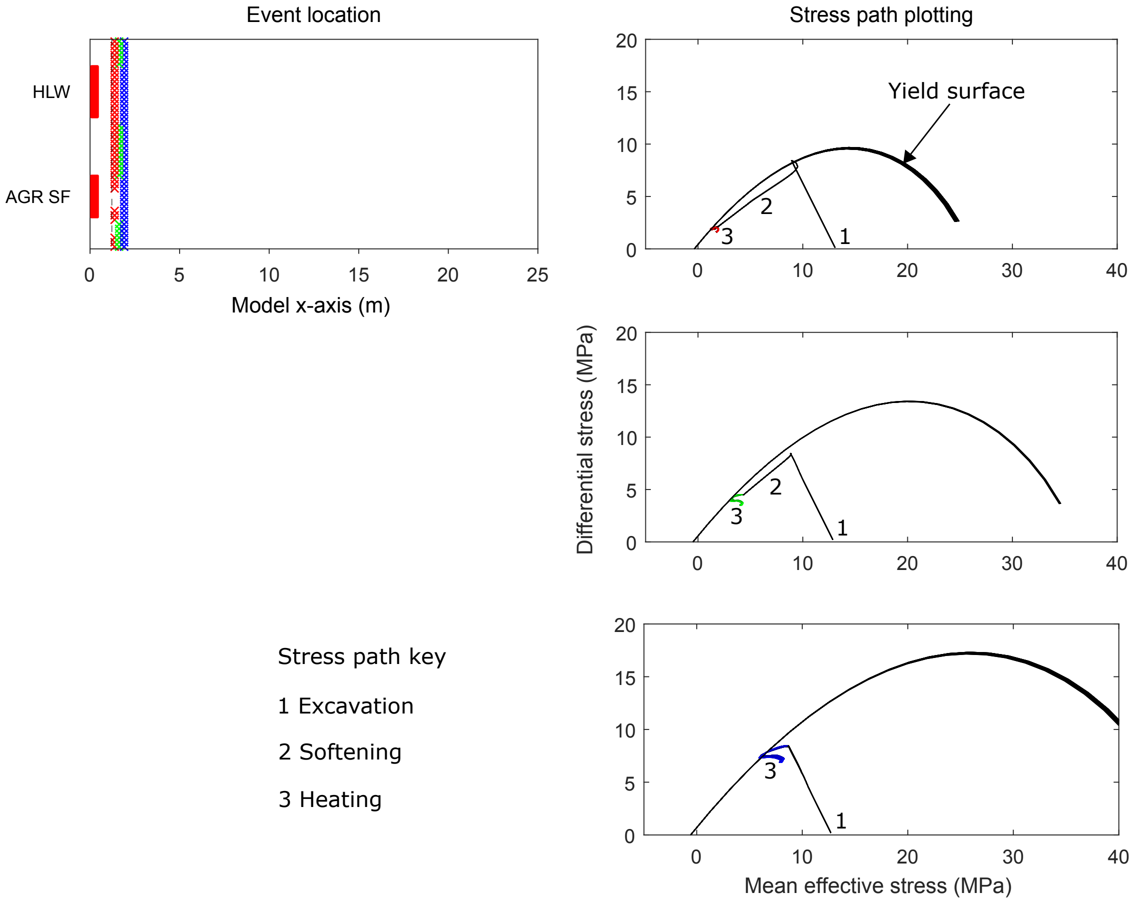

Figure 5.6: Event locations and stress path plotting for microseismic events that occured during heating from a representative model. The events are grouped into three radial distances fixed by the structured mesh. The stress path plotting is separated into those three groups and the radial distance is indicated by the colour. The colour also highlights the stress path from the moment of backfill and during heating, i.e. the black stress paths show the excavation perturbation as indicated by the number labels. Black arcs show the yield envelopes and appear thick because yield envelopes for all of the elements that yield at that radial distance are overlain. Yield events occur as hypothesised in Figure 5.1.

backfilling. The stress path relaxes roughly parallel to the yield surface. This is softening caused by yielding in shear during the excavation.

The microseismic events spatial locations are proximal to the tunnel, up to 0.75 m radial distance, and along the entire simulated length (Figure 5.6). The decrease in mean effective stress during heating is greater further from the excavation over the radial distance of the predicted microseismic events (Figure 5.6). This is because the preceding ventilation reduced the pore pressure towards the excavation. The effect of the preceding ventilation on the pore pressure during heating is illustrated in the pore pressure transect after 2 years (Figure 5.7). The pore pressure variation parallel to the long axis of the tunnel is low and unlikely to affect the microseismicity.

The stress paths during heating (coloured lines in Figure 5.6) translate horizontally rightwards after yield events (contact with the yield surface). This indicates an increase in mean effective stress which is caused by a decrease in pore pressure as a response to dilational yielding. The decrease in pore pressure is curtailed by the continued heating indicated by the curling ends to the stress paths (Figure 5.6).

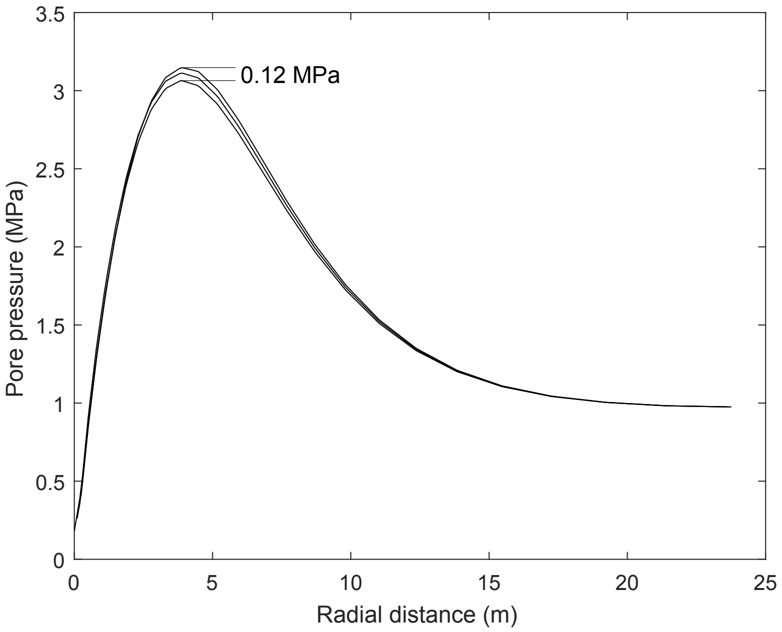

Figure 5.7: Three radial transects of pore pressure 2 years after waste emplacement and backfilling. The tunnel wall is at 0 m. The pore pressure peak is not at the tunnel wall because the pore pressure adjacent to the tunnel was reduced by preceding ventilation. The transects are perpendicular to the centre of the HLW canister, centre of the HLW and AGR SF canisters and centre of the AGR spent fuel canister. The pore pressure peak variation parallel to the long axis of the tunnel is 0.12 MPa.

5.4.2 Input factor mapping for microseismicity

Input factor mapping is describing the input factor combinations that meet a particular criteria. Figure 5.8 summarises the input factor mapping for the criteria of 'no microseismicity', which separates the models into a group that predicted no microseismicity at any stage. All scenarios with a normalized sample value of greater than 0.2411 for depth have microseismicity. The depth range is 200 to 1000 m, therefore, the maximum depth at which no microseismicity was predicted was 393 m. The absence of tunnel support results in microseismicity for all depths.

Figure 5.9 illustrates input factor mapping for the criteria of microseismicity after backfilling. The criteria separates the models into a group that predicted microseismicity during the backfill and heating stage. Microseismicity constrains the minimum depth and maximum backfill swelling pressure. However, microseismicity does not map onto an exclusive region of the depth against backfill swelling pressure

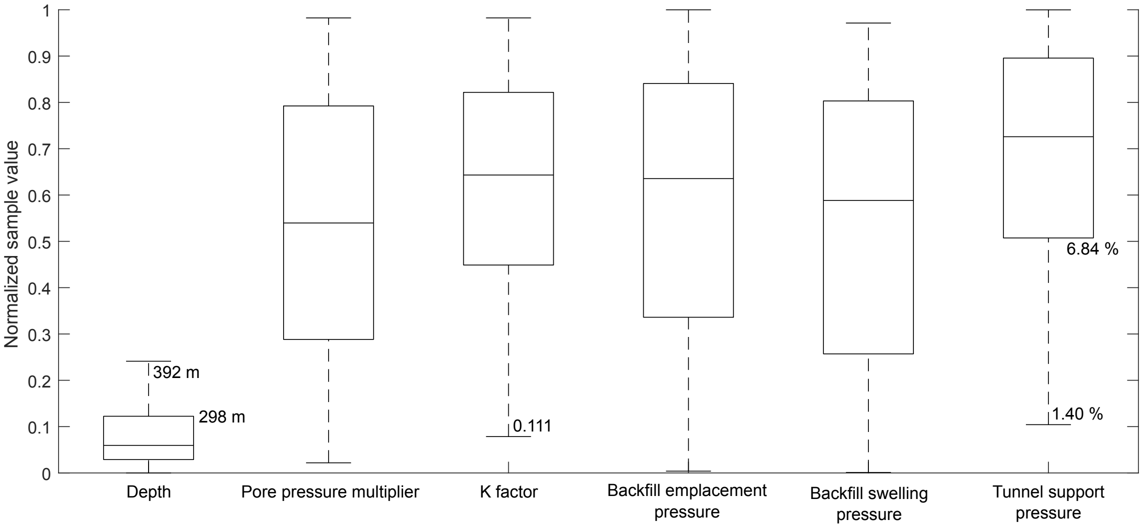

Figure 5.8: Input factor mapping for the criteria of no microseismicity. The criteria is used to separate the models into a group that predicted no microseismicity and a group that did. The input factors of the models in the group that predicted no microseismicity are normalized and presented as box plots. The line inside each box is the median; the tops and bottoms of each box are the 25th and 75th percentile, and the distance between them is the interquartile range; and the whiskers extend to the furthest observations. The box plots show that no microseismicity is predicted by models with shallow depths and greater tunnel support pressure.

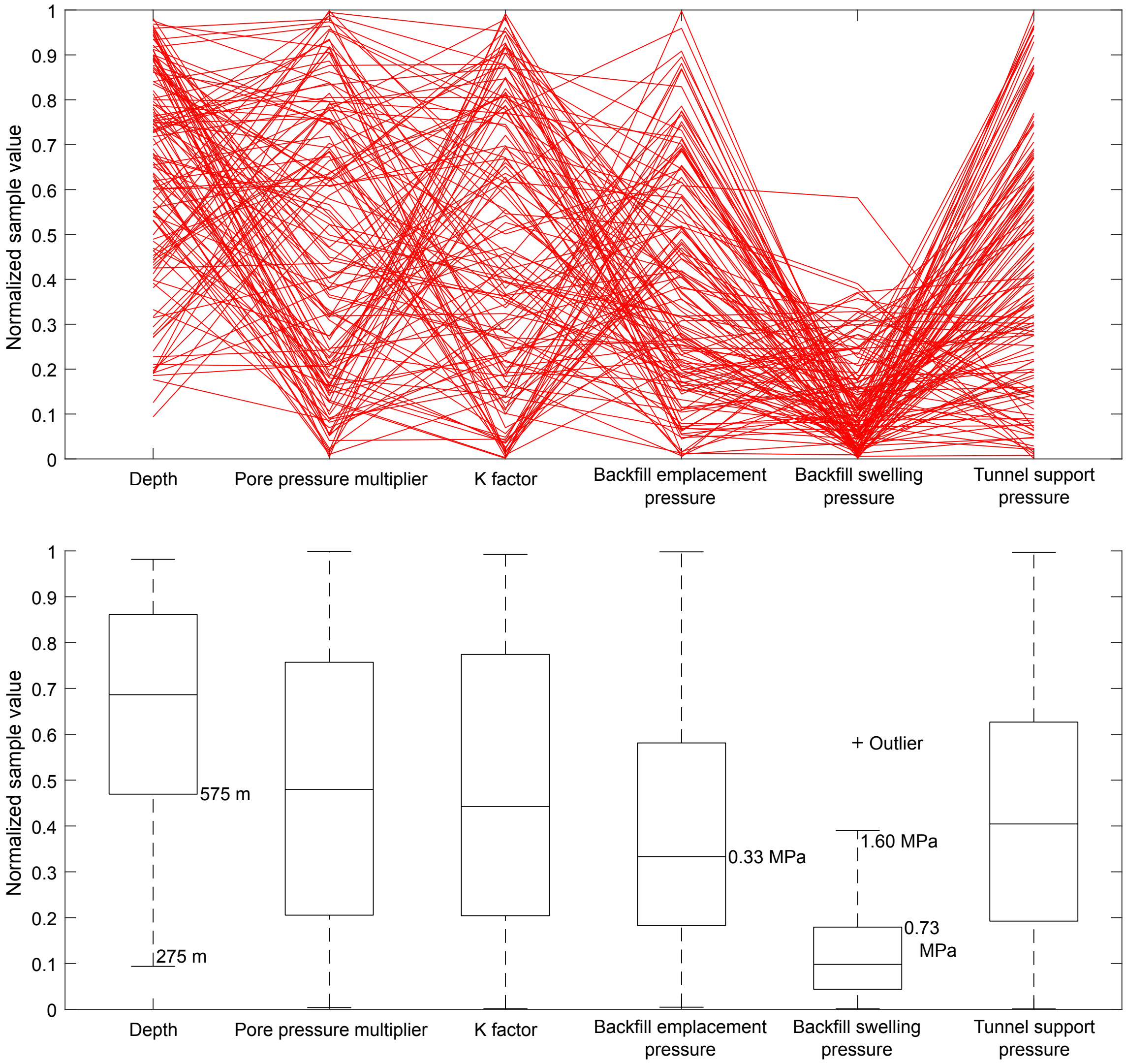

Figure 5.9: Input factor mapping for the criteria of microseismicity after backfilling. Red lines illustrate the normalized input factor values of each sample that predicts microseismicity after backfilling. Box plots are illustrated for a statistical summary and are defined in Figure 5.8. However, a backfill swelling pressure whisker does not include an outlier which is defined as greater than 1.6 times the interquartile range. Microseismicity is predicted in model runs with greater depths and lesser outward pressure from the engineered aspects on the tunnel wall.

(Figure 5.10).

The backfill swelling pressure has the lowest range and interquartile range (Figure 5.9) indicating that it may be the best input factor to constrain using microseismic

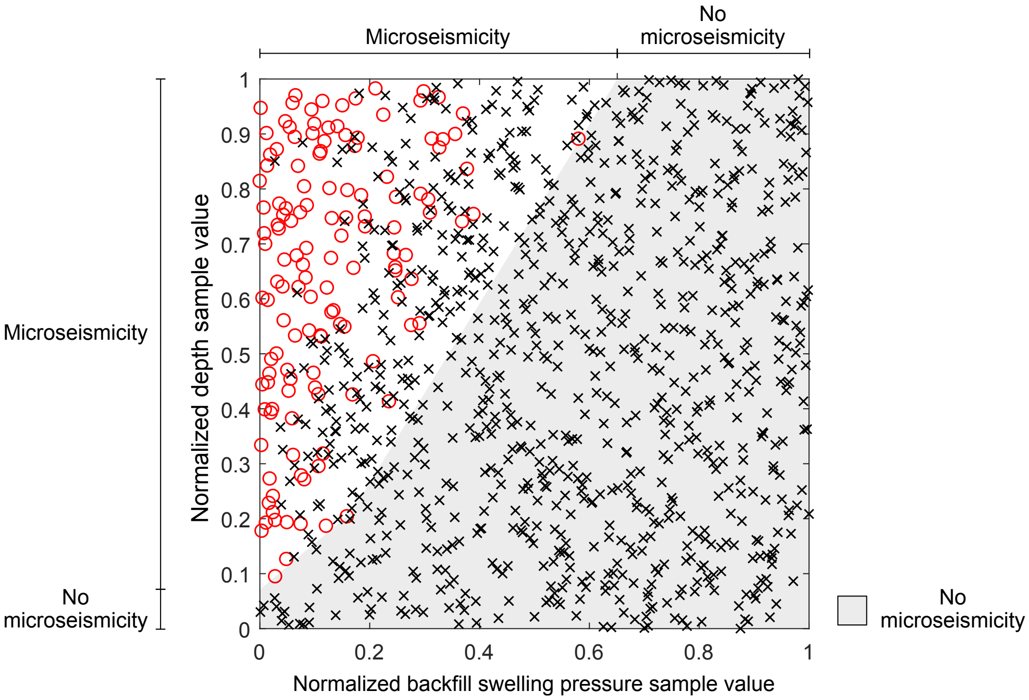

Figure 5.10: The normalized sample value for backfill swelling pressure against depth. A black cross indicates no microseismicity and a red circle indicates microseismicity after waste emplacement. The data do not form exclusive regions. Therefore, it would not be accurate to predict the occurrence of microseismicity knowing only the depth and backfill swelling pressure.

data. This is an important finding because the backfill swelling pressure will be the most uncertain input factor, investigated here, once the facility has been built.

The scenario of 'no microseismicity' may constrain the minimum backfill swelling pressure which may indicate the engineered barrier is behaving as expected. Contrarily, microseismicity may constrain the maximum backfill swelling pressure which may indicate the engineered barrier is not behaving as expected. Crucially, the microseismic event types, magnitudes and locations could contain information to help understand why.

5.4.3 Microseismic monitoring insights

If microseismic events are recorded after waste emplacement, what insights might the event data contain?

Figure 5.11 contains a histogram for each of the data contained in the microseismic event predictions from the modelling. The time histogram is bimodal, with a tight (single bin) mode in the first year after waste emplacement and a second mode with the median at six years after waste emplacement (32 years). The second mode is skewed with a steep decline in events at nine years after waste emplacement. Figure 5.12 shows that the peak pore pressure is reached in the first year after emplacement which is also the year with the most microseismic events. Figure 5.12 shows the mean effective stress and pore pressure in the rock nearest to the tunnel, the peak pore pressure and minimum mean effective stress are delayed with increasing radial distance.

In Figure 5.11, the pseudo scalar seismic moment histogram is skewed towards larger events with the median at 4.5 MPa. The radial distance histogram distribution is scattered across five distinct bins because the spatial location of events is constrained by the model mesh elements. The highest frequency is adjacent to the tunnel wall and the frequency declines steeply over the radial distance. The longit-

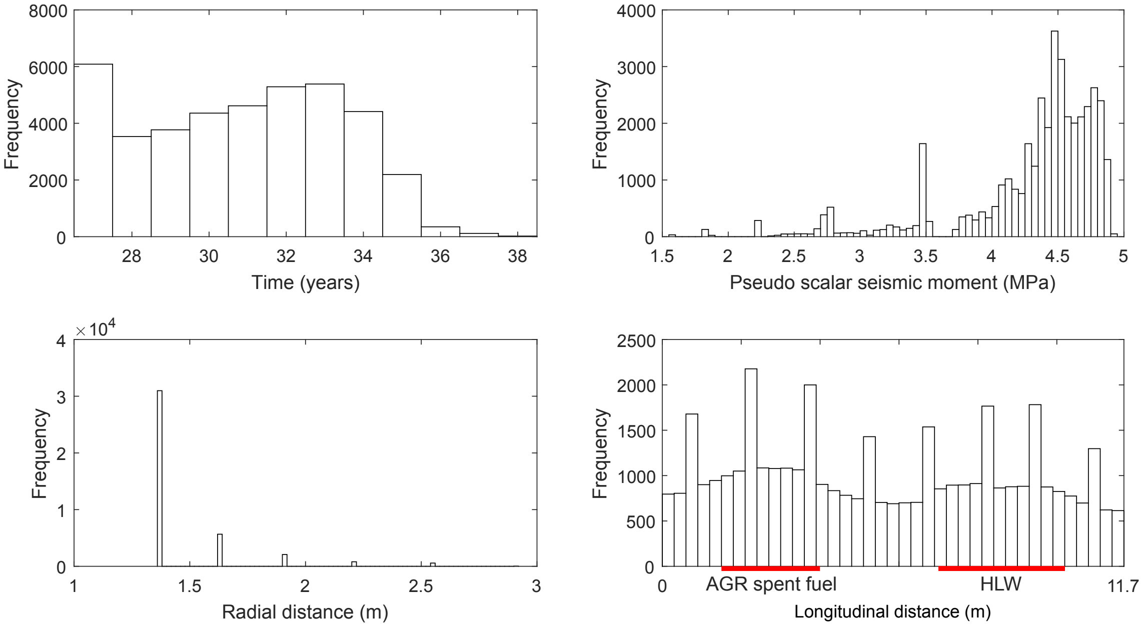

Figure 5.11: Histograms for all of the events that occur in the sensitivity analysis after waste emplacement. The five distinct bins with events for radial distance are the centre of mesh elements. The waste canisters are illustrated for the y-axis, rather than the longitudinal distance values, because they explain the bimodal distribution.

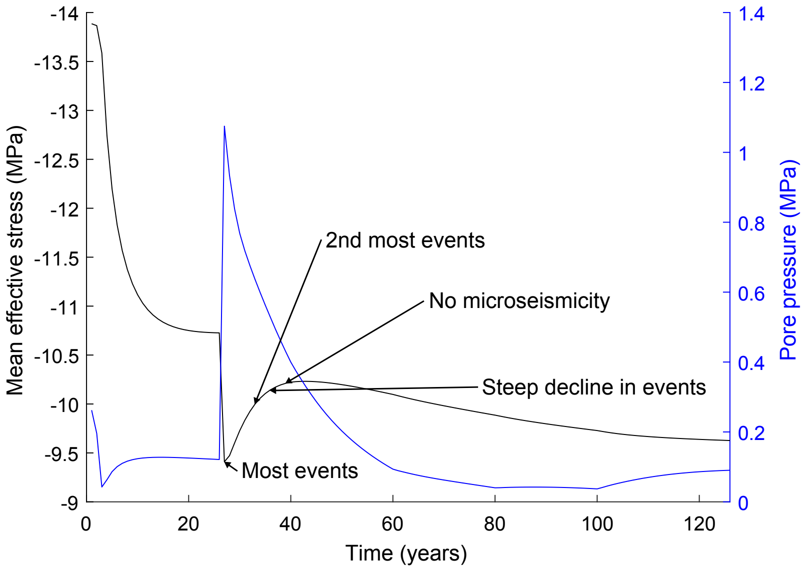

Figure 5.12: Mean effective stress (black) and pore pressure (blue) against time at a point in the centre of the waste canisters and 0.125 m radial distance from the tunnel, for a model with post-emplacement microseismicity (576 m depth, 5.6% over-pressure, 0.93 horizontal stress factor, 1.2 % tunnel support pressure, 0.3 MPa backfill emplacement pressure and up to 0.5 MPa backfill swelling pressure).

udinal distance histogram is bimodal with modes centred about the waste canisters. Longitudinal distance refers to the distance parallel to the long axis of the tunnel. The distribution spans the entire tunnel section. 50.73 % of events occur in the AGR spent fuel canister side of the tunnel section and 49.27 % of events occur in the HLW canister side of the tunnel section, indicating that the waste type causes a similar number of events. There are more events in the space between AGR spent fuel canisters than between HLW canisters. The waste type can be distinguished by the AGR spent fuel having a tighter distribution reflecting its shorter canister length.

Categorizing the events according to the nearest waste canister and plotting the same histograms (Figure 5.13a) shows little change. The AGR spent fuel canister is skewed towards earlier events and further radial distances. This is because the AGR spent fuel has a higher initial internal heat generation (Figure 5.4).

Categorizing the events according to the radial distance (Figure 5.13b) shows that an events time and pseudo scalar seismic moment are strongly related to its

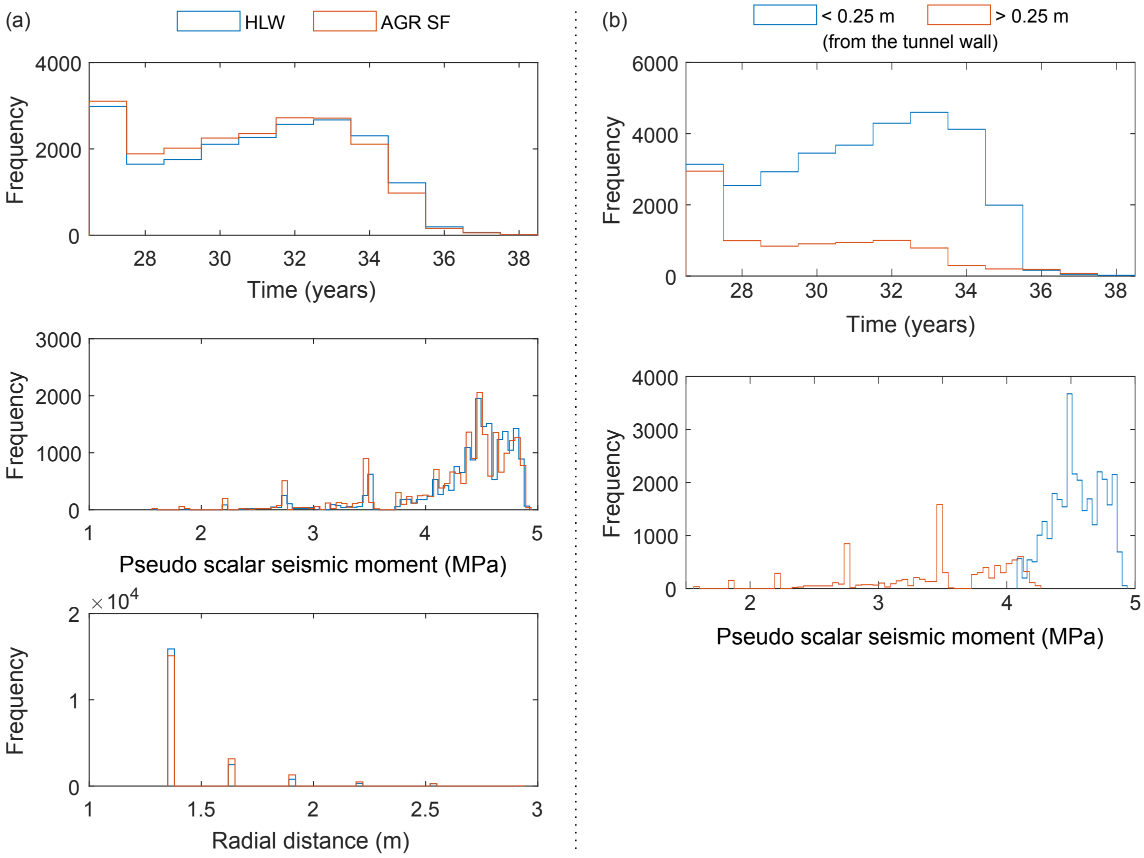

Figure 5.13: Histograms for all of the events that occur in the sensitivity analysis after waste emplacement. (a) Events grouped by the nearest waste canister. The similarity of distributions indicates that the waste canister type does not affect the microseismic event time, pseudo scalar seismic moment or radial distance. (b) Events grouped by the radial distance. Less than 0.25 m represents events occurring in the mesh elements adjacent to the tunnel wall.

radial distance. The events that are adjacent to the tunnel wall have higher pseudo scalar seismic moments and a wider probable distribution through time. The shear events adjacent to the tunnel wall display a tight pseudo scalar seismic moment distribution varying over 1 MPa. Figure 5.14 confirms that relatively high pseudo scalar seismic moment events are distributed through time whereas relatively low pseudo scalar seismic moment events are skewed towards the initial year.

The pseudo scalar seismic moment distributions for the events categorized according to the radial distance are almost exclusive, with the exception of 4.08 MPa

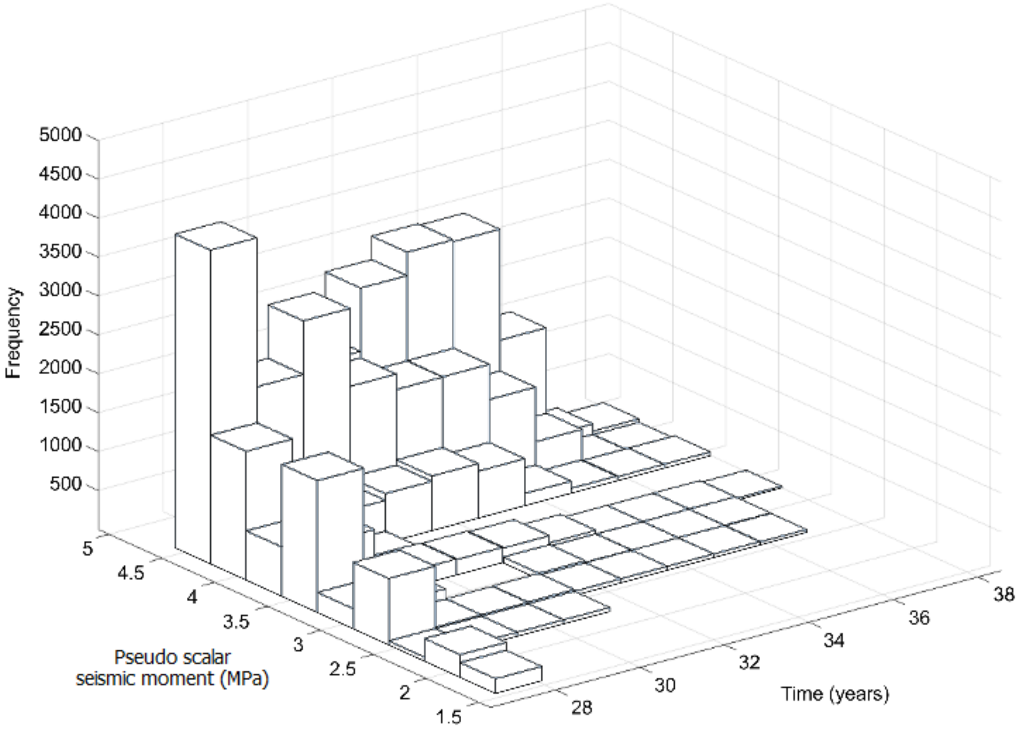

Figure 5.14: 2D histogram of time and pseudo scalar seismic moment for all of the events that occur in the sensitivity analysis after waste emplacement.

to 4.23 MPa (Figure 5.13b). Therefore, the event time and pseudo scalar seismic moment can be used to predict whether the events have a radial distance less than or greater than 0.25 m from the tunnel wall. A random forest algorithm was trained on 70 % of the events to predict whether the event was within 0.25 m of the tunnel wall using its time and pseudo scalar seismic moment. The algorithm successfully predicted the remaining 30 % of the events with no errors.

Backfill swelling pressure

A multi-method sensitivity analysis (Petropoulos & Srivastava, 2016) was run with the microseismic event times, pseudo scalar seismic moments, radial distances and longitudinal distances as input factors, and the model run's backfill swelling pressure as the output factor. Figure 5.15 shows that the backfill swelling pressure is sensitive for the pseudo scalar seismic moment, radial distance and time. These analyses

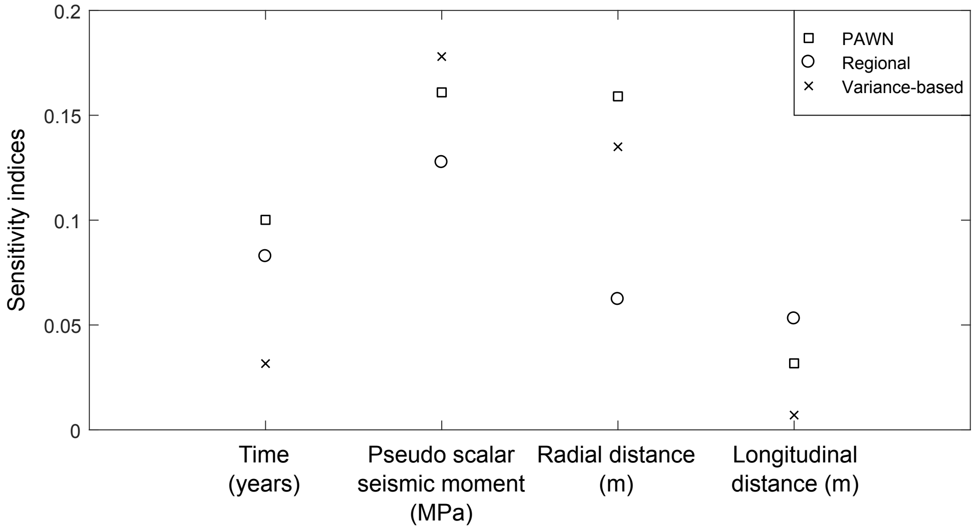

Figure 5.15: Multi-method sensitivity analysis (Petropoulos & Srivastava, 2016) for the microseismic event times, pseudo scalar seismic moments, radial distances and longitudinal distances as input factors against the model run's backfill swelling pressure as the output factor. The pseudo scalar seismic moment is the most sensitive input factor and the longitudinal distance is the least sensitive input factor.

demonstrate that the backfill swelling pressure is sensitive for data from microseismic events.

Another multi-method sensitivity analysis was run with summary statistics for the microseismic events predicted by each model run as input factors. Therefore, instead of all of the events from a model run individually contributing to the input factors as in the sensitivity analysis in Figure 5.15, in this analysis, only the minimum, maximum and mean values from the model run contribute.

The analysis provided three additional insights to the sensitivity of the backfill swelling pressure to data from microseismic events. Firstly, the backfill swelling pressure is also sensitive for the total number of microseismic events and secondly, this ranks higher than the time and radial distance (Figure 5.16). Finally, the backfill swelling pressure is not sensitive for the minimum time or minimum radial distance of the microseismic events. This is because the minimum time and minimum radial distance are the minimum possible (i.e. constant) for all model runs.

Linear regression was used to determine how the microseismic event data affects the likely backfill swelling pressure. The R-squared value for the model is 0.285

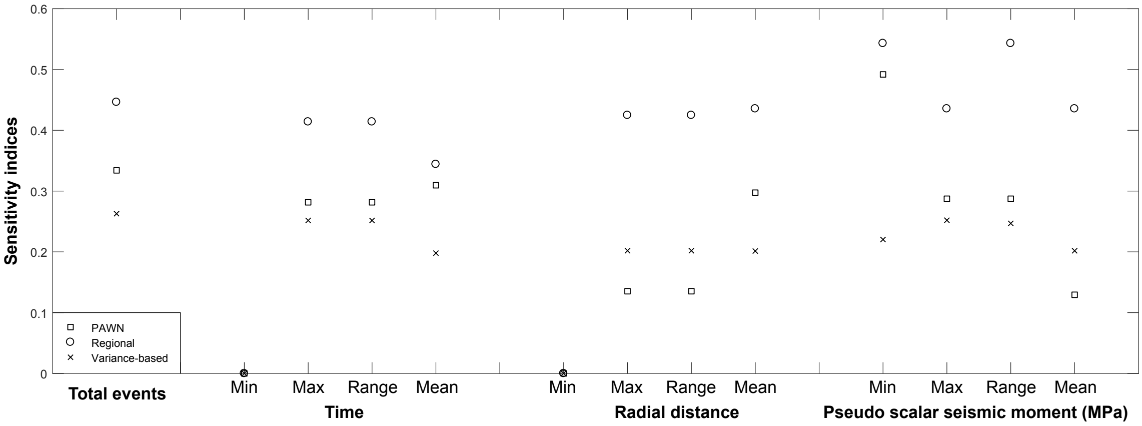

Figure 5.16: Multi-method sensitivity analysis (Petropoulos & Srivastava, 2016) for summary statistics of microseismic events in each model run against the model run's backfill swelling pressure as the output factor.

which suggests that the model explains approximately 28.5 % of the variability in the backfill swelling pressure as the response variable. The p-value is 8.08×10^{-7} which is less than the significant level of 0.05 indicating that the model is significant. This was expected because stress plotting showed that the microseismicity depends on low radial stress (Figure 5.6).

Figure 5.17a shows that increasing the total number of events decreases the likely backfill swelling pressure. The model gradient indicates that for every event recorded, the likely backfill swelling pressure decreases by 0.7 kPa. However, the R-squared value is 0.152 which suggests that the model explains only 15.2 % of the variability in the backfill swelling pressure. The residual analysis (Figure 5.17b) best fit line is $y = 0.0$ and the spread of residuals is unbiased around the horizontal line meaning that it is not a non-linear relationship. The spread of residual values decreases as the total events increases, indicating that the accuracy of the model increases with increasing microseismic events.

Figure 5.18 shows the linear regression model for the summary statistics of the model runs and their events. Increasing the maximum time, mean time, maximum radial distance, mean radial distance or maximum pseudo scalar seismic moment suggests a decrease in the likely backfill swelling pressure. Decreasing the minimum pseudo scalar seismic moment also suggests a decrease in the likely backfill swelling pressure.

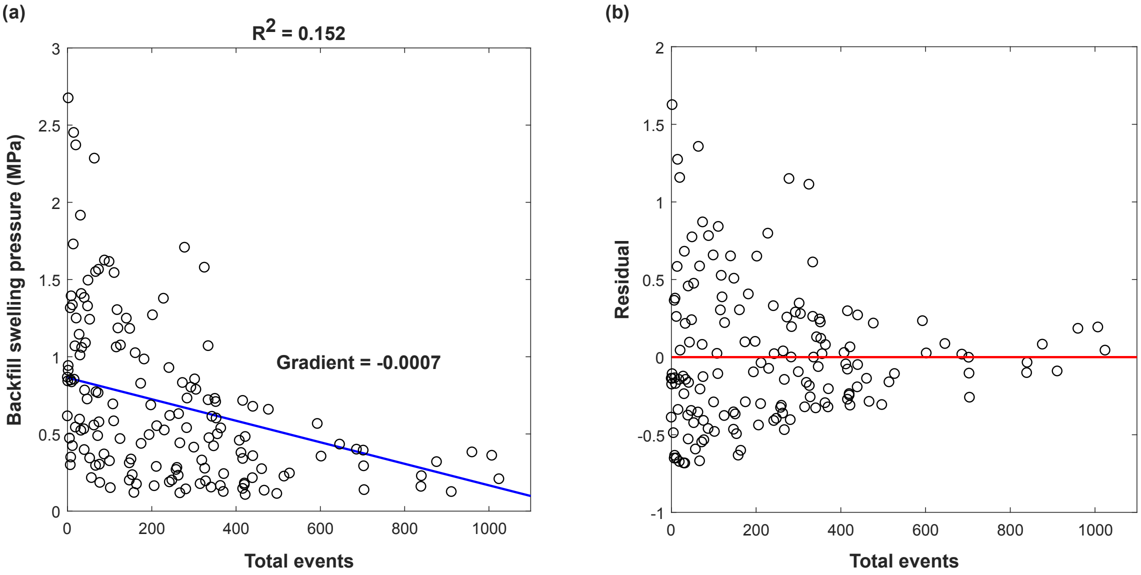

Figure 5.17: (a) Linear regression for total events against backfill swelling pressure where the predictive model is illustrated in blue. (b) Residual analysis for the regression, where the residual value is the difference between the observed value of the dependent variable and the predicted value and the line of best fit is illustrated in red.

5.5 Discussion

A THM model, similar to the validated axisymmetric heater test model in Chapter 3 and Chapter 4, was built to simulate a section of heat-producing waste tunnel with HLW and AGR spent fuel canisters. Microseismic modelling was integrated into the geomechanical modelling process. The associated moment tensor mechanisms were evaluated based on the eigen-solution of the differential stress tensor to estimate the pseudo scalar seismic moment of failure, with the assumption that failure is not aseismic (Angus et al., 2010). A range of scenarios were explored using methods introduced in Chapter 4. The explored space represents the current range of scenarios for a GDF in lower strength sedimentary rock.

Microseismicity occurred after emplacement in 13.4 % of the GDF scenarios, as the increasing pore pressure during heating reduced the effective stress. The microseismicity was mapped onto the sample space to identify depths, in situ stress, in situ pore pressure, tunnel support pressure and backfill swelling scenarios that may have microseismicity. The depth and backfill swelling pressure were constrained.

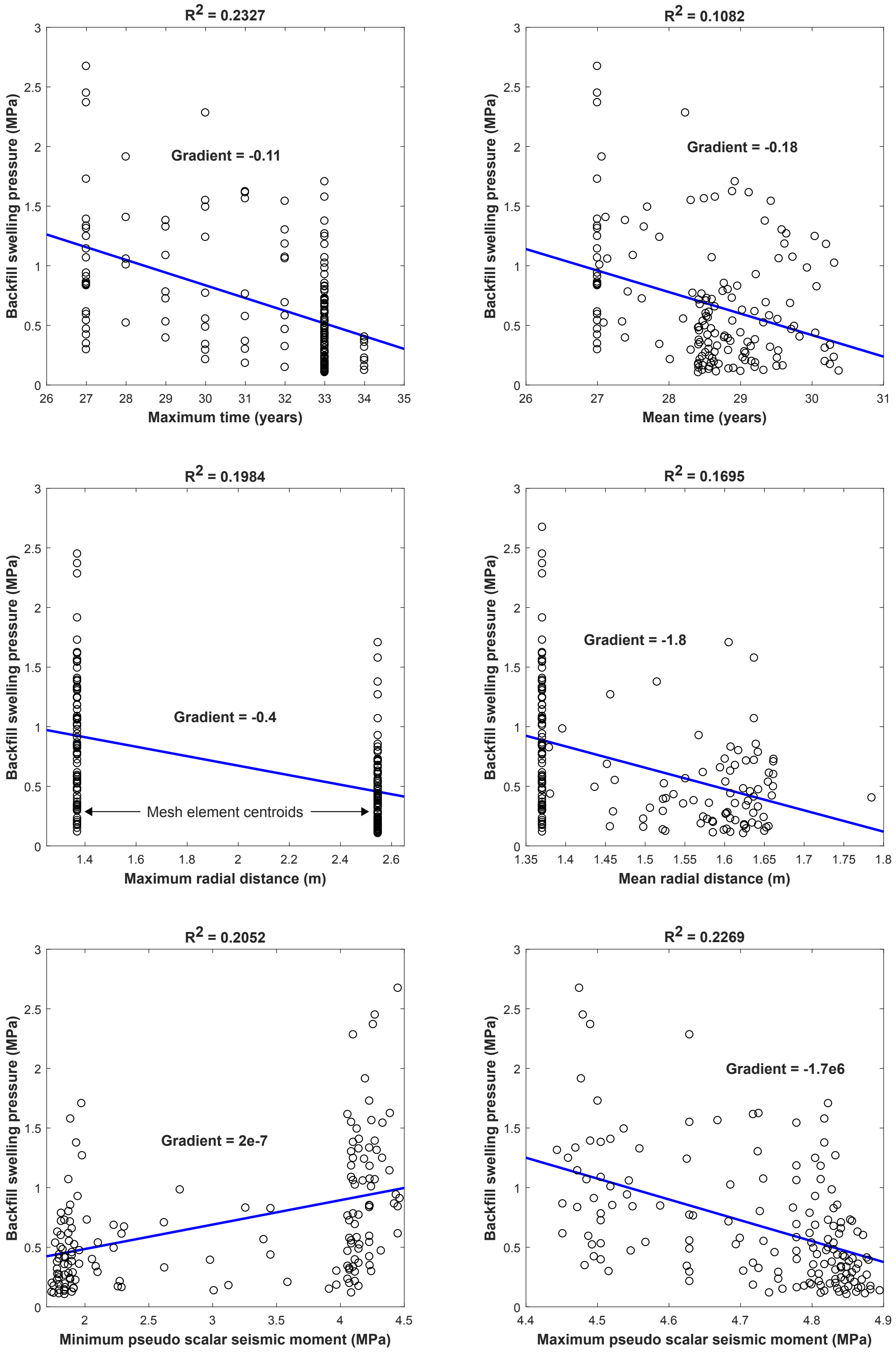

Figure 5.18: Linear regression for the response variable backfill swelling pressure. The event distributions are constrained by the model mesh elements and model output times.

The results were analysed in terms of spatial, temporal and pseudo scalar seismic moment variations in the predicted microseismic events. It was shown that the microseismic events contain data that affects the determination of likely backfill swelling pressure. Therefore, it is proposed that continued microseismic modelling after backfilling HLW and spent fuel disposal tunnels in these scenarios will provide insights into the backfill swelling pressure and pore pressure development.

It is possible to directly monitor the backfill swelling pressure at a particular location using sensors (Thomas et al., 2014). Microseismic monitoring to indirectly monitor backfill swelling pressure has three advantages. First, it is non-intrusive (Barkved, 2004), therefore, no potential pathways are created for contamination. Second, it is 3D and expansive rather than a particular location, and there will be around 80 km of HLW and spent fuel disposal tunnels (RWM, 2016a). Third, it is cheap and the technology will already be being used to monitor possible rock bursts (Zhao et al., 2018a).

The modelling does not capture the effects of anisotropy. In reality, discontinuities will make microseismicity more likely. Microseismicity, if any, should be expected to occur with an anisotropic distribution that is preferentially along bedding. This would be observed as similar to the distribution of microseismicity associated with shear-induced failure around excavations in Opalinus Clay (Gonidec et al., 2014). The isotropic assumption is justified by the need for 1000's model evaluations for the sensitivity analysis (Section 5.4.3). The proposed insights provided by microseismicity regarding the backfill swelling pressure are not effected by the isotropic assumption but they may be effected by faults. Increased microseismicity might be expected around known faults (Angus et al., 2010), therefore, increased microseismicity would not neccessarily indicate low backfill swelling pressure. Case specific modelling or sensors could be used in these locations.

Chapter 6

Discussion

6.1 Introduction

This section discusses the work presented in Chapters 3, 4, and 5, particularly how the research objectives presented in Chapter 2 are met and potential applications of the work. Different case studies and approaches are discussed.

6.2 Thermo-hydro-mechanical modelling for GDFs

The first stage of any modelling is conceptualization. GDF designs are host rock specific and categorized as higher strength rocks, lower strength sedimentary rocks and evaporites (RWM, 2016b). The key coupled THM processes expected in the host rocks are different and require different modelling approaches (Latha & Garaga, 2012; Joulin et al., 2017; Salimzadeh et al., 2017). The first objective was to determine a good representation of reality for heat-producing waste in lower strength sedimentary rock. The method for achieving this objective was to benchmark a THM model with experimental data from an in situ heater test that is an analogue for heat-producing waste in lower strength sedimentary rock. In situ URL experiments operate at a similar scale to radioactive waste disposal plans, therefore, there is no requirement for upscaling from micro- or sample scale (Plötze et al. 2007).

There are four major URLs devoted to clay repository research: Mol (Belgium), Mont Terri (Switzerland), Bure and Tournemire (France). The host rock at Mol is Boom Clay which is a young (30 Ma), high porosity (0.39) and weak (2 MPa uniaxial compressive strength normal to bedding), plastic clay (Li et al., 2018). The other host rocks are Opalinus Clay, Callovo-Oxfordian argillite and Toarcian argillite which are older (155–185 Ma), lower porosity (0.07–0.18) and stronger (15–32 MPa uniaxial compressive strength normal to bedding) indurated clays. RWM (2016c) has identified the latter group as target analogues for lower strength sedimentary host rocks in the UK.

Large scale heating tests at URLs simulate repository-induced THM coupled effects on the host rock at the correct scale and in situ (i.e. undisturbed). The HE-D experiment in Opalinus Clay (Wileveau & Rothfuchs, 2003; Wileveau, 2005) and TER experiment in Callovo-Oxfordian argillite (Garitte et al., 2010) aimed to understand thermal diffusion of heat flux, thermal consolidation and strain reaction in the lower strength sedimentary host rocks. The test sites were in the saturated zone away from drift to avoid hydraulic and mechanical disturbance (Wileveau, 2005). Both confirmed the THM coupled processes in lower strength sedimentary rocks.

The HE-D experiment in Opalinus Clay at the Mont Terri Rock Laboratory (Wileveau, 2005; Garitte et al., 2017) was used for the benchmark test (Section 3.3). Figure 6.1 shows representative temperature and pore pressure curves for the HE-D experiment.

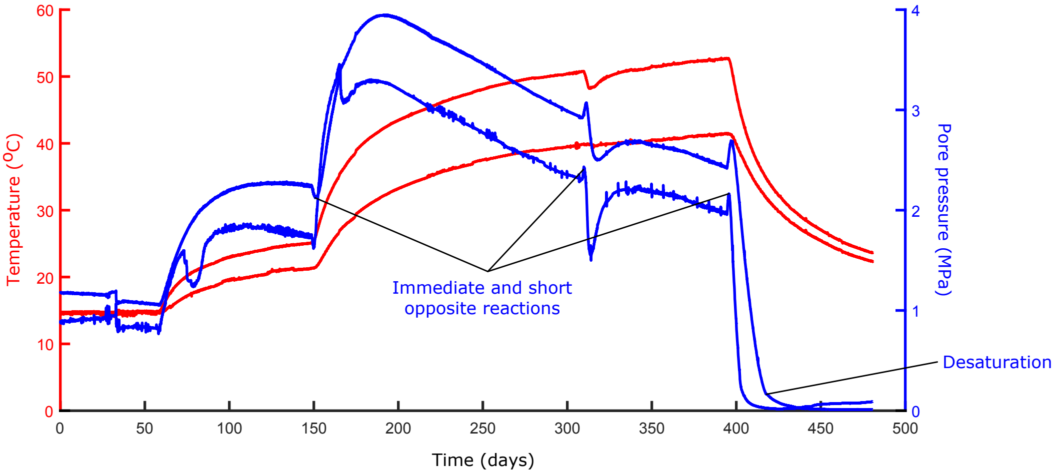

Figure 6.1: Representative temperature (red) and pore pressure (blue) curves for the HE-D experiment. The temperature behaviour is discussed in Section 6.2.1 and the pore pressure behaviour is discussed in Section 6.2.2.

Predicting accurate experimental result magnitudes depends on input parameter values, conceptualizations and mesh discretization (Figure 3.8). Better representation of the heat source (Garitte et al., 2017) and mesh refinement improved the predictions. Anisotropic properties improve predictions at some sensor locations which depends on the radial relationship between the sensor location and bedding orientation.

Plasticity and damage may decrease stiffness and increase porosity and permeability (Hoxha et al., 2006). However, limited fracturing was observed in cores taken 20 cm distance from the heaters after dismantling the HE-D experiment (Wileveau & Rothfuchs, 2006). No plasticity was observed in the benchmark test.

6.2.1 Benchmark test temperature behaviour

The temperature is accurately predicted by conduction, which has been found in previous benchmark tests using the HE-D experiment (Gens et al., 2007; Zhang et al., 2007a) and other in situ heating tests (Rutqvist & Tsang, 2004). The behaviour is characterized by increasing temperature with a decreasing gradient (Figure 3.17). The curvature and maximum temperature increase with proximity of the sensors towards the heaters. Similarly, the cooling behaviour is decreasing temperature with a decreasing gradient, where the curvature increases with proximity of the sensors towards the heaters.

Fourier's law for conduction states that the rate of heat transfer is proportional to the negative temperature gradient and the area normal to the gradient through which the heat flows (Carslaw & Jaeger, 1959). The differential form for local heat flux, q_f, is given by Equation 6.1. Fourier's law is incorporated into ELFEN as discussed in Section 3.2.1.

$$q = -\kappa \nabla T \tag{6.1}$$

where κ is thermal conductivity and ∇T is the temperature gradient (Rockfield Software Limited, 2013b). The heater test case may be approximated as a continuous line source, where the line is parallel to the y-axis and through the point (x',z'). For a continuous and constant line source, heat is liberated at the rate $\rho c q$ per unit time per unit length of the line, where ρ is density and c is specific heat capacity.

For a radial distance, r, in the system, the temperature increase, ∇T, is given by Equation 6.2.

$$\nabla T = \frac{q}{4\pi\kappa} Ei\left(- \frac{r^2}{4\kappa\nabla t} \right) \tag{6.2}$$

where $r^2 = (x - x')^2 + (z - z')^2$ and Ei is the energy transferred to the system in the steps from the reference state to the given state (Carslaw & Jaeger, 1959). The energy from a continuous line source disperses cylindrically at half the inverse square law (Figure 6.2).

With this approximation, the temperature behaviour is controlled by the material properties (thermal conductivity, specific heat capacity and density; Table 4.1), temperature gradient and radial distance. However, the thermal conductivity of Opalinus Clay is transversely isotropic (Mugler et al., 2006) which is representative of lower strength sedimentary rocks. Furthermore, the heaters have finite lengths and spacing purposefully engineered to disrupt an otherwise continuous line source to limit the maximum temperatures (RWM, 2016a).

Transversely isotropic materials can be simulated with a 2D, plane strain cross-section perpendicular to bedding or a 3D model (Figure 3.7). The heaters finite

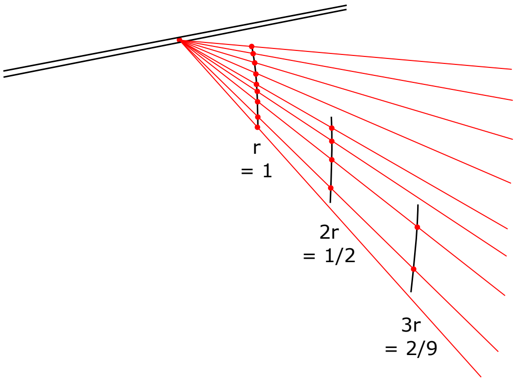

Figure 6.2: Cylindrical radiation from a continuous line source, where r is a radial distance from the line source and red lines represent the flux. The total number of flux lines is constant. The density of flux lines is inversely proportional to half the square of the distance from the source. This is half the inverse square law (which describes radiation from a point source) because the surface area of a cylinder increases with the square of the radius at half the rate of the surface area of a sphere.

lengths and spacing can be simulated with a 2D, axisymmetric cross-section parallel to the longitudinal axis of the heaters which is parallel to bedding or a 3D model. Note that r is given by the equation for radial distance which is used to map the sensors 3D locations onto axisymmetric space. An axisymmetric model is appropriate for cylindrical dispersion and circular cross-sectional tunnels. An efficient, 2D model was required for this work, therefore, the axisymmetric model was used. This is in line with other 2D simulations of in situ heater tests (Zhang et al., 2007a; Garitte et al., 2017). The effect of transverse isotropy is discussed later in Section 6.2.4.

In summary, the temperature is accurately predicted by conduction. As the system progresses the rock is heated reducing the temperature gradient, therefore, reducing the heat flux and causing a decreasing temperature gradient over time. Furthermore, since the temperature gradient is highest nearest the heaters, the curvature is highest nearest the heaters.

6.2.2 Benchmark test pore pressure behaviour

The pore pressure behaviour is similar to the temperature that drives it. However, the curvatures are greater with sharper initial reactions and reversals to decreasing pore pressure whilst the temperature continues to increase (Figure 3.18). There are two additional phenomena: an immediate and short opposite reaction to changes to the heater output, and a reduction during cooling below the initial pore pressure.

An increase in temperature causes thermal expansion of the solid and fluid. The solid expansion is constrained by in situ stress causing thermal stress. The fluid expansion is constrained by the solid causing increased pore pressure, which is amplified by the differential thermal expansion of fluid and solid (Delage et al., 2000). Darcy's law states that fluid flows towards lower pressures and with a greater rate for greater pressure gradients. The fluid flux, q_f, is calculated in Equation 6.3.

$$q = -\frac{k}{\mu}\nabla p_f \tag{6.3}$$

where k is absolute permeability, μ is viscosity and ∇p_f is the pore pressure gradient (Rockfield Software Limited, 2013b). Therefore, the temperature gradient causes a pore pressure gradient that triggers flow towards lower pressure. The flow dissipates the increased pore pressure and the flow rate increases with temperature because of the temperature-dependent viscosity (Hooman & Gurgenci, 2007). The main input parameter that differs amongst approaches to simulating the HE-D experiment is the fluid viscosity. This work agrees that temperature-dependent viscosity makes a significant improvement on the predicted pore pressure (Gens et al., 2007) by increasing the rate of excess pore pressure dissipation post-peak. Competition between generating and dissipating pore pressures causes the pore pressure to decrease during the test whilst the temperature is increasing continuously.

There is no significant hydraulic to thermal coupling. Advection is negligible and the bulk thermal properties are not significantly affected by fluid flow.

The pore pressure is accurately predicted by thermal consolidation, which has been found in previous benchmark tests using the HE-D experiment (Wang & Kolditz, 2013; Garitte et al., 2017) and other in situ heating tests (Rutqvist & Tsang, 2004). The models predict the measured increase in pore pressure and the subsequent drainage. The greatest difference between modelling approaches is caused by the heater borehole hydraulic boundary condition being drained or undrained. Undrained heater boreholes over-predict the maximum pore pressure and under-predict the drainage rate (Zhang et al., 2007a). Minor variations in permeability (e.g. 2.00×10^{-20} m^2 to 5.00×10^{-20} m^2) and thermal expansion (e.g. 1.0×10^{-5} K^{-1} to 2.6×10^{-5} K^{-1}) used in published models do not cause significant differences in the pore pressure behaviour (Garitte et al., 2017).

Desaturation

Darcy's law is analogous to Fourier's law. The fluid flux is dependent on the pore pressure gradient similar to the heat flux being dependent on the temperature gradient. However, unlike heat flux, fluid flux with a finite source is a mass transfer mechanism. During cooling the temperature decreases towards the initial value and the fluid contracts. The pore pressure decreases below the initial value (Figure 6.1) because fluid has flowed away from the heaters when the pore pressures were raised. Increased pore pressure and drainage during the heating phase was observed in this work and by all other published simulations of the HE-D experiment (Wang & Kolditz, 2013; Garitte et al., 2017).

Further work simulating THM processes for heat-producing waste in lower strength sedimentary rocks should consider the effects of partial saturation, matric suction and relative permeability (Romero et al., 1999; Ravichandran, 2009) to accurately predict resaturation (Cleall et al., 2006). The effects are stronger in heater tests because the heat source is stopped instantly, whereas heat-producing radioactive waste output decays (Bond & Watson, 2012) supporting a slower return to the initial temperature.

6.2.3 Benchmark test displacement behaviour

Adjacent to the heater, heating causes thermal expansion of the rock. The volume of rock undergoing thermal expansion increases as the heat is conducted. The rock beyond significant increases in temperature is subject to radial compression away from the heaters and circumferential expansion as a reaction to the expansion of the contained rock.

The displacement trends are accurately predicted by thermal poroelasticity, which has been found in previous benchmark tests using the HE-D experiment (Wang & Kolditz, 2013). However, the predicted rock expansion magnitude varies between published models by a factor of four (Garitte et al., 2017), despite the models using the same value for the thermal expansion of the solid skeleton.

The sensitivity analysis finds that uncertainty in the displacement is influenced more by the pore pressure input factors than the thermal expansion of the solid skeleton. In reservoir production, decreasing pore pressure increases mean effective stress causing reservoir compaction (Nagel, 2001). Reservoir compaction reduces mean effective stress in the overburden which resultantly expands (Herwanger & Koutsabeloulis, 2011). Therefore, rock expansion caused by increasing pore pressures should be considered a major control for displacement in heater tests and radioactive waste disposal.

6.2.4 Isotropic and anisotropic representations

Lower strength sedimentary rocks with high clay contents have transversely isotropic properties related to the depositional conditions of the sediments and the foliated nature of clays (Baud et al., 2005). Permeability is low and the anisotropy is high, generally an order of magnitude higher parallel to bedding than perpendicular to bedding (Hantschel & Kauerauf, 2009). Anisotropic permeability decreases with increasing water content (Zhang & Rothfuchs, 2004).

Opalinus Clay thermal conductivity is 2.1 W/m.K normal to bedding and 1.0 W/m.K parallel to bedding (Mugler et al., 2006) and permeability is $2.00 \times 10^{-19}\ m^2$ normal to bedding and $5.00 \times 10^{-20}\ m^2$ parallel to bedding (Marschall et al., 2005). Therefore, two locations at identical radial distances but different angles observe different temperatures and pore pressures. This has been simulated in benchmark tests and shows distinctive elliptical contours with the major axis oriented parallel to bedding (Garitte et al., 2017).

The effects of the anisotropy of the Opalinus Clay on the thermal diffusion in the HE-D experiment can be seen by interpolating the sensor data onto an axisymmetric space (Figure 6.3). There is a trend for higher diffusion perpendicular to the heater furthest from the niche. Analysed alongside the sensor layout, this is interpreted as being because the sensors perpendicular to the heater nearest the niche are oriented parallel to the Opalinus Clay bedding.

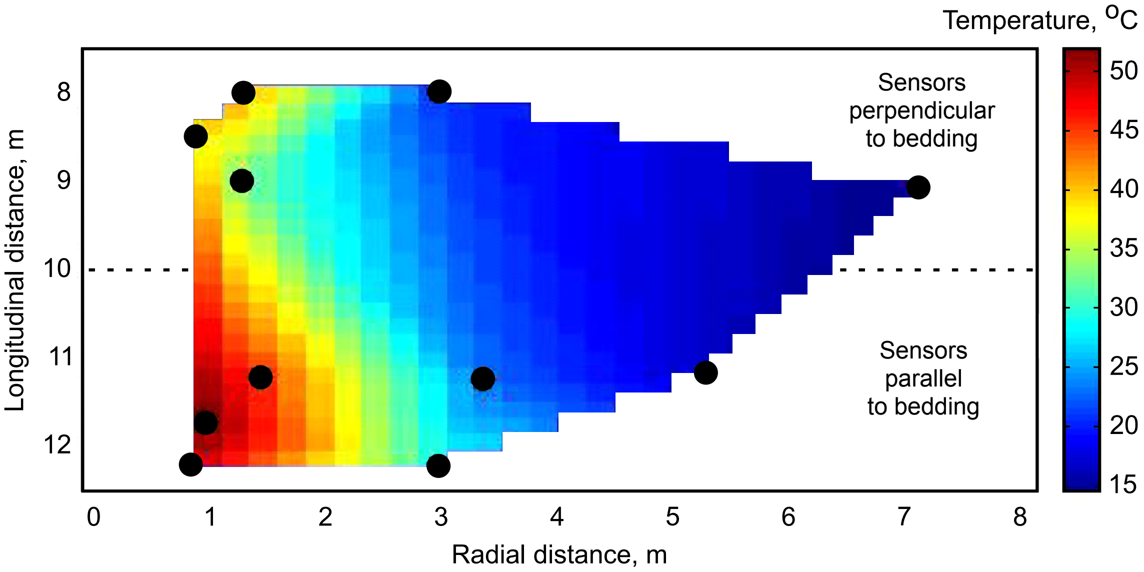

Figure 6.3: HE-D temperature data interpolated onto an axisymmetric space. Black circles represent sensor locations in axisymmetric space. The sensors can be grouped into roughly perpendicular to bedding or parallel to bedding in relation to the heaters.

The axisymmetric, isotropic assumption is required for the global sensitivity analysis. The assumption is valid because the THM processes and observable trends are predicted and the magnitudes are predicted accurately for some sensors. Furthermore, the disparity at other sensors is well understood (Figure 6.3). The sensitivity of thermal conductivity and permeability is still determined in the analysis. However, the sensitivity of the anisotropic ratio is not.

6.3 Global sensitivity analysis

A global sensitivity analysis was performed on the benchmarked model to meet three complimentary objectives. First, to demonstrate computationally expensive, global sensitivity analysis methods for computationally expensive, THM, FEM models. Second, for input factor screening and convergence analysis. Third, for input factor ranking to determine which rock properties are most sensitive for heat-producing radioactive waste.

When implementing the results, it should be considered that the work presented in this thesis used a specific case study and experimental set-up. The case study and experimental set-up were selected to increase the applicability of the work. The case study was an in-situ heating experiment which provides a good representation of heat-producing waste packages in rock. The host rock was Opalinus Clay which is an analogue for low permeability, lower strength sedimentary rocks. The parameter ranges are based on uncertainty ranges in the characterisation of the experiment site, which are relatively well constrained for rock masses, as would be expected at a site for radioactive waste disposal. Considering the case study, therefore, the results are applicable to modelling internal heat generation in low permeability, lower strength sedimentary rocks, up to 100 °C over a timescale of days to years.

6.3.1 Input factor screening

Sarrazin et al. (2016) demonstrate that screening converges with less model evaluations than other sensitivity analyses objectives. Therefore, the EET (Section 4.2.1) is performed first because if any parameter ranges are insensitive for all of the outputs of interest then that parameter can be removed from the later analyses for efficiency. Screening or factor fixing identifies variables that have no influence on the model output, which can be fixed to any value in their range. Screening may be used to support model calibration (Wang et al., 2013) by reducing the parameter space. For example, Vanuytrecht et al. (2014) firstly screen model input factors to inform their model calibration. Table 4.2 provides a summary of the input factor screening.

Heat transfer is controlled by conduction and advection. The Darcy fluid flux for the advection term is described by the permeability, viscosity, pore pressure gradient, fluid density and acceleration due to gravity. The parameters in the advection term are screened meaning that the temperature variance can be attributed to uncertainty in the conduction parameters.

The temperature variance is accounted for by uncertainty in three conduction parameters. Within these three parameters, only the porosity is affected by changes in the model. The porosity changes are less than 0.5 % which is negligible. Therefore, the thermal field can be one-way coupled for uncertainty analyses reducing computation time. Furthermore, in back analyses, the temperature can be calibrated first by varying only the thermal conductivity, grain heat capacity and porosity. Then the thermal conductivity and grain heat capacity can be fixed to the back calculated values to further reduce the number of uncertain parameters for the pore pressure back analysis.

Poisson's ratio, the SR3 parameters, fluid density, grain density and fluid heat capacity can be screened at all sensor locations for pore pressure uncertainty. This demonstrates that the uncertainty in these parameters is negligible and no further work should be done to characterize them. However, the thermal expansion coefficient of the fluid and viscosity were not screened for pore pressure. Therefore, the salinity of the fluid should not be assumed in future modelling.

Convergence analysis

Convergence analysis uses subsamples of increasing size to make repeat calculations of the sensitivity indices. The indices are plotted against sample size (Figure 4.6c). The variation in the indices is shown to reduce with increasing sample size, indicating that a more accurate prediction of the sensitivity indices is achieved with a larger sample size. It is important to assess for convergence (Section 4.2.5) to demonstrate that the sample size was large enough for the result to converge.

Figure 4.6c shows that convergence was achieved within a sample size of 1980 for a specific location and time for mean effective stress. Convergence is shown to have been achieved at all of the sensor locations, through time, for the mean effective stress (Figure 4.7), temperature (Figure 4.10a), pore pressure (Figure 4.11a) and displacement (Figure 4.12a). However, the exact sample size within which convergence is achieved varies. Therefore, a sample size of less than 2200 for 21 input factors cannot be recommended.

Validation of screening

Assessing convergence aims to prove that the analysis is robust, meaning that changing the sample size will not affect the result. However, it does not validate the result. Validating the screening result requires testing it by comparing the results from a sample of the original input factor space (unconditional) with a sample from the screened input factor space (conditional). The result is valid if all of the sample variability in the unconditional group is observed in the conditional group (i.e. the output of a set of influential input factors is proven or disproven to come from the same distribution as the output of all of the input factors).

An additional 1000 model runs was required for the conditional sample and the result was validated (Figure 4.8). The limitation of the validation procedure is that it determines that the screening threshold is not too high but not whether it is too low. Therefore, no influential input factors are screened, however, it is possible that non-influential input factors are not screened. If non-influential input factors are not screened, then the screening has not been fully effective.

A different validation procedure is proposed in Sarrazin et al (2016) that tests different screening thresholds by comparing conditional samples taken from the different input factor spaces provided by the screening thresholds. A valid screening threshold can then be selected a posteriori. The number of sets of conditional samples required can be decreased by ranking the input factors first, therefore, decreasing the number of degrees of freedom. The procedure would require an additional 1000 model runs multiplied by the number of degrees of freedom which is not appropriate for computationally expensive models.

6.3.2 Input factor ranking

Ranking or factor prioritization orders inputs according to their influence on the model output. Ranking may be used for dominant control analysis to enhance our understanding of the model and the system drivers (e.g. van Werkhoven et al., 2008). An enhanced understanding based on ranking may be used to prioritize efforts for uncertainty reduction (e.g. Sin et al., 2011), or to support model development (e.g. Hartmann et al., 2013). Table 4.2 provides a summary of the input factor ranking.

The most influential parameters are thermal conductivity and permeability. This was expected because they directly affect the temperature and pore pressure outputs as the transport parameters. Pore pressure increases with decreases in thermal conductivity or intrinsic permeability, which is agreeable with previous work (Ofoegbu et al., 2019).

Previous parametric studies have focused on the rock permeability and its stiffness (represented by the Young's modulus for elastic models). Parametric studies (Selvadurai & Nguyen 1996; Gens et al. 2007; Ofoegbu et al. 2019) showed that the pore pressure is higher for lower permeability and higher stiffness. However, this work shows that the initial pore pressure, Biot's coefficient, thermal expansion coefficient and porosity are all more sensitive than the grain stiffness for the pore pressure.

Hoxha et al. (2006) states that the consideration of temperature-dependent viscosity, and thermal expansion and density of the fluid can have a noticeable influence on the predicted values of pore pressure. The sensitivity analysis presented here screened density of the fluid but agrees that temperature-dependent viscosity and thermal expansion of the fluid have significant uncertainty for predicting pore pressure. Uncertainty in the viscosity is not the variation caused by expected temperature changes, but the actual uncertainty caused by composition, e.g. salinity.

The result can be used to prioritize efforts for uncertainty reduction, i.e. further characterization. Efforts should focus on the thermal conductivity to reduce temperature uncertainty. On permeability and the thermal expansion coefficients of the grain and fluid to reduce pore pressure uncertainty. And on permeability and Biot's coefficient to reduce displacement uncertainty.

The input factor ranking enhances our understanding of the dominant controls for displacement. It indicates that uncertainty of how the pore pressure affects the pore space contributes more significantly to the displacement uncertainty than uncertainty in the thermal expansion coefficients. This should be considered if attempting to back analyse thermal expansion coefficients during heating experiments.

For calibrations, it is recommended that the temperature is calibrated first and then the thermal conductivity and solid heat capacity are fixed for calibrating pore pressure.

The ranking is validated using the multi-method approach proposed in Petropoulos & Srivastava (2016). The three methods provided coherent sensitivity predictions and did not increase the computational time of the analysis.

6.3.3 Effect of anisotropy

An isotropic, axisymmetric model was used to reduce computation time which was necessary for the required high number of model computations. However, the Opalinus Clay is anisotropic, therefore, the isotropic assumption causes a limitation for the input factor space. The uncertainty range cannot be the range in parallel and perpendicular values because this does not represent the uncertainty in the property. That range would be larger than the true uncertainty and exaggerate the sensitivity. Therefore, the average uncertainty range for the parallel and perpendicular values is used and centred on the mean recommended value (Table 4.1). This provides an appropriate uncertainty range because using the mean recommended value as an isotropic property is in line with other publications (Zhang et al., 2007a; Garitte et al., 2017) and benchmarked in Chapter 3.

The limitation is that the sample values for the anisotropic properties do not represent the parallel or perpendicular values. This could provide an inaccurate result if the properties have strongly nonlinear effects, i.e. if a higher, parallel value would be sensitive but a lower perpendicular value would not be sensitive, despite a similar uncertainty range. This limitation could be addressed in future work by performing separate global sensitivity analyses for the parallel and perpendicular properties, doubling the computation time.

6.3.4 Maximising data

In computer science, the number of transistors that can be placed inexpensively on a dense integrated circuit has doubled approximately every two years (Mack, 2011). However, successive generations of computer software increase in size and complexity, offsetting the performance gains of improved dense integrated circuits (Ross, 2003).

Increasing processing speed and memory have been used to increase the complexity of models in earth sciences. Coupled process modelling has increased the number of applications, including heat-producing waste in rock (Garitte et al., 2017). Explicit fracture modelling has increased our understanding of fracture networks (Thomas et al., 2017) and excavation damage zones (Lisjak et al., 2016). 3D representations have simulated anisotropic materials (Gens et al., 2007). However, having the capability to make more complex models should not immediately translate to making more complex models. Models will always be a simplification of reality leading to Box's law (Box & Draper, 1987) which states that all models are wrong (but some models are useful).

Increasing processing speed and memory might also be used to increase the exploration of uncertainty and sensitivity in models and thereby generate more data. Sensitivity analyses have widely recognized potential in earth sciences. Across scientific disciplines, earth sciences produces the second highest density of papers mentioning sensitivity analysis (Saltelli et al., 2019). The discipline relies heavily on large computer models and large-budget models are used for making significant decisions. However, the quality of sensitivity analyses presented in earth sciences is low, ranking second worst according to the ratio that are global sensitivity analysis methods (Saltelli et al., 2019).

In addition to increasing processing speed and memory, computers are getting smaller and cheaper (Feng & Yu, 2019). High performance computing (HPC) facilities exploit this by aggregating computers into clusters (Buyya, 1999). It is difficult to parallelize modelling software (Titarenko & Hildyard, 2017) and the computation time gains do not linearly match the increase in computational power (Hill & Marty, 2008). However, Monte Carlo style sensitivity analyses provide a method for using HPC facilities without parallelizing software. Furthermore, running multiple models in unison realizes the full computation time gains, linearly matching the increase in computational power. This method is fully scalable, from single processors to four core desktops and HPCs.

On a four core desktop, a modeller may run three models in unison whilst maintaining most functionality for other work. When a model completes, another should be submitted. Operating systems (e.g. Microsoft Windows, Linux and DOS) have powerful tools for automating tasks, usually written as executables (e.g. batch files and shell scripts). These should be used with computationally expensive models (e.g. FEM and DEM) in sensitivity analyses to remove the requirement for the user to submit 1000's of models manually. In this work, less than one minute spacing between a model completing and the next being submitted was achieved by automatically checking the processes running on the machine every minute. This was more complex but more efficient and reliable than using a pause with the estimated model run time. In addition to taking advantage of a computers rapid processing, this method also benefits from the fact that computers can be always on.

The future of modelling should be computationally expensive models with complementary, simpler versions for sensitivity and uncertainty analyses. The sensitivity analyses should be automated to maximise data with minimum additional input.

6.4 Microseismic monitoring for GDFs

The objective was to combine microseismic modelling with a THM model to predict possible microseismic events near heat-producing waste during the operation of a generic GDF. This was achieved and the predicted events occurred up to 11 years after waste emplacement (Figure 5.11). This timescale is important because the facility will still be operational (Watson et al., 2009).

6.4.1 Representation of heat-producing waste in rock

The HE-D experiment observed THM coupled processes in lower strength sedimentary rock (Wileveau & Rothfuchs, 2006). The HE-D modelling (Section 3.4) validated the material model and simulation of THM coupled processes. The HE-D experiment did not observe significant damage during heating (Zhang et al., 2007a) and the model did not predict yielding. However, the experiment setup was different to heat-producing waste emplaced in lower strength sedimentary rock.

A THM model was built to simulate heat-producing waste canister and backfill emplacement and early heating. The model was based on the HE-D model (Chapter 3) because it was validated by a benchmark test. The validation demonstrated that the Opalinus Clay material model and the following assumptions were accurate: heat transfer mechanisms are conduction (Fourier's law) through porous medium and advection of liquid water; fluid transport is controlled by liquid water advection (Darcy's law); a THM model is used for the description of the mechanical behaviour of the clay rock with the main features of thermal expansion and poroelasticity; the clay rock is assumed to be homogeneous. The mechanical constitutive model incorporates poroelasticity, material hardening and softening, and tensile, shear and shear-enhanced compaction failure.

The model geometry was changed to the HLW disposal tunnel in lower strength sedimentary rock concept (Figure 6.4). The tunnel radius was increased from 0.15 m to 1.25 m and the heater spacing and dimensions were changed to the canister spacing and dimensions (RWM, 2016a). The thermal load was changed to representative power curves for HLW and AGR spent fuel (Bond & Watson, 2012). The spacing between the canisters and tunnel wall was filled by the backfill material with an emplacement pressure (Dixon et al., 2011) and a swelling pressure over time (Cleall et al., 2006).

A number of simplifications are made to model the HLW and SF disposal tunnel in lower strength sedimentary rock. The sedimentary overburden is simulated as a geostatic load assuming the same density as the host rock. The possible variations in overburden caused by different densities (e.g. 1330 to 2700 kg/m^3) are acceptable

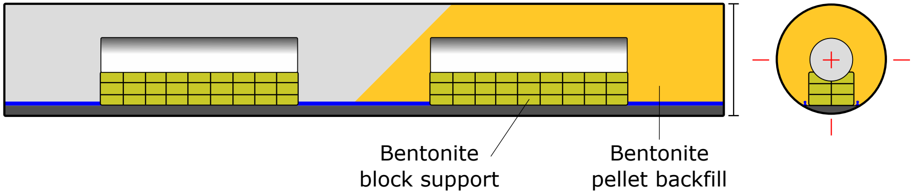

Figure 6.4: Diagram of the RWM lower strength sedimentary rock concept for a HLW and AGR spent fuel disposal tunnel (edited from RWM, 2016a).

within the large range of depths investigated. The parallel disposal tunnels are not modelled because 40 m centres are 7.5 m further than the 10 radii stress perturbation predicted by the elasticity analytical solution (Jaeger et al., 2007). The access tunnel and first 20 m of the disposal tunnel aren't modelled because of the complexity in the changing profiles and orientations (RWM, 2016a). The full 800 m tunnel length is not modelled because it is assumed that the tunnel perturbation is similar along its length away from the ends. Bastiaens et al. (2010) found that a 28 m heater has a central 10 m that is unaffected by the ends of the heater.

The FE experiment in Opalinus Clay (Müller et al., 2018) was a full-scale emplacement experiment simulating construction, waste emplacement (with a heater), bentonite pellet backfilling and early post-closure evolution of the heat-producing waste disposal tunnel for the Swiss repository concept. The RWM concept for lower strength sedimentary rock is based on and analogous to the Swiss repository concept (Nagra, 2002; Lanyon & Gaus, 2016). Data from the FE experiment will provide a good comparison for the modelling in Chapter 5 when it is available.

Concepts can be categorized as horizontal or vertical emplacement, where the model in Section 5.2.1 is representative of horizontal emplacement. Vertical emplacement is typically considered for higher strength host rocks, for example, KBS-3V concept in Sweden (Pettersson & Lönnerberg 2008), Posiva's concept for Olkiluoto, Finland (Alenius, 2015) and RWM's concept for higher strength rock (RWM, 2016a). The main difference is the waste canister is emplaced in a vertical borehole with a 0.875 m radius and backfilled with a 0.29 m ring of bentonite. The excavation stress perturbation is expected to be less significant near the waste because of the smaller radius. Microseismicity (Figure 5.6) is less likely because of the higher strength and lower stress perturbation.

6.4.2 Pseudo scalar seismic moment

Moment tensors store information about the microseismic source magnitude and orientation (Baig & Urbancic, 2010). Moment tensors can be determined in several ways, including stress drop, kinetic energy, or internal forces. Section 5.3 describes the microseismic modelling approach outlined in Angus et al. (2010) to calculate the pseudo scalar seismic moment. The approach was applied in Wang et al. (2018)

using a Mohr Coulomb yield envelope rather than the SR3 yield envelope used in this work and in Angus et al. (2010).

There is no information regarding area of failure or slip, therefore, the pseudo scalar seismic moment is not the moment magnitude. The pseudo scalar seismic moments (Section 5.3) are analogues to earthquake stress drop rather than moment magnitude (Hardebeck & Aron, 2009; McGuire & Kaneko, 2018). The pseudo scalar seismic moment has unit of N/m^2, whereas the actual seismic moment has unit of Nm (Hanks & Kanamori, 1979). Stress drop, similar to moment, is a static measurement of permanent changes caused by an earthquake. Specifically, the stress at the source before and after a seismic event. Microseismic modelling used the true stress. In reality, direct measurements of static stress drop are unknown and estimates for stress drop are dynamic (Brune, 1970).

Stress drop values have large distributions. Shearer et al. (2006) reported 0.2 to 20 MPa for over 60,000 small earthquakes in California, with the majority of the events within 0.5 to 5 MPa. Allmann & Shearer (2009) reported 0.3 to 50 MPa for 2000 globally recorded earthquakes. Microseismic modelling predicts similarly large distributions for stress drop. Angus et al. (2010) reported distributions over three orders of magnitude and centred on 1 MPa. They also found that shear events displayed a wider distribution than shear-enhanced compaction events. The similar distributions between stress drops calculated for observations and modelled stress drops suggests that the wide distributions are real rather than attributable to analysis methods or modelling assumptions (Shearer, 2019).

Microseismic modelling predicted a distribution of 1.5 to 5 MPa for the pseudo scalar seismic moments (Figure 5.11). This distribution is within the published distributions for stress drops. The distribution is tighter because the events are closely related spatially and temporally in comparison to production induced events (Angus et al., 2015), Californian earthquakes (Shearer et al., 2006) and globally recorded earthquakes (Allmann & Shearer, 2009). The symmetric distribution of the predicted pseudo scalar seismic moments near the tunnel (Figure 5.13) represents a typical magnitude distribution of matrix failure (Angus et al., 2010).

Assumption that failure is not aseismic

The pseudo scalar seismic moment (stress drop) is calculated based on the eigensolution of the differential stress tensor using the stress tensor at the source of yielding, before and after the yielding event (Equation 5.2). This approach assumes that every yield event is not aseismic.

Microseismic events can be triggered by tensile failure (Mode I), extensional-shear failure (Mode II) and shear-enhanced compaction (Mode III; Sibson, 2000). During heating, every event occurred by yielding in shear, following the p'-q stress paths illustrated in Figure 5.6. Therefore, they can be classified as Mode II events. Gonidec et al. (2014) recorded Mode II microseismicity during excavation at the Mont Terri Rock Laboratory, providing direct evidence to support the validity of the assumption that yielding in shear can produce Mode II events in the Opalinus Clay. Furthermore, microseismic events have been recorded in shales with downhole arrays (Yu & Shapiro, 2014), shales in the laboratory (Sarout et al., 2017) and mudrocks (Schleicher et al., 2010).

Time dependent strain (Paraskevopoulou and Diederichs, 2018) is more likely to be aseismic. However, the timing of events is known in the model and time dependent strain is not simulated.

6.4.3 Predicted microseismicity

The spatial, temporal and pseudo scalar seismic moment estimate have implications for real radioactive waste disposal scenarios, regardless of the simplicity of the model. Microseismic modelling predicted microseismicity up to 11 years after waste emplacement (Figure 5.11). Furthermore, all models with microseismicity after waste emplacement had microseismicity within the first year. The spatial distribution was across the full length of the tunnel with modes centred on the waste canisters (Figure 5.11). The waste canisters seismic signatures were similar (Figure 5.13).

Figure 5.6 shows the p'-q stress paths for the post-emplacement events. Excavation increases the differential stress and reduces the mean effective stress, often causing yielding in shear. Yielding in shear causes softening where the yield envelope contracts. Pore pressure increases quickly after waste emplacement, similar to the HE-D experiment which observed up to 4 MPa increases in pore pressure over 130 days (Figure 6.1). Increasing pore pressure shifts the p'-q stress to the left and caused yielding in shear in 13.4 % of the models (Figure 5.10).

Thermal expansion of the fluid and increasing pore pressure is the cause of the microseismicity, however, it is the preceding stress conditions created by the excavation that control whether microseismicity occurs or not. The HE-D model (Section 3.4) did not predict microseismicity because the URL is shallow at around 300 m depth (Thury & Bossart, 1999) and the heater borehole radius was small at 0.15 m. The stress perturbation from a circular excavation is negligible at a radial distance of ten times the radius (Jaeger et al., 2007). Therefore, over the radial distance that the stress perturbation is significant, the drained borehole maintains lower pore pressures.

Higher magnitude events occur nearer the tunnel wall (Figure 5.13) because the stress redistribution is greatest at the tunnel wall. A random forest algorithm prediction (Section 5.4.3) demonstrated that this is so significant that the magnitude and time of an event can be used to predict whether its radial distance is greater than or less than 0.25 m from the tunnel wall. The prediction success is aided by the mesh element constraints on the event locations, therefore, the 100 % accuracy would not be expected outside of modelling. Larger events nearer the tunnel was in line with expectations and comparable to excavation scenarios (Chen et al., 2018).

Undrained triaxial tests with heating on Opalinus Clay specimens observe a factor of four strength reduction from 20 MPa at 20 $^{\circ}C$ to 5 MPa at 116 $^{\circ}C$, for a lateral stress of 3 MPa (Zhang et al., 2007b). The weakness is caused by thermally-induced excess pore pressure decreasing the mean effective stress. This is comparable to the yield events in Figure 5.6, which occur between 2 MPa and 8 MPa differential stress with 1.5 MPa and 6 MPa mean effective stress respectively.

Sensitivity of rock properties

Sensitivity analyses on Opalinus Clay material properties in Chapter 4 ranked the rock and fluid properties according to their sensitivity to mean effective stress and pore pressure, given the uncertainty ranges characterized for the HE-D experiment site. The analyses ranked the in situ stress, in situ pore pressure, Biot's coefficient, thermal conductivity, thermal expansion coefficient and permeability highly (Table 4.2).

Increasing in situ stress, in situ pore pressure, Biot's coefficient, thermal conductivity and thermal expansion coefficient will all increase the likelihood of microseismicity. Increased thermal conductivity will increase temperatures and therefore, pore pressures. Increased in situ pore pressure and thermal expansion coefficient will increase pore pressure. An increase in pore pressure will decrease mean effective stress more for a higher Biot's coefficient (Equation 3.6). Excavation stress redistribution will cause a greater differential stress for a greater in situ stress. Increasing permeability will decrease the likelihood of microseismicity by decreasing pore pressure. Therefore, unexpected spatial variations in microseismicity may indicate heterogeneity in these rock properties.

Effect of anisotropy

The model uses an isotropic assumption for the Opalinus Clay which accurately simulates coupled processes (Figures 3.17 and 3.18) but does not predict the 3D behaviour (Garitte et al., 2010; Garitte et al., 2017). The anisotropic properties of Opalinus Clay include Young's modulus, permeability, thermal conductivity and linear thermal expansion coefficient (Bock, 2001). These anisotropic properties are greater in the parallel direction than perpendicular direction relative to bedding. The uniaxial compressive strength is greater perpendicular to bedding than parallel to bedding. In situ stress is also anisotropic and typically vertical stress is greater than horizontal stresses (McGarr & Gay, 1978).

It is expected that the higher thermal conductivity and lower strength parallel to bedding will increase the maximum radial distance of microseismicity parallel to bedding. This would be consistent with excavation induced damage and microseismicity in Opalinus Clay (Lisjak et al., 2015).

6.4.4 Input factor space

A broad range of scenarios were investigated for microseismicity. The depth range was 200 to 1000 m which represents the current constraints on the depth of a GDF in the UK (RWM, 2016a). Increasing depth increased the likelihood for microseismicity post waste emplacement (Figure 5.9). However, a GDF in lower strength sedimentary host rock is expected to be towards the lower end of the depth constraints. 500 m is assumed for lower strength sedimentary rocks and 750 m for higher strength sedimentary rocks. A range of 250 to 600 m (Figure 2.1) is more likely for a GDF in lower strength sedimentary host rock.

A normalized over- and under-pressure range of 0.9 to 1.1 was investigated for in situ pore pressure. Lower strength sedimentary rocks are more likely to be over-pressured because the amount of overburden stress carried by the pore fluid increases for more compressible rocks (Osborne & Swarbrick, 1997). Furthermore, lower permeability sustains over-pressure during uplift (David et al., 1994). A range was investigated to determine the effect trend of changing in situ pore pressure on microseismicity. The range was small because the actual uncertainty is unknown. Higher over-pressure increased microseismicity during excavation (Figure 5.8) but had negligible effect during heating.

Tunnel support pressure, backfill emplacement pressure and backfill swelling pressure are all outward pressures onto the tunnel wall. These pressures increase the radial stress which is reduced by the excavation. The increase in radial stress increases the mean effective stress and decreases the deviatoric stress, both of which move the stress path, in p'-q space, away from yielding in shear (Figure 5.6).

A limitation of the work is that the tunnel support is simulated by filling the excavated void with a lower stiffness material. A zero-displacement constraint is removed at the moment of excavation, allowing the rock to relax into the lower stiffness material, therefore, the void never exists. This approach was used successfully in Lisjak et al. (2015). The limitation is that the tunnel support pressure is not defined explicitly and becomes a function of the in situ stress. True tunnel support is similar, rock bolts and shotcrete, etc. have a strength and stiffness (Neuner et al., 2017) and the tunnel support pressure they exert is reactionary to the in situ stress. However, for the purposes of modelling, it is more informative to consider the tunnel support pressure (Hoek, 2018).

Constraining the backfill swelling pressure

Demonstrating a mechanism for microseismicity during early post waste emplacement was an important output for this work. Even more important, was the ability to demonstrate that observable properties of the microseismicity could be used to improve our understanding of the GDF performance during its operational stage. Figures 5.15 and 5.16 show that the microseismic event times, distances and pseudo scalar seismic moments are influenced by the backfill swelling pressure. Then, linear regression was applied to determine the effect of the microseismic event data on the likely backfill swelling pressure (Figures 5.17 and 5.18).

The linear regression model was shown to be significant using the p-value (Section 5.4.3) and appropriate using residual analysis (Figure 5.17). The R^2 value indicated that the model explains 28.5 % of the variability in backfill swelling pressure. The results suggest microseismic monitoring could constrain the backfill swelling pressure but the low R^2 value indicates that the constraints should be considered as increasing likelihood rather than accurate history matching. The large uncertainties in this sensitivity analysis will be reduced by site selection and characterization. For example, the depth will be known to a cm accuracy. Therefore, the R^2 value may increase if the analysis is repeated when the site is characterized.

Microseismicity would provide direct evidence that the engineered barrier is not behaving as expected, i.e. not providing enough confining pressure. The large-scale in situ SELFRAC-I experiment simulated the swelling pressures of bentonite using a plate load of 4.8 MPa (Lisjak et al., 2016). The transmissivity of the excavation damage zone was decreased by several orders of magnitude in Opalinus Clay. The experiment demonstrates the importance of the backfill swelling pressure for the engineered barrier system. Understood in this context, microseismicity would indicate that the engineered barrier system had not yet facilitated the self-sealing properties of the lower strength sedimentary rock (Grambow, 2016) and that the transmissivity of the excavation damage zone is still high.

The linear regression model trends can be used to support robust decision-making (Singh et al., 2014). Figures 5.17 and 5.18 show that increasing maximum time, mean time, maximum radial distance, mean radial distance, maximum pseudo scalar seismic moment, total number of events and decreasing the minimum pseudo scalar seismic moment all decrease the likely backfill swelling pressure. Furthermore, the gradients provide quantitative values for the changes in likely backfill swelling pressure.

6.5 Summary

In situ experiments provide benchmark test opportunities for complex numerical modelling. The process of benchmarking the models in this work was an important one that discovered fixable inaccuracies in the approach that otherwise might have been overlooked. The process of improving the model representation of the experiment to fit the prediction to the data provided an understanding that led to the discovery of the mechanism for the opposite effect phenomenon in pore pressure (Section 3.5.2).

Axisymmetric modelling was used to enable computationally expensive methods requiring multiple model runs. A strong case is made for not overlooking simpler models for the purposes of always simulating anisotropy.

The benchmarked model was particularly suitable for a sensitivity analysis on the Opalinus Clay material properties characterized at a URL. The results are an important, first-comprehensive-look at the sensitivity of the remaining uncertainty in rock properties to mean effective stress, temperature, pore pressure and displacement. The uncertainty in Biot's coefficient must be included in discussions on the pore pressure as well as the mean effective stress.

The potential for microseismic monitoring to improve understanding of the processes occurring around heat-producing waste during the operation of a generic GDF was demonstrated, quantified and discussed. A strong case is made for continued microseismic monitoring post heat-producing waste emplacement to constrain backfill swelling pressures.

Chapter 7

Conclusions

7.1 Aim and approach

The aim of this work was to investigate the potential for using seismic monitoring methods to enhance rock characterization and understanding of the processes occurring in the rock surrounding heat-producing waste.

The approach was firstly, to create a model that realistically simulated heat-producing waste in a lower strength sedimentary rock. This was achieved by simulating the HE-D in situ heater test in Opalinus Clay and validating the prediction by comparing it to the experiment results (Chapter 3). Then, Monte Carlo style simulation and global sensitivity analyses were performed on the model to screen and rank the uncertainty in rock properties according to their sensitivities to mean effective stress, pore pressure, displacement and temperature (Chapter 4). The most sensitive properties have the most potential for constraining further, using observations relating to mean effective stress and pore pressure. The model was adapted to represent the RWM concept for HLW and AGR spent fuel disposal tunnels in lower strength sedimentary rock. Microseismic modelling was combined with the model to predict the associated microseismicity (Chapter 5). Monte Carlo style simulation was performed to investigate a range of engineering scenarios and global sensitivity analyses and regression analysis were used to relate the engineering scenarios to microseismic event pseudo scalar seismic moments and locations in space and time.

7.2 Originality

The novel aspects of the thesis were benchmarking ELFEN using an in situ heater test, adding ELFEN to the list of software that have accurately predicted THM coupled processes for radioactive waste disposal (Chapter 3). Furthermore, demonstrating global sensitivity analysis methods for computationally expensive THM, FEM models (Chapter 4). A method for reducing the number of uncertain input factors and a method for ranking input factors were demonstrated. Finally, integrating microseismic modelling with THM modelling for predicting microseismic events associated with the geological disposal of radioactive waste (Chapter 5).

7.3 Findings

Thermal poroelasticity in a coupled THM, FEM model in ELFEN is benchmarked against the HE-D in situ heater experiment to validate the software for simulating heat-producing radioactive waste emplaced in lower strength sedimentary rocks. The results were accurate with the exception of discrepancies introduced at some sensors by the axisymmetric, isotropic simplification of the anisotropic Opalinus Clay (Section 3.5).

The coupled THM behaviour of the Opalinus Clay during the HE-D experiment is better understood. In particular, it is shown that the drained borehole causes the immediate and opposite to what is expected reactions of pore pressure to changes in the heater output (Section 6.2.2).

The benchmarked model provided an excellent opportunity for a global sensitivity analysis because the benchmark test validates the model as a good representation of reality. Furthermore, the boundary conditions of the model are well constrained, reducing the uncertainty to the rock characterization. Finally, the rock in the test site was well characterized, similar to what is expected for a lower strength sedimentary host rock. Axisymmetric modelling and high performance computing were combined to introduce computationally expensive global methods to sensitivity analyses of THM, FEM models (Section 4.3).

Uncertainty in lower strength sedimentary rock and fluid properties characterized at a URL has been screened to reduce the number of properties that should still be considered uncertain. The analysis significantly reduced the number of parameters required to predict mean effective stress, temperature, pore pressure and displacement (Section 4.4). This result can be used to improve the efficiency of sensitivity analyses, uncertainty analyses and model calibrations to observations. Furthermore, convergence analysis found that 1870 (corresponding to a base sample size, n, of 85, Equation 4.12) model runs were required to reach screening convergence for 21 input factors in a THM, FEM model.

The rock and fluid properties were ranked according to their sensitivity to mean effective stress, temperature, pore pressure and displacement (Section 4.4). One-at-a-time sensitivity analyses for Opalinus Clay typically investigate Young's modulus and permeability. The ranking found that the uncertainties in initial stress, initial pore pressure and Biot's coefficient are more sensitive than the stiffness and permeability for the mean effective stress. These are the most likely parameters to be able to constrain, by calibrating models with microseismic monitoring during heating, because the microseismic events will be caused by a reduction in mean effective stress.

A similar axisymmetric model was built using the same material properties. The geometry was changed to simulate a HLW and spent fuel disposal tunnel allowing for the excavation, backfill pressure and backfill swelling pressure to be simulated (Section 5.2.1). Potential GDF scenarios were explored using the same Monte Carlo style techniques as Chapter 4. Microseismic modelling was built into the methodology to predict the spatial, temporal and pseudo-scalar seismic moment of microseismic events (Section 5.3).

A mechanism for microseismicity post-emplacement of heat-producing radioactive waste in lower strength sedimentary rocks has been demonstrated. Microseismic events were predicted in models when the mean effective stress was decreased because of increasing pore pressure and the differential stress was high because of low radial stresses near to the tunnel (Section 5.4.1).

Exploration of microseismicity mapped onto engineering related parameters showed that the microseismicity was dependent on the facility depth and the outward pressure exerted from the tunnel by tunnel support, backfill emplacement and backfill swelling pressure (Section 5.4.2). The likely backfill swelling pressure can be constrained by post-emplacement microseismic monitoring. Increasing number of events, maximum and mean time of events, maximum and mean radial distance of events and maximum pseudo scalar seismic moment all indicate the likelihood of a lower backfill swelling pressure (Section 5.4.3). Therefore, microseismic monitoring is a potential source of information for the performance of the engineered barrier.

7.4 Applications

Efforts towards reduction of uncertainty in rock properties should focus on the in situ stress and Biot's coefficient. Future modelling should include automated global sensitivity analyses to increase the value of the model in terms of data and understanding. Uncertainty in the grain density and fluid properties, including viscosity and excluding thermal expansion, should not be included in global sensitivity analyses on lower strength sedimentary rocks. Microseismic monitoring should be used post-emplacement of heat-producing radioactive waste for insights into developing pore pressure, mean effective stress and the engineered backfill swelling pressure.

7.5 Future work

The microseismic modelling (Chapter 5) should be extended to 3D with anisotropic properties. The aim would be to predict a more realistic spatial distribution of microseismicity and to investigate the effect of backfill swelling pressures on bedding parallel permeability.

Higher strength host rock investigations

As discussed in Section 6.2, the results in this work may not be applicable to higher strength host rocks. Therefore, future work should repeat the sensitivity analyses (Chapter 4) and microseismic modelling (Chapter 5) for higher strength rocks. Models should use DEM and discrete fracture networks with fracture initiation and propagation (Xiang et al., 2009). Fluid flow should be predominantly through the connected fractures (Lang et al., 2018) which may require simulating laminar flow (Zhu, 2019). Accurately simulating conductivity will require complex shaped multi bodied contact (Joulin et al., 2017). The sensitivity analysis should consider uncertainty in the fracture network, towards which, advances in deep learning should be considered for automated geometry generation (Mosser et al., 2017; 2018). Finally, the microseismic modelling should calculate the actual seismic moments (Khazaei et al., 2016), using Equation 2.1, because the slip and fracture area will be known.

Time lapse seismic monitoring for geological disposal facilities

Time-lapse seismic monitoring compliments microseismic monitoring methods because a 3D velocity map is required to spatially locate the microseismic events passively recorded at receivers (e.g. Gonidec et al., 2014). Seismic geomechanics (Herwanger & Koutsabeloulis, 2011) combines time-lapse seismic velocity data and geomechanical modelling using rock physics models (e.g. Sayers, 2002; Tod, 2002; Prioul et al., 2004; Shapiro & Kaselow, 2005; Hall et al., 2008; Sarout & Guéguen, 2008; Ougier-Simonin et al., 2009; Guéguen & Sarout, 2011; Korneev & Glubokovskikh, 2013). Future work should apply rock physics modelling to predict time-lapse seismic velocity maps using the anisotropic, effective stress predictions from the modelling in Chapter 5. Rock physics models would need to be calibrated using laboratory experiments or core velocity-stress measurements (e.g. Angus & Price, 2016). The investigation should aim to show whether time-lapse seismic monitoring can improve our understanding of effective stress after waste emplacement. The two-way travel time perturbation (He et al., 2015) for receivers in the tunnels (Bentham et al., 2018) would be an appropriate indicator.

There is potential to combine the proposed future work ideas to relate modelled excavation damage zone evolution, in a higher strength host rock, to time-lapse changes in the seismic velocity map (Schuster et al., 2018).

REFERENCES

Abu-Hamdeh, N.H. 2003. Thermal Properties of Soils as affected by Density and Water Content, *Biosystems Engineering*, **86**(1), 97–102, ISSN 1537–5110, https://doi.org/10.1016/S1537-5110(03)00112-0.

Alassi, H.T. 2008. Modelling reservoir geomechanics using discrete element method: Application to reservoir monitoring. *Ph.D. Thesis*, NTNU, Norway.

Alenius, M. 2015. Review of Engineered Barrier System (EBS) topics in Posiva's construction license application for a spent fuel repository at Olkiluoto, Finland. STUK-TR 18.

Allan, C.J. & Nuttall, K. 1997. How to cope with the hazards of nuclear fuel waste, *Nuclear Engineering and Design*, **176**, 1–2, 51–66, ISSN 0029-5493, https://doi.org/10.1016/S0029-5493(96)01331-3.

Allmann, B. P. & Shearer, P. M. 2009. Global variations of stress drop for moderate to large earthquakes, *J. Geophys. Res.*, **114**, B01310, doi:10.1029/2008JB005821.

Altmann, S. 2008. 'Geo'chemical research: A key building block for nuclear waste disposal safety cases. *Journal of Contaminant Hydrology*, **102**, 3–4, 174–179, ISSN 0169–7722, https://doi.org/10.1016/j.jconhyd.2008.09.012.

Amec Foster Wheeler. 2015. Project Ankhiale: Estimating the uplift due to high-heat-generating waste in a Geological Disposal Facility, 103727-0003-UA00-TLN-0001, **3**.

ANDRA. 2005. Dossier Argiles: Tome Evaluation de Sûreté du Stockage Géologique. ANDRA Report C.RP.ADS.04.0022.

Andres TH. 1997. Sampling methods and sensitivity analysis for large parameter sets. *Journal of Statistical Computation and Simulation*, **57**, 77–110.

Angus, D.A.C., Kendall, J.-M., Fisher, Q.J., Segura, J.M., Skachkov, S., Crook, A.J.L. & Dutko, M. 2010. Modelling microseismicity of a producing reservoir from coupled fluid-flow and geomechanical simulation. Geophysical Prospecting, **58**, 5, 901–914, DOI: 10.1111/j.1365-2478.2010.00913.x.

Angus, D.A.C., Dutko, M., Kristiansen, TG. et al. 2015. Integrated hydromechanical and seismic modelling of the Valhall reservoir: A case study of predicting subsidence, AVOA and microseismicity. *Geomechanics for Energy and the Environment*, **2**, 32–44. ISSN 2352-3808.

Angus, D.A.C. & Price, D. 2016. Probabilistic Comparison of Stress Dependent Rock Physics Models. 78th EAGE Conference and Exhibition 2016. Rock Physics III - Interpretation and Stress Dependency. DOI: 10.3997/2214–4609.201601235 .

Aranyossy, J. F., Mayor, J. C., Marschall, P., Plas, F., Blumling, P., Van Geet, M., Armand, G., Techer, I., Alheid, A. J., Rejeb, A., Pinettes, P., Balland, C., Popp, T., Rothfuchs, T., Matray, J. M., De Craen, M., Wieczorek, K., Pudewills, A., Czaikowski, O., Hou, Z., & Fröhlich, H. 2008. EDZ Development and Evolution (RTDC 4). *In nuclear science and technology. Understanding and Physical and Numerical Modelling of the Key Processes in the Near Field and their Coupling for Different Host Rocks and Repository Strategies NF-PRO) Final Synthesis Report (D. 4.5.3).* FP6-EURATOM/NF-PRO, F16W-CT-2003-02389 (pp. 150–197). European Commission, Luxembourg.

Armand, G., Leveau, F., Nussbaum, C., de La Vaissiere, R., Noiret, A., Jaeggi, D., Landrein, P. & Righini, C. 2014. Geometry and Properties of the Excavation-Induced Fractures at the Meuse/Haute-Marne URL Drifts. *Rock Mech Rock Eng*, **47**, 21. https://doi.org/10.1007/s00603-012-0339-6.

Arrhenius, S.A. 1889. Über die Dissociationswärme und den Einfluß der Temperatur auf den Dissociationsgrad der Elektrolyte. *Z. Phys. Chem.*, **4**, 96–116, doi:10.1515/zpch-1889-0408.

Baig, A. & Urbancic, T. 2010. Microseismic moment tensors: A path to understanding frac growth. *The Leading Edge*, **29**, 3, 320–324, https://doi.org/10.1190/1.3353729.

Ballester, P.J. & Carter, J.N. 2007. A parallel real-coded genetic algorithm for history matching and its application to a real petroleum reservoir. *Journal of Petroleum Science and Engineering*, **59**(3), 157–168.

Barkved O.I. 2004. Continuous seismic monitoring. *SEG Technical Program Expanded Abstracts*, 2537–2540, https://doi.org/10.1190/1.1851258.

Bartl, U. & Czurda, K.A. 1991. Migration and retention phenomena of radionuclides in clay-barrier systems. *Applied Clay Science*, **6**, 3, 195–214, ISSN 0169-1317, https://doi.org/10.1016/0169-1317(91)90025-5.

Baud, P., Laurent, L., Christian, D., Geoffrey, C.R. & Wong, T-F. 2005. Effects of bedding and foliation on mechanical anisotropy, damage evolution and failure mode. Geological Society, London, Special Publications, **245**, 223–249, https://doi.org/10.1144/GSL.SP.2005.245.01.11.

Belmokhtar, M., Delage, P., Ghabezloo, S., Tang, AM., Menaceur, H. & Conil, N. 2017. Poroelasticity of the Callovo-Oxfordian Claystone. *Rock Mechanics and Rock Engineering.* **50**, 4, 871–889.

BEIS & NDA, 2016. Radioactive Wastes in the UK: UK Radioactive Waste Inventory Report.

Bentham, H. & Morgan, J.V. & Angus, D. 2018. Investigating the use of 3D full-waveform inversion to characterise the host rock at a geological disposal site. *Geophysical Journal International*, **215**. 10.1093/gji/ggy386.

BGS. 2015. [Online]. [Accessed 9 May 2017]. Available from: https://www.bgs.ac.uk/scienceFacilities/boreholeGeophysics.

BGS. 2018. National Geological Screening: Central England region. British Geological Survey, Minerals and Waste Programme Commissioned Report, CR/17/091. 77pp. E Hough, D Schofield, T Pharaoh, R Haslam, S Loveless, J P Bloomfield, J R Lee, B Baptie, R P Shaw, T Bide and F M McEvoy.

Birkholzer, J.T., Bond, A.E., Hudson, J.A., Jing, L., Tsang, C-F., Shao, H. & Kolditz, O. 2018. DECOVALEX-2015: an international collaboration for advancing the understanding and modeling of coupled thermo-hydro-mechanical-chemical (THMC) processes in geological systems. *Environmental Earth Sciences*, **77**(14), 539, 1866–6299, 10.1007/s12665-018-7697-7.

Bock H. 2001. RA Experiment - Rock mechanics analyses and synthesis: Data Report on Rock Mechanics. Technical Report 2000–02.

Bond, A. & Watson, S. 2012. Understanding the Post-closure Thermal Impact of HLW/SF Waste Packages. Quintessa Report QRS-1384Q-R2 Version 2.1 for the NDA RWMD. Quintessa Ltd, Henley.

Bond, A., Millard, A., Nakama, S., Zhang, C., & Garritte, B. 2013. Approaches for representing hydro-mechanical coupling between sub-surface excavations and argillaceous porous media at the ventilation experiment, Mont Terri, *Journal of Rock Mechanics and Geotechnical Engineering*, **5**, 2, 85–96, ISSN 1674-7755, https://doi.org/10.1016/j.jrmge.2013.02.002.

Bossart, P., Meier, P.M., Moeri, A., Trick, T. and Mayor, J.C. 2002. Geological and hydraulic characterisation of the excavation disturbed zone in the Opalinus Clay of the Mont Terri Rock Laboratory. *Engineering Geology*, **66**, 1–2, pp.19–38.

Bossart, P., Bernier F., Birkholzer, J., Bruggeman, C., Connolly, P., Dewonck, S., Fukaya, M., Herfort, M., Jensen, M., Matray, J., Mayor, J.C., Moeri, A., Oyama, T., Schuster, K., Shigeta, N., Vietor, T., Wieczorek, K. 2017. Mont Terri rock laboratory, 20 years of research: introduction, site characteristics and overview of experiments. *Swiss Journal Geoscience*, **110**, 3.

Box, G. E. P., & Draper, N. R. 1987. Wiley series in probability and mathematical statistics. Empirical model-building and response surfaces. Oxford, England: John Wiley & Sons.

Broichhausen, H., Littke, R., Hantschel, T. 2005. Mudstone compaction and its influence on overpressure generation, elucidated by a 3D case study in the North Sea. *Int. J. Earth Sci.*, **94**, 5–6, 956–978.

Buyya, R. (Ed.), High Performance Cluster Computing: Architectures and Systems, vol.1, Prentice Hall, Upper Saddle River, USA, 1999.

Cacas, M. C., E. Ledoux, G. DE Marsily, B. Tillie, A. Barbreau, E. Durand, B. Feuga & P. Peaudecerf. 1990. Modeling Fracture Flow With a Stochastic Discrete Fracture Network: Calibration and Validation. 1. The Flow Model. *Water Resources Research*, **26**, 3, 479–489.

Campolongo F., Cariboni J and Saltelli A. 2007. An effective screening design for sensitivity analysis of large models. *Environmental Modelling Software*, **22**, 10, 1509–1518.

Campolongo F., Saltelli A and Cariboni J. 2011. From screening to quantitative sensitivity analysis. A unified approach. *Computer Physics Communication*, **182**, 4, 978–988.

Carman, P.C. 1937. Fluid flow through a granular bed. *Trans. Inst. Chem*, England, London, **15**, 150–156.

Carslaw, H. S. & Jaeger, J. C. 1959. Conduction of heat in solids. Oxford: Clarendon Press, 1959, 2nd ed.

Cekerevac, C. & Laloui, L. 2004. Experimental study of thermal effects on the mechanical behaviour of a clay. *Int. J. Numer. Anal. Meth. Geomech.*, **28**, 3, 209–228. https://doi.org/10.1002/nag.332.

Chen, G.J., Sillen, X., Verstricht, J., Li, X.L. 2011. ATLAS III in situ heating test in boom clay: Field data, observation and interpretation, *Computers and Geotechnics*, **38**, 5, 683–696, ISSN 0266-352X, https://doi.org/10.1016/j.compgeo.2011.04.001.

Chen, F., Tianhui Ma, Chun'an Tang, Yanhong Du, Zhichao Li, and Fei Liu, 2018. Research on the Law of Large-Scale Deformation and Failure of Soft Rock Based on Microseismic Monitoring, *Advances in Civil Engineering*, Article ID 9286758, https://doi.org/10.1155/2018/9286758.

Chen, Z., Montavon, G., Ribet, S., Guo, Z., Robinet, J.C., David, K., Tournassat, C., Grambow, B., Landesman, C. 2014. Key factors to understand in-situ behavior of Cs in Callovo–Oxfordian clay-rock (France). *Chemical Geology*, **387**, 47–58, ISSN 0009-2541, https://doi.org/10.1016/j.chemgeo.2014.08.008.

Cleall, P.J., Melhuish, T.A. & Thomas, H.R. 2006. Modelling the three-dimensional behaviour of a prototype nuclear waste repository, *Engineering Geology*, **85**, 1–2, 212–220, ISSN 0013-7952, https://doi.org/10.1016/j.enggeo.2005.09.045.

Committee on Radioactive Waste Management, Managing our Radioactive Waste Safely - CoRWM's Recommendations to Government, July 2006. CoRWM Document 700. Available at www.corwm.org.uk.

Conil N., Armand G, Garitte B, Jobmann M, Jellouli M, Filippi M, De La Vaissière R and Morel J. 2012. In situ heating test in Callovo-Oxfordian claystone: measurement and interpretation. In Proceeding of the 5th International meeting of Clays in Natural and Engineered Barriers for Radioactive Waste Confinement, Montpellier, October 22-25.

Cosenza, A., Mannina G, Vanrolleghem PA and Neumann MB. 2013. Global sensitivity analysis in wastewater applications: a comprehensive comparison of different methods. *Environmental Modelling and. Software*, **49**, 40–52.

Cosgrove, J.W. & Hudson, J.A. 2016. Structural Geology and Rock Engineering. London: Imperial College Press.

Crisci, E., Ferrari, A., Giger, S.B. & Laloui, L. 2019. Hydro-mechanical behaviour of shallow Opalinus Clay shale. *Engineering Geology*, **251**, 214–227, ISSN 0013-7952, https://doi.org/10.1016/j.enggeo.2019.01.016.

Crook, T., Willson, S., Yu, J.G. & Owen, R. 2003. Computational modelling of the localized deformation associated with borehole breakout in quasi-brittle materials. *Journal of Petroleum Science and Engineering*, **38**, 3–4, 177–186, ISSN 0920-4105, https://doi.org/10.1016/S0920-4105(03)00031-7.

Crook, A.J.L., Owen D.R.J., Willson S.M., Yu J.G. 2006. Benchmarks for the evolution of shear localization with large relative sliding in frictional materials. *Comput Methods Appl Mech Eng* **195**, 4991–5010.

Crook, A.J.L., Yu, J. G., Flatebo, R. E., & Kristiansen, T. G. 2008. Computational Modelling of the Rate Dependent Deformation and Liquefaction of Chalk. American Rock Mechanics Association.

Cuenot, N., Dorbath, C. & Dorbath, L. 2008. Analysis of the Microseismicity Induced by Fluid Injections at the EGS Site of Soultz-sous-Forêts (Alsace, France): Implications for the Characterization of the Geothermal Reservoir Properties. *Pure appl. geophys.*, **165**, 797. https://doi.org/10.1007/s00024-008-0335-7.

Cui, W., Potts, D. M., ZdravkoviÄ‡, L., Gawecka, K. A., & Taborda, D. M. (2018). An alternative coupled thermo-hydro-mechanical finite element formulation for fully saturated soils. *Computers and Geotechnics*, **94**, 22–30.

David, C., Wong, TF., Zhu, W. & Zhang, J. 1994. Laboratory measurement of compaction-induced permeability change in porous rocks: Implications for the generation and maintenance of pore pressure excess in the crust. Pure and applied geophysics, 143, 1, 425–456, https://doi.org/10.1007/BF00874337.

Davies, C. and Bernier, F. (eds.). 2005. Impact of the Excavation Disturbed or Damaged Zone (EDZ) on the Performance of Radioactive Waste Geological Repositories. Proceedings of a European Commission Cluster Conference and Workshop in Luxembourg, 3-5 November 2003. European Commission, Brussels.

De Gennaro, S., Schutjens, P., Frumau, M., Fuery, M., Ita, J. & Fokker, P., 2010. The role of geomechanics in the development of an HPHT field. *American Rock Mechanics Association*, 10-450.

Dean, R.H., Gai, X., Stone, C.M. & Minkoff, S.E., 2006. A comparison of techniques for coupling porous flow and geomechanics. Spe Journal, 11(1), 132-140. 3, 14.

DECC, 2014. Implementing geological disposal: a framework for the long-term management of higher activity radioactive waste (DECC, 2014).

DECOVALEX. 2014. About DECOVALEX: Overview and Objectives. [Online]. [Accessed 5 October 2018]. Available from: https://decovalex.org/about.html.

DEFRA et al. (2018) Scope Of And Exemptions From The Radioactive Substances Legislation in England, Wales AND Northern Ireland.

Delage, P., Sultan, N. & Cui, Y.J. (2000). On the thermal consolidation of Boom clay. *Canadian Geotechnical Journal*, **37**, 343–354, https://doi.org/10.1139/t99-105.

Dixon, D., Sanden, T., Jonsson, E., & Hansen, J. (2011). Backfilling of deposition tunnels: Use of bentonite pellets (SKB-P–11-44). Sweden.

Donald, I.W. Waste Immobilization in Glass and Ceramic Based Hosts. Wiley, Chichester, UK, 2010.

Dou, L., Lu, C., Mu, Z. & Gao, M. (2009). Prevention and forecasting of rock burst hazards in coal mines. *Mining Science and Technology (China)*, **19**, 5, 585–591, https://doi.org/10.1016/S1674-5264(09)60109-5.

Drews, M.C., Bauer, W., Caracciolo, L. & Stollhofen, H. (2018). Disequilibrium compaction overpressure in shales of the Bavarian Foreland Molasse Basin: results and geographical distribution from velocity-based analyses. *Mar. Petrol. Geol.*, **92**.

Drucker, D.C., & Prager, W. (1952). Soil mechanics and plastic analysis or limit design. *Quarterly of applied mathematics*, **10**(2), 157–165.

Emerick, A.A. & Reynolds, A.C. (2012). History matching time-lapse seismic data using the ensemble Kalman filter with multiple data assimilations. *Computational Geosciences*, **16**(3), 639-659.

Environment Agency (2009). Technical issues associated with deep repositories for radioactive waste in different geological environments. Science report: SC060054/SR1.

Evans, K.F., Cornet, F.H., Hashida, T., Hayashi, K., Ito, T., Matsuki, K. & Wallroth, T. (1999). Stress and rock mechanics issues of relevance to HDR/HWR engineered geothermal systems: review of developments during the past 15 years.

Geothermics, **28**, 4–5, 455–474, ISSN 0375-6505, https://doi.org/10.1016/S0375-6505(99)00023-1.

Disposal of Nuclear Waste Geological Challenges in Radioactive Waste Isolation Fifth Worldwide Review. Boris Faybishenko, Jens Birkholzer, Peter Persoff, David Sassani, and Peter Swift. 2016.

Feng, J. & Yu, K. (2019) Moore's law and price trends of digital products: the case of smartphones, Economics of Innovation and New Technology, DOI: 10.1080/10438599.2019.1628509.

Fjaer, E. & Kristiansen, T.G. (2009). An integrated geomechanics, rock physics and seismic model. 71st EAGE Conference & Exhibition, Amsterdam. 17.

Forrester, A., Sobester, A. & Keane, A. (2008). Engineering design via surrogate modelling: A practical guide. John Wiley & Sons. 52.

Fraser Harris, A.P., McDermott, C.I., Kolditz, O., Haszeldine, R.S. (2015). Modelling groundwater flow changes due to thermal effects of radioactive waste disposal at a hypothetical repository site near Sellafield, UK. *Environ Earth Sci* **74**, 1589–1602. DOI 10.1007/s12665-015-4156-6.

Fu, P., Johnson, S.M. & Carrigan, C.R. (2012). An explicitly coupled hydro-geomechanical model for simulating hydraulic fracturing in arbitrary discrete fracture networks. *Numerical and Analytical Methods in Geomechanics*, https://doi.org/10.1002/nag.2135.

Galson and Crawford, 2013. Technical Report. Treatment of Coupled Processes in Geological Disposal. Review of UK Work, and Treatment of Coupled Processes in Performance Assessments in other Countries. D.A. Galson and M.B. Crawford, Galson Sciences Ltd.

Gao, X., Yan, E. C., Yeh, T. C. J., Wang, Y. L., Cai, J. S., & Hao, Y. H. (2018). Sequential back analysis of spatial distribution of geomechanical properties around an unlined rock cavern. Computers and Geotechnics, 99, 177–190, ISSN 0266-352X, https://doi.org/10.1016/j.compgeo.2018.03.007.

García-Siñeriz, J. L., Villar, M. V., Rey, M., & Palacios, B. (2015). Engineered barrier of bentonite pellets and compacted blocks: state after reaching saturation. Engineering geology, 192, 33–45, ISSN 0013-7952, https://doi.org/10.1016/j.enggeo.2015.04.002.

Vikram V. Garg & Roy H. Stogner (2017) Hierarchical Latin Hypercube Sampling, Journal of the American Statistical Association, 112:518, 673-682, DOI: 10.1080/01621459.2016.1158717.

Garitte, B., Vaunat, J., Gens, A. & Armand, G. 3D Interpretation of an in situ heating test in the callovo-oxfordian mudstone. A: Clays in Natural & Engineered Barriers for Radioactive Waste Confinement. Clays in Natural & Engineered Barriers for Radioactive Waste Confinement. 4th. International Meeting. Nantes: 2010, p. 231–232.

Garitte B, Nguyen TS, Barnichon JD, Graupner BJ, Lee C, Maekawa K, Manepally C, Ofoegbu G, Dasgupta B, Fedors R, Pan PZ, Feng XT, Rutqvist J, Chen F, Birkholzer J, Wang Q, Kolditz O, Shao H (2017) Modelling the Mont Terri HE-D experiment for the thermal–hydraulic–mechanical response of a bedded argillaceous formation to heating, Environmental Earth Sciences, 76:354.

Gens A, Vaunat J, Garitte B, Wileveau Y. In situ behaviour of a stiff layered clay subject to thermal loading: observations and interpretation. *Geotechnique* 2007; 57(2):207–228.

Gens, A., Sanchez, M., Do, L., Guimaraes, N., Alonso, E.E., Lloret, A., Olivella, S., Villar, M.V. & Huertas, F. (2009). A full-scale in situ heating test for high-level nuclear waste disposal: observations, analysis and interpretation. Geotechnique 59, No. 4, 377–399, doi: 10.1680/geot.2009.59.4.377.

Gens, A. Underground research laboratories in nuclear waste containment. 2018. SEG.

Gischig, V. S., Doetsch, J., Maurer, H., Krietsch, H., Amann, F., Evans, K. F., ... & Wiemer, S. (2018). On the link between stress field and small-scale hydraulic fracture growth in anisotropic rock derived from microseismicity. Solid Earth, 9(1), 39-61, doi 10.3929/ethz-b-000238888.

Le Gonidec, Y., Sarout, J., Wassermann, J., Schubne, A., Gibert, D., Nussbaum, C., Kergosien, B., Maineult, A. & Guéguen, Y. (2014). Acoustic experiments: seismic survey and micro-seismicity. Nussbaum, C. & Bossart, P. Mont Terri Rock Laboratory: Geophysical investigation of the Excavation Damaged Zone during a mine-by experiment. [Online] Reports of the Swiss Geological Survey, 58–75.

Görke UJ, Park CH, Wang W, Singh A, Kolditz O (2011). Numerical simulation of multiphase hydrome-chanical processes induced by CO2 injection in deep saline aquifers. Oil Gas Sci Technol 48:1–15.

Grambow, B. (2016). Geological Disposal of Radioactive Waste in Clay. Elements. 12 (4): 239–245. https://doi.org/10.2113/gselements.12.4.239.

Grechka, V., Mazumdar, P., & Shapiro, S. A. (2010). Predicting permeability and gas production of hydraulically fractured tight sands from microseismic data. Geophysics, 75(1), B1–B10, https://doi.org/10.1190/1.3278724.

Guéguen, Y. & Sarout, J., 2011. Characteristics of anisotropy and dispersion in cracked medium. *Tectonophysics*, **503**, 165–172.

Guilbot, J. & Smith, B., 2002. 4-D constrained depth conversion for reservoir compaction estimation: Application to Ekofisk Field. The Leading Edge, 21, 302–308.

Guo, L., Latham, J. P., & Xiang, J. (2017). A numerical study of fracture spacing and through-going fracture formation in layered rocks. International Journal of Solids and Structures, 110, 44–57, ISSN 0020-7683, https://doi.org/10.1016/j.ijsolstr.2017.02.004.

Haas A. & Dubrule O. (1994). Geostatistical inversion - a sequential method of stochastic reservoir modelling constrained by seismic dataNormal access. First Break, 12(11), 561–569. 10.3997/1365-2397.1994034.

Hall, S., Kendall, J.M., Maddock, L. & Fisher, Q.J. (2008). Crack density tensor inversion for analysis of changes in rock frame architecture. *Geophysical Journal International*, **173**, 577–592.

Hamdi, P., Stead, D. & Elmo, D. (2014). Damage characterization during laboratory strength testing: A 3D-finite-discrete element approach, Computers and Geotechnics, Volume 60, Pages 33–46, ISSN 0266-352X, https://doi.org/10.1016/j.compgeo.2014.03.011.

Hanks, T.C., & Kanamori, H. (1979). A moment magnitude scale. Journal of Geophysical Research,84, 2348–2350.

Hantschel, T. & Kauerauf, A.I. 2009. Fundamentals of Basin and Petroleum Systems Modeling. Springer, Berlin, Heidelberg.

Hardebeck J.L. & Aron A. (2009). Earthquake Stress Drops and Inferred Fault Strength on the Hayward Fault, East San Francisco Bay, California. Bulletin of the Seismological Society of America ; 99 (3): 1801–1814. doi: https://doi.org/10.1785/0120080242.

Hart, R., P.A. Cundall, J. Lemos. (1988). Formulation of a three-dimensional distinct element modelâ€"Part II. Mechanical calculations for motion and interaction of a system composed of many polyhedral blocks. International Journal of Rock Mechanics and Mining Sciences & Geomechanics Abstracts, 25(3), 117–125, ISSN 0148-9062, https://doi.org/10.1016/0148-9062(88)92294-2.

Hartmann, A., Wagener, T., Rimmer, A., Lange, J., Brielmann, H., & Weiler, M. (2013). Testing the realism of model structures to identify karst system processes using water quality and quantity signatures. *Water Resour. Res.*, **49**, 3345–3358, doi:10.1002/wrcr.20229.

Hawkins, K. (2008). Defining the extent of the compacting Elgin reservoir by measuring stress-induced anisotropy. First Break, 26(10). 6.

Hazzard, J. F., & Young, R. P. (2002). Moment tensors and micromechanical models. Tectonophysics, 356(1-3), 181–197, ISSN 0040-1951, https://doi.org/10.1016/S0040-1951(02)00384-0.

He, Y.X., Angus, D.A., Clark, R.A., & Hildyard, M.W. (2015). Analysis of time-lapse travel-time and amplitude changes to assess reservoir compartmentalization. Geophysical Prospecting, 64(1), 54-67.

Hertzsch, J. M., & Gräsle, W. (2015). Dependency of the Elastic Modulus of Opalinus Clay on the Confining Pressure. In Second EAGE Workshop on Geomechanics and Energy (pp. cp-466). European Association of Geoscientists & Engineers.

Herwanger, J., Palmer, E. & Schiøtt, C.R. (2007). Anisotropic velocity changes in seismic time-lapse data. SEG Technical Program Expanded Abstracts, 2883-2887. 6.

Herwanger, J. & Horne, S.A. (2009). Linking reservoir geomechanics and time-lapse seismics: Predicting anisotropic velocity changes and seismic attributes. Geophysics, 74, W13-W33. xvii, 2, 7, 14, 17.

Herwanger, J. & Koutsabeloulis, N. (2011). Seismic Geomechanics: How to Build and Calibrate Geomechanical Models Using 3D and 4D Seismic Data. EAGE. 66, 93.

Hill, Mark & Marty, M.R.. (2008). Amdahl's Law in the Multicore Era. Computer. 41. 33 - 38. 10.1109/MC.2008.209.

Hoek, E. Tunnel support in weak rock. Keynote address, Symposium of Sedimentary Rock Engineering, Taipei, Taiwan, November 20-22, 1998.

Hoek, E. Chapter 2: Support for very weak rock associated with faults and shear zones. Edited By A.G. Thompson, Rock Support and Reinforcement Practice in Mining, 2018, London, Routledge, ISBN 9780203740460, https://doi.org/10.1201/9780203740460.

Hökmark, H., Lönnqvist, M. and Fälth, B. (2010). THM-issues in Repository Rock. Thermal, Mechanical, Thermo-Mechanical and Hydromechanical Evolution of the Rock at the Forsmark and Laxemar Sites. SKB TR-10-23, Svensk Kärnbränslehantering AB, Stockholm.

Hooman K. & Gurgenci H. (2007). Effects of temperature-dependent viscosity variation on entropy generation, heat and fluid flow through a porous-saturated duct of rectangular cross-section. Appl Math Mech (En Ed), 28 (1), pp. 69-78.

Huang, Y. H., Chang, C. C., Chiou, Y. F., Tseng, H. H., & Chang, S. J. (2018). Safety Assessment of the Fractured Crystalline Reference Case on the Spent Nuclear Fuel Disposal in Taiwan. In 2nd International Discrete Fracture Network Engineering Conference. American Rock Mechanics Association.

Hueckel T. & Baldi, G. (1990). Thermoplasticity of Saturated Clays: Experimental Constitutive Study. *Journal of Geotechnical Engineering*, **116**, 12. https://doi.org/10.1061/(ASCE)0733-9410(1990)116:12(1778).

Hueckel T. & Borsetto M. (1990). Thermoplasticity of Saturated Soils and Shales: Constitutive Equations. *Journal of Geotechnical Engineering*, **116**, 12. https://doi.org/10.1061/(ASCE)0733-9410(1990)116:12(1765).

Huang, K. P., Wang, T. T., Huang, T. H., & Jeng, F. S. (2010). Profile deformation of a circular tunnel induced by ambient stress changes. Tunnelling and underground space technology, 25(3), 266-278, ISSN 0886-7798, https://doi.org/10.1016/j.tust.2009.12.006.

Hudson, J.A., Tsang, C.-F. & Jing, L. Chapter 1 - Coupled THMC modeling for safety assessment of geological disposal of radioactive wastes: The DECOVALEX project (1992–2015), Edited By Xia-Ting Feng, Rock Mechanics and Engineering Volume 3, Analysis, Modeling & Design, 2017, London, CRC Press, ISBN 9781315708133, https://doi.org/10.1201/b20402.

International Atomic Energy Agency, 2011a. The Fukushima Daiichi Accident Technical Volume 4: Radiological Consequences.

International Atomic Energy Agency, 2011b. Geological disposal facilities for radioactive waste: specific safety guide. IAEA Safety Standards Series No. SSG-14.

Iooss B. & Lemaitre P. (2015) A Review on Global Sensitivity Analysis Methods. In: Dellino G., Meloni C. (eds) Uncertainty Management in Simulation-Optimization of Complex Systems. Operations Research/Computer Science Interfaces Series, vol 59. Springer, Boston, MA.

Iske, A. & Randen, T., 2006. Mathematical methods and modelling in hydrocarbon exploration and production. **7**, Springer Science & Business Media.

Jackson, C.P., Holton, D. & Myers, S. 2015. Project Ankhiale: Estimating the uplift due to high-heat-generating waste in a Geological Disposal Facility. Amec.

Jaeger, J.C., Cook, N.G.W. & Zimmerman, R. Fundamentals of Rock Mechanics, John Wiley, New York, 2007.

Jalali MR, Gischig V, Doetsch J, Krietsch H, Amann F and Klepikova M. Mechanical, hydraulic and seismological behavior of crystalline rock as a response to hydraulic fracturing at the Grimsel Test Site. *American Rock Mechanics Association*; 51st U.S. Rock Mechanics/Geomechanics Symposium, 25–28 June, San Francisco, California, USA.

Jing, L. & Hudson, J.A. (2002). Numerical methods in rock mechanics. International Journal of Rock Mechanics and Mining Sciences, Volume 39, Issue 4, Pages 409-427, ISSN 1365-1609, https://doi.org/10.1016/S1365-1609(02)00065-5.

Jing, L. (2003). A review of techniques, advances and outstanding issues in numerical modelling for rock mechanics and rock engineering. International Journal of Rock Mechanics and Mining Sciences, Volume 40, Issue 3, Pages 283-353, ISSN 1365-1609, https://doi.org/10.1016/S1365-1609(03)00013-3.

Jing, L. & Stephansson, O. (2007). Fundamentals of Discrete Element Methods for Rock Engineering: Theory and Applications. Elsevier Science, Volume 85, 1st Edition. ISBN: 9780444829375.

Jobmann M, Li S, Polster M, Breustedt M, Schlegel R, Vymlatil P & Will J. (2016). Using Statistical Methods for Rock Parameter Identification to Analyse the THM Behaviour of Callovo-oxfordian Claystone. *Journal of Geological Resource and Engineering*; 3:125–136.

Johannesson, L.E., Börgesson, L., Goudarzi, R., Sandén, T., Gunnarsson, D. & Svemar, C. (2007). Prototype repository: A full scale experiment at Äspö HRL. *Physics and Chemistry of the Earth*, Parts A/B/C, **32**, 1–7, pp.58–76.

Johnson, M.E., Moore, I.M., Ylvisaker, D. (1990). Minimax and maximin distance designs. J. Stat. Plan. Inference 26, 131–148.

(Joulin et al., 2017) Joulin C., Xiang J., Latham JP., Pain C. (2017) A New Finite Discrete Element Approach for Heat Transfer in Complex Shaped Multi Bodied Contact Problems. In: Li X., Feng Y., Mustoe G. (eds) Proceedings of the 7th International Conference on Discrete Element Methods. DEM 2016. Springer Proceedings in Physics, vol 188. Springer, Singapore.

Kasiri, N. & Bashiri, A., (2010). Comparative study of different techniques for numerical reservoir simulation. *Petroleum Science and Technology*, **28**(5), 494-503.

Kenney, J. P., Kirby, M. E., Cuadros, J., & Weiss, D. J. (2017). A conceptual model to predict uranium removal from aqueous solutions in waterâ€“rock systems associated with low-and intermediate-level radioactive waste disposal. RSC advances, 7(13), 7876–7884.

Keto, P., Dixon, D., Jonsson, E., Gunnarsson, D., Boergesson, L., & Hansen, J. (2009). Assessment of backfill design for KBS-3V repository. Sweden: N. p., Web.

Khazaei, C., Hazzard, J. & Chalaturnyk, R. Pure Appl. Geophys. (2016). Discrete Element Modeling of Stick-Slip Instability and Induced Microseismicity. 173: 775. https://doi.org/10.1007/s00024-015-1036-7.

Kirby ME, Simperler A, Krevor S, Weiss DJ, Sonnenberg JL. (2018). Computational Tools for Calculating log β Values of Geochemically Relevant Uranium Organometallic Complexes. J Phys Chem A. doi: 10.1021/acs.jpca.8b06863. [Epub ahead of print].

Kolditz, O. (1995). Modelling flow and heat transfer in fractured rocks: conceptual model of a 3-d deterministic fracture network. Geothermics 24(3):451–470.

Korneev, V. & Glubokovskikh, S. (2013). Seismic velocity changes caused by an overburden stress. *Geophysics*, **78**(5), 25-31.

Kozak, M.W. (2017). 16 - Safety assessment for near-surface disposal of low and intermediate level wastes, Editor(s): Michael J. Apted, Joonhong Ahn, In Woodhead Publishing Series in Energy, Geological Repository Systems for Safe Disposal of Spent Nuclear Fuels and Radioactive Waste (Second Edition), Woodhead

Publishing, Pages 475-498, ISBN 9780081006429, https://doi.org/10.1016/B978-0-08-100642-9.00016-5.

Kozeny, J. (1927). Uber kapillare leitung des wassers im boden: Sitzungsber. Royal Academy of Science, 136, 271-306. 23.

Kull H, Jockwer N, Zhang CL, Wileveau Y and Pepa S (2005). Measurement of Thermally-Induced Pore-water Pressure and Gas Migration in the Opalinus clay at Mont Terri - HE-D heating Experiment. 2nd International Meeting of Clays in Natural and Engineered Barriers for Radioactive Waste Confinement, Tours, March 14–18.

Lang P, Paluszny Rodriguez A, Morteza N, Zimmerman R. et al. (2018), Relationship between the orientation of maximum permeability and intermediate principal stress in fractured rocks, Water Resources Research, Vol: 54, Pages: 8734-8755, ISSN: 0043-1397.

Lanyon, G.W. & Gaus, I. (2016). Main outcomes and review of the FEBEX In Situ Test (GTS) and Mock-up after 15 years of operation. Technical Report 15-04 Grimsel Test Site Investigation Phase VI March 2016. Nagra.

Latha, G. M., & Garaga, A. (2012). Elasto-plastic analysis of jointed rocks using discrete continuum and equivalent continuum approaches. International Journal of Rock Mechanics and Mining Sciences, 53, 56–63, https://doi.org/10.1016/j.ijrmms.2012.03.013.

Latham, J. P., Anastasaki, E., & Xiang, J. (2013). New modelling and analysis methods for concrete armour unit systems using FEMDEM. Coastal Engineering, 77, 151–166, https://doi.org/10.1016/j.coastaleng.2013.03.001.

Lever, D.A., Berry, J.A., Hoch, A.R., Holton, D., Kelly, M. and Marshall, T.A. (2011). The Treatment of Geosphere Evolution in Post-Closure Performance Assessments. Serco Report SERCO/TAS/002783/001 Issue 4 for the NDA RWMD. Serco, Harwell.

Li, X. L., Bastiaens, W., Van Marcke, P., Verstricht, J., Chen, G. J., Weetjens, E., & Sillen, X. (2010). Design and development of large-scale in-situ PRACLAY heater test and horizontal high-level radioactive waste disposal gallery seal test in Belgian HADES. Journal of Rock Mechanics and Geotechnical Engineering, 2(2), 103–110, ISSN 1674-7755, https://doi.org/10.3724/SP.J.1235.2010.00103.

Li, X. (2013). TIMODAZ: A successful international cooperation project to investigate the thermal impact on the EDZ around a radioactive waste disposal in clay host rocks, *Journal of Rock Mechanics and Geotechnical Engineering*, **5**(3), 231–242, ISSN 1674–7755, https://doi.org/10.1016/j.jrmge.2013.05.003.

Li, Y., Vardon, P.J., Hicks, M.A., Hart J. & Fokker, P.A. Technical feasibility of a Dutch radioactive waste repository in Boom Clay: Geomechanical validation. July 2018. OPERA-PU-TUD321d.

Lisjak, A., Garitte, B., Grasselli, G., Müller, H.R. & Vietor, T. (2015). The excavation of a circular tunnel in a bedded argillaceous rock (Opalinus Clay): Short-term rock mass response and FDEM numerical analysis, Tunnelling and Underground Space Technology, Volume 45, Pages 227-248, ISSN 0886-7798, https://doi.org/10.1016/j.tust.2014.09.014.

Lisjak, A., Tatone, B.S., Mahabadi, O.K., Grasselli, G., Marschall, P., Lanyon, G.W., de la Vaissière, R., Shao, H., Leung, H. & Nussbaum, C. (2016). Hybrid finite-discrete element simulation of the EDZ formation and mechanical sealing process around a microtunnel in Opalinus Clay. Rock Mechanics and Rock Engineering, 49(5), 1849–1873.

Liu, Y., Alessi, D. S., Owttrim, G. W., Kenney, J. P. L., Zhou, Q., Lalonde, S. V., & Konhauser, K. O. (2016). Cell surface acid-base properties of the cyanobacterium Synechococcus: Influences of nitrogen source, growth phase and N: P ratios. Geochimica et Cosmochimica Acta, 187, 179–194, ISSN 0016-7037, https://doi.org/10.1016/j.gca.2016.05.023.

Liu, H., Yuan, F., Jiang, Y., Zhao, M., Chen, K., Guo, Z., & Wang, Y. (2019). Mechanisms for overpressure generated by the undercompaction of paleogene strata in the Baxian Depression of Bohai Bay Basin, China. Marine and Petroleum Geology, 99, 337–346, ISSN 0264-8172, https://doi.org/10.1016/j.marpetgeo.2018.10.001.

Lockner, D. (1993). The role of acoustic emission in the study of rock fracture. International Journal of Rock Mechanics and Mining Sciences & Geomechanics Abstracts, Volue 30, Issue 7, Pages 883-899, https://doi.org/10.1016/0148-9062(93)90041-B.

Lorig, L.J., & Brady, B.H.G. (1982). A Hybrid Discrete Element-Boundary Element Method Of Stress Analysis. American Rock Mechanics Association. The 23rd U.S Symposium on Rock Mechanics (USRMS), 25–27 August, Berkeley, California.

Ma, T. H., Tang, C. A., Tang, S. B., Kuang, L., Yu, Q., Kong, D. Q., & Zhu, X. (2018). Rockburst mechanism and prediction based on microseismic monitoring. International Journal of Rock Mechanics and Mining Sciences, 110, 177-188, https://doi.org/10.1016/j.ijrmms.2018.07.016.

Mack, C.A. (2011). Fifty Years of Moore's Law, in IEEE Transactions on Semiconductor Manufacturing, vol. 24, no. 2, pp. 202–207. doi: 10.1109/TSM.2010.2096437.

Martin, C. D. & Lanyon, G. W. (2003). Measurement of in-situ stress in weak rocks at Mont Terri Rock Laboratory, Switzerland. International Journal of Rock Mechanics & Mining Sciences, 40, 1077–1088.

Martinez-Landa, L., and Carrera, J. (2005), An analysis of hydraulic conductivity scale effects in granite (Full-scale Engineered Barrier Experiment (FEBEX), Grimsel, Switzerland), Water Resour. Res., 41, W03006, doi:10.1029/2004WR003458.

Marschall, P., Horseman, S. & Gimmi, T. (2005). Characterisation of Gas Transport Properties of the Opalinus Clay, a Potential Host Rock Formation for Radioactive Waste Disposal. Oil & Gas Science and Technology - Rev. IFP, 60 1, 121-139. DOI: https://doi.org/10.2516/ogst:2005008.

Matthew A.P. & Diederichs M.S. (2014). A Review of the Tensile Strength of Rock: Concepts and Testing. Geotech Geol Eng, Vol:32, Pages:525–546. DOI 10.1007/s10706-014-9732-0.

Maxwell, S.C., Rutledge, J., Jones, R. & Fehler, M. (2010), Petroleum reservoir characterization using downhole microseismic monitoring, GEOPHYSICS 75: 75A129-75A137. https://doi.org/10.1190/1.3477966.

Mayerhofer, M. J., Lolon, E. P., Youngblood, J. E., & Heinze, J. R. (2006). Integration of Microseismic-Fracture-Mapping Results With Numerical Fracture Network Production Modeling in the Barnett Shale. Society of Petroleum Engineers. doi:10.2118/102103-MS.

McGarr, A., & Gay, N.C. (1978). State of stress in the Earth's crust, Annu. Rev. Earth Planet. Sci., 6, 558–562.

McGuire, J. & Kaneko, Y. (2018). Directly estimating earthquake rupture area using second moments to reduce the uncertainty in stress drop, Geophysical Journal International, Volume 214, Issue 3, Pages 2224–2235, https://doi.org/10.1093/gji/ggy201.

McKay, M.D., Beckman, R.J. & Conover, W.J. (1979). A Comparison of Three Methods for Selecting Values of Input Variables in the Analysis of Output from a Computer Code. Technometrics 21(2):239-245.

McTigue, D.F. (1986). Thermoelastic response of fluid-saturated porous rock, *J. Geophys. Res.*, **91**, 9, 9533–9542, doi:10.1029/JB091iB09p09533.

Menaceur H, Delage P, Tang A & Conil N. (2015). The thermo-mechanical behaviour of the Callovo-Oxfordian claystone. *International Journal of Rock Mechanics and Mining Sciences*; 78:290–303.

Menaceur, H., Delage, P., Tang, A.M.& Conil, N. (2016). On the Thermo-Hydro-Mechanical Behaviour of a Sheared Callovo-Oxfordian Claystone Sample with Respect to the EDZ Behaviour. *Rock Mech Rock Eng*, **49**, 1875. https://doi.org/10.1007/s00603-015-0897-5.

Mohajerani, M., Delage, P., Sulem, J., Monfared, M., Tang, A.M. & Gatmiri, B. (2012). A laboratory investigation of thermally induced pore pressures in the Callovo-Oxfordian claystone, International Journal of Rock Mechanics and Mining Sciences, Volume 52, Pages 112-121, ISSN 1365-1609, https://doi.org/10.1016/j.ijrmms.2012.02.012.

Mohajerani, M., Delage, P., Sulem, J., Monfared, M., Tang, A.M. & Gatmiri, B. (2014). The Thermal Volume Changes of the Callovo-Oxfordian Claystone. *Rock Mech Rock Eng*, **47**, 131. https://doi.org/10.1007/s00603-013-0369-8

Mohamedelhassan, E. & Shang, J.Q. (2002). Vacuum and surcharge combined one-dimensional consolidation of clay soils. Canadian Geotechnical Journal, 39(5): 1126-1138, https://doi.org/10.1139/t02-052.

Monfared, M., Sulem, J., Delage, P. & Mohajerani, M. (2011). A Laboratory Investigation on Thermal Properties of the Opalinus Claystone. *Rock Mech Rock Eng*, **44**, 735. https://doi.org/10.1007/s00603-011-0171-4

Möri, A., Alexander, W.R., Geckeis, H., Hauser, W., Schäfer, T., Eikenberg, J., Fierz, Th., Degueldre, C. & Missana, T. (2003). The colloid and radionuclide retardation experiment at the Grimsel Test Site: influence of bentonite colloids on radionuclide migration in a fractured rock. Colloids and Surfaces A: Physicochemical and Engineering Aspects, Volume 217, Issues 1–3, Pages 33-47, ISSN 0927-7757, https://doi.org/10.1016/S0927-7757(02)00556-3.

Morris MD & Mitchell TJ. (1995). Exploratory designs for computer experiments. *Journal of Statistical Planning and Inference*; 43:381–402.

Mosser, L., Dubrule, O. & Blunt, M.J. (2017). Reconstruction of three-dimensional porous media using generative adversarial neural networks. Phys. Rev. E 96, 043309.

Mosser, L., Le Blévec, T. & Dubrule, O. (2018). Chapter 8: Reconstruction of Three-Dimensional Porous Media: Statistical or Deep Learning Approach? Statistical Data Science, pp. 125–139. https://doi.org/10.1142/9781786345400 0008.

C. Mugler, Filippi, M., Montarnal, Ph., Martinez, J.-M. & Wileveau, Y. (2006). Determination of the thermal conductivity of opalinus clay via simulations of experiments performed at the Mont Terri underground laboratory. *Journal of Applied Geophysics*; **58**(112–129).

Müller, T. M., & Sahay, P. N. (2016). Biot coefficient is distinct from effective pressure coefficient. *Geophysics*, **81**(4), 27–33.

Müller, H.R., Garitte, B., Vogt, T., Köhler, S., Sakaki, T., Weber, H., Spillmann, T., Hertrich, M., Becker, J.K., Giroud, N., Cloet, V., Diomidis, N. & Vietor, T. (2018). Implementation of the full-scale emplacement (FE) experiment at the Mont Terri rock laboratory. In: Bossart P., Milnes A. (eds) Mont Terri Rock Laboratory, 20 Years. Swiss Journal of Geosciences Supplement, vol 5. Birkhäuser, Cham.

Munjiza, A. (2004). The combined finite-discrete element method, Chichester: John Wiley.

Nagel, N.B. (2001). Compaction and subsidence issues within the petroleum industry: From wilmington to ekofisk and beyond, Physics and Chemistry of the Earth, Part A: Solid Earth and Geodesy, Volume 26, Issues 1–2, Pages 3-14, ISSN 1464-1895, https://doi.org/10.1016/S1464-1895(01)00015-1.

Nagra, 2002. Project Opalinus Clay - Safety Report: Demonstration of disposal feasibility for spent fuel, vitrified high-level waste and long-lived intermediate-level waste. Nagra Technical Report 02-05.

National Decommissioning Authority. 2010a. Geological Disposal: An overview of the generic Disposal System Safety Case. NDA/RWMD/010.

National Decommissioning Authority. 2010b. Geological Disposal: Geosphere Status Report. Nuclear Decommissioning Authority Report NDA/RWMD/035, Harwell.

Neuner, M.; Cordes, T.; Drexel, M.; Hofstetter, G. (2017). Time-Dependent Material Properties of Shotcrete: Experimental and Numerical Study. Materials, 10, 1067. https://doi.org/10.3390/ma10091067.

Nguyen, T.S., Selvadurai, A.P.S. & Armand, G. (2005). Modelling the FEBEX THM experiment using a state surface approach, International Journal of Rock Mechanics and Mining Sciences, Volume 42, Issues 5–6, Pages 639-651, ISSN 1365-1609, https://doi.org/10.1016/j.ijrmms.2005.03.005.

Nirex, 2002. Radioactive Wastes in the UK: A Summary of the 2001 Inventory. DEFRA/RAS/02.003, Nirex Report N/041, October 2002.

Noorishad J. & Tsang C.-F. (1996). ROCMAS simulator; A thermohydromechanical computer code. O. Stephansson, L. Jing, C.-F. Tsang (Eds.), Coupled thermo-hydro- mechanical processes of fractured media, Elsevier (1996), pp. 551-558.

Norris S., Bruno J., Van Geet M. & Verhoef E. (eds) Radioactive Waste Confinement: Clays in Natural and Engineered Barriers. Geological Society, London, Special Publications, 443, https://doi.org/10.1144/SP443.26. 2017 The Author(s). Published by The Geological Society of London.

Norton, J. (2015). An introduction to sensitivity assessment of simulation models, Environmental Modelling & Software, Volume 69, Pages 166-174, ISSN 1364-8152, https://doi.org/10.1016/j.envsoft.2015.03.020.

Nossent J, Elsen P & Bauwens W. (2011). Sobol' sensitivity analysis of a complex environmental model. *Environmental Modelling Software*; 26(12):1515–1525.

Nowak T, Kunz H, Dixon D, Wang W, Görke UJ, Kolditz O (2011). Coupled 3-D thermo-hydro-mechanical analysis of geotechnical in situ tests. International Journal of Rock Mechanics and Mining Sciences, 48(1):1–15.

Nuclear Energy Agency & Radioactive Waste Management Committee. 2010. Survey on Long-term Preservation of Information and Memory for Geological Disposal of Radioactive Waste. Organisation for Economic Co-operation and Development, 2011, 7/REV.

Nussbaum, C., Graf, A. & Bossart, P. 2004a. Structural and geological mapping of the HE-D niche: results and discussion, HE-D Experiment, Technical Note 2004-07.

Nussbaum, C., Badertscher, N., Graf, A., Steiger, H., Meier, O., Bossart,P. 2004b. Drilling Campaigns of Phases 9a and 9b, Drilling and field Mapping of Drillcores including Photo Documentation - Part 2, Technical Note 2004-06.

C.Nussbaum, C. Girardin, N.Badertscher. 2014. Geological characterisation of the investigated rock mass. Nussbaum, C. & Bossart, P. Mont Terri Rock Laboratory: Geophysical investigation of the Excavation Damaged Zone during a mine-by experiment. [Online] Reports of the Swiss Geological Survey, 30–44.

Nygard, R., Gutierrez, M., Gautam, R & Hoeg, K. (2004a). Compaction behavior of argillaceous sediments as function of diagenesis. *Marine and Petroleum Geology*, **21**, 3, 349–362, ISSN 0264-8172, https://doi.org/10.1016/j.marpetgeo.2004.01.002.

Nygard, R., Gutierrez, M., Hoeg, K. & Bjorlykke, K. (2004b). Influence of burial history on microstructure and compaction behaviour of Kimmeridge clay. *Petroleum Geoscience*, **10**, 3, 259–270, https://doi.org/10.1144/1354-079303-591.

Ofoegbu, G. I., Dasgupta, B., Manepally, C., Stothoff, S. A., & Fedors, R. (2019). To be Submitted to International Journal of Rock Mechanics and Mining Sciences.

Onajite, E. (2013). Seismic data analysis techniques in hydrocarbon exploration. Elsevier.

optiSLang. The Optimizing Structural Language Version 3.1.4, optiSLang Documentation. Dynardo GmbH, Weimar 2010. http://www.dynardo.de.

Organization for Economic Co-operation and Development, 1995. The Environmental and Ethical Basis of Geological Disposal of Long-Lived Radioactive Wastes, a Collective Opinion of the Radioactive Waste Management Committee of the OECD Nuclear Energy Agency.

Osborne, M.J. & Swarbrick, R.E. (1997). Mechanisms for Generating Overpressure in Sedimentary Basins: A Reevaluation. AAPG Bulletin.

Ougier-Simonin, A., Sarout, J. & Guéguen, Y. (2009). A simplified model of effective elasticity for anisotropic shales. *Geophysics*, **74**, 57-63.

Paraskevopoulou, C. & Diederichs, M. (2018). Analysis of time-dependent deformation in tunnels using the Convergence-Confinement Method. *Tunnelling and Underground Space Technology*, **71**, 62–80, ISSN 0886-7798, https://doi.org/10.1016/j.tust.2017.07.001.

Paszyński, M., Pardo, D. & Paszyńska, A. (2010). Parallel multi-frontal solver for p adaptive finite element modeling of multi-physics computational problems. Journal of Computational Science, Volume 1, Issue 1, 2010, Pages 48-54, ISSN 1877-7503, https://doi.org/10.1016/j.jocs.2010.03.002.

Patterson, R., Yu, W. & Wu, K. (2018). Integration of microseismic data, completion data, and production data to characterize fracture geometry in the Permian Basin, Journal of Natural Gas Science and Engineering, Volume 56, Pages 62-71, ISSN 1875-5100, https://doi.org/10.1016/j.jngse.2018.05.025.

Petropoulos G and Srivastava PK (2016). Sensitivity Analysis in Earth Observation Modelling. Elsevier Science & Technology Books.

Pettersson, S. & Lönnerberg, B. (2008). Final Repository For Spent Nuclear Fuel In Granite - The KBS-3V Concept In Sweden And Finland. International Conference: Underground Disposal Unit Design & Emplacement Processes for a Deep Geological Repository. 16–18 June 2008, Prague.

Pianosi F, Sarrazin F and Wagener T. (2015). A Matlab toolbox for Global Sensitivity Analysis. *Environmental Modelling & Software*; 70:80–85.

Pianosi, F., Beven, K., Freer, J., Hall, J. W., Rougier, J., Stephenson, D. B., & Wagener, T. (2016). Sensitivity analysis of environmental models: A systematic review with practical workflow. Environmental Modelling & Software, 79, 214–232, ISSN 1364-8152, https://doi.org/10.1016/j.envsoft.2016.02.008.

Plötze, M., Kahr, G., Dohrmann, R. & Weber, H. (2007). Hydro-mechanical, geochemical and mineralogical characteristics of the bentonite buffer in a heater experiment: the HE-B project at the Mont Terri Rock Laboratory. Physics and Chemistry of the Earth, 32, 730–740.

Price, D., Angus, D., Garcia, A., Fisher, Q., Parsons, S. & Kato, J. (2017). A multimethod Global Sensitivity Analysis to aid the calibration of geomechanical models via time-lapse seismic data. Geophysical Journal International. 212. 10.1093/gji/ggx516.

Prioul, R., Bakulin, A. & Bakulin, V. (2004). Nonlinear rock physics model for estimation of 3D subsurface stress in anisotropic formations. *Geophysics*, **69**, 415-425.

Profit, M., Dutko, M., Yu, J., Cole, S., Angus, D. & Baird, A. (2016). Complementary hydro-mechanical coupled finite/discrete element and microseismic modelling to predict hydraulic fracture propagation in tight shale reservoirs. Comp. Part. Mech. 3: 229. https://doi.org/10.1007/s40571-015-0081-4.

Qi, C. & Fourie, A. (2018). A Real-Time Back-Analysis Technique to Infer Rheological Parameters from Field Monitoring. Rock Mechanics and Rock Engineering, 51(10), 3029–3043, 10.1007/s00603-018-1513-2.

Ravichandran, N. (2009). Fully coupled finite element model for dynamics of partially saturated soils, Soil Dynamics and Earthquake Engineering, Volume 29, Issue 9, Pages 1294-1304, ISSN 0267-7261, https://doi.org/10.1016/j.soildyn.2009.03.002.

Revil, A., Leroy, P. & Titov, K. (2005). Characterization of transport properties of argillaceous sediments: application to the Callovo-Oxfordian argillite. Journal of Geophysical Research, 110, B06202, doi:10.1029/2004JB003442.

Rockfield Software Limited, 2012. ELFEN GeoDB Generic Materials. Swansea. xviii,

Rockfield Software Limited, 2013a. ELFEN Explicit Manual. Version 4.7.1. Rockfield Software Limited.

Rockfield Software Limited, 2013b. ELFEN Implicit Manual. Version 4.7.1. Rockfield Software Limited.

Romero, E., Gens, A. & Lloret, A. (1999). Water permeability, water retention and microstructure of unsaturated compacted Boom clay, Engineering Geology, Volume 54, Issues 1–2, Pages 117-127, ISSN 0013-7952, https://doi.org/10.1016/S0013-7952(99)00067-8.

Roscoe K.H. & Burland J.B. (1968). On the generalised stress-strain behaviour of ‘wet’ clay, Eng. plasticity, Cambridge Univ. Press, 535-609.

Ross, P.E. (2003). 5 Commandments [technology laws and rules of thumb], in IEEE Spectrum, vol. 40, no. 12, pp. 30–35. doi: 10.1109/MSPEC.2003.1249976.

Rutqvist, J., Wu, Y.-S., Tsang, C.-F. & Bodvarsson, G. (2002). A modeling approach for analysis of coupled multiphase fluid flow, heat transfer, and deformation in fractured porous rock. *International Journal of Rock Mechanics and Mining Sciences*, **39**, 4, 429–442, ISSN 1365-1609, https://doi.org/10.1016/S1365-1609(02)00022-9.

Rutqvist, J. & Tsang, C.-F. (2004). A Fully Coupled Three-Dimensional THM Analysis of the Febex in Situ Test with the Rocmas Code: Prediction of THM Behavior in a Bentonite Barrier, Editor(s): Ove Stephanson, Elsevier Geo-Engineering Book Series, Elsevier, Volume 2, Pages 143-148, ISSN 1571-9960, ISBN 9780080445250, https://doi.org/10.1016/S1571-9960(04)80032-6.

Radioactive Waste Management, 2016a. Geological Disposal: Generic Disposal Facility Design. NDA Report no. DSSC/412/01.

Radioactive Waste Management, 2016b. Geological Disposal Technical Background to the generic Disposal System Safety Case. NDA Report no. DSSC/421/01.

Radioactive Waste Management, 2016c. Geological Disposal Part B: Technical Specification NDA Report no. DSSC/402/01 Generic Disposal System Specification.

Salimzadeh, S., Usui, T., Paluszny, A., & Zimmerman, R. W. (2017). Finite element simulations of interactions between multiple hydraulic fractures in a poroelastic rock. International Journal of Rock Mechanics and Mining Sciences, 99, 9–20, ISSN 1365-1609, https://doi.org/10.1016/j.ijrmms.2017.09.001.

Saltelli A, Ratto M, Andres T, Campolongo F, Cariboni J, Gatelli D, Saisana M & Tarantola S. Global Sensitivity Analysis. The Primer, John Wiley and Sons, 2008.

Saltelli, A., Stark, P.B., Becker, W. & Stano, P. (2013). Climate models as economic guides -scientific challenge of quixotic quest? Issues Sci. Technol. 31 (3), 1–8.

Saltelli, A., Aleksankina, K., Becker, W., Fennell, P., Ferretti, F., Holst, N., Li, S. & Wu, Q. (2019). Why so many published sensitivity analyses are false: A systematic review of sensitivity analysis practices. Environmental modelling & software, 114, 29-39, ISSN 1364-8152, https://doi.org/10.1016/j.envsoft.2019.01.012.

Sarout, J. & Guéguen, Y. (2008). Anisotropy of elastic wave velocities in deformed shales: Part 2 - Modelling results. *Geophysics*, **73**, 91-103.

Sarout, J., Le Gonidec, Y., Ougier-Simonin, A., Schubnel, A., Guéguen, Y. & Dewhurst, D.N. (2017). Laboratory micro-seismic signature of shear faulting and fault slip in shale, Physics of the Earth and Planetary Interiors, Volume 264, 47–62, ISSN 0031-9201, https://doi.org/10.1016/j.pepi.2016.11.005.

Sarrazin F, Pianosi F & Wagener T. (2016). Global Sensitivity Analysis of environmental models: Convergence and validation. *Environmental Modelling & Software*; 79:135–152.

Sayers, C.M. (2002). Stress-dependent elastic anisotropy of sandstones. *Geophysical Prospecting*, **50**, 85-95.

Schleicher, A.M., van der Pluijm, B.A. & Warr, L.N. (2010). Nanocoatings of clay and creep of the San Andreas fault at Parkfield, California. Geology; 38 (7): 667–670. doi: https://doi.org/10.1130/G31091.1.

Schuster K., Amann F., Yong S., Bossart P., Connolly P. (2018) High-resolution mini-seismic methods applied in the Mont Terri rock laboratory (Switzerland). In: Bossart P., Milnes A. (eds) Mont Terri Rock Laboratory, 20 Years. Swiss Journal of Geosciences Supplement, vol 5. Birkhäuser, Cham.

Sellin, P., & Leupin, O.X. (2013). The use of clay as an engineered barrier in radioactive-waste management-a review. Clays and Clay Minerals, 61(6), 477-498.

Settari, A. & Walters, D.A. (2001). Advances in coupled geomechanical and reservoir modeling with applications to reservoir compaction. Spe Journal, 6(3), 334-342. 14.

Settari, A. & Sen, V. (2007). The role of geomechanics in integrated reservoir modeling. *The Leading Edge*, **26**, 5, 545–672, https://doi.org/10.1190/1.2737102.

Seyedi, D., Vitel, M., Vu, M. N., & Armand, G. (2018). Key parameters controlling thermo-hydro-mechanical pressurization in Callovoâ€“Oxfordian claystone. In International symposium on energy geotechnics (SEG-2018), Lausanne, Switzerland, 10.13140/RG.2.2.27195.05926.

Shapiro, S. & Kaselow, A. (2005). Porosity and elastic anisotropy of rocks under tectonic stress and pore-pressure changes. *Geophysics*, **70**(5), N27-N38.

Shearer, P. M., Prieto, G. & Hauksson, E. (2006), Comprehensive analysis of earthquake source spectra in southern California, J. Geophys. Res.,doi:10.1029/2005JB003979, in press.

Shearer, P. M. (2019). Introduction to seismology, Cambridge University Press, Cambridge, England, 1–189.

Shirazi, S. M., Kazama, H., Salman, F.A., Othman, F. & Akib, S. (2010). Permeability and swelling characteristics of bentonite. *International Journal of the Physical Sciences*; **5**(11), 1647–1659.

Sibson, R. H. (2000). Fluid involvement in normal faulting. Journal of Geodynamics 29(3): 469-499.

Siegesmund, S., Sousa, L. & Knell, C. (2018). Thermal expansion of granitoids. Environmental Earth Sciences, 77:41. https://doi.org/10.1007/s12665-017-7119-2.

Sillen X. & Weetjens E. The source term and the geometry of the PRACLAY heater test, European Underground Research Infrastructure for Disposal of Nuclear Waste in Clay Environment (EURIDICE), Mol (2004).

Silver, P.G. & Jordan, T.H. (1982). Optimal estimation of scalar seismic moment. *Geophysical Journal International*, **70**, 3, 755–787, https://doi.org/10.1111/j.1365-246X.1982.tb05982.x.

Sin, G., Gernaey, K.V., Neumann, M.B., van Loosdrecht, M.C.M. & Gujer, W. (2011). Global sensitivity analysis in wastewater treatment plant model applications: Prioritizing sources of uncertainty. *Water Research*, **45**, 2, 639–651, ISSN 0043-1354, https://doi.org/10.1016/j.watres.2010.08.025.

Singh, R., Wagener, T., Crane, R., Mann, M. E., & Ning, L. (2014). A vulnerability driven approach to identify adverse climate and land use change combinations for critical hydrologic indicator thresholds: Application to a watershed in Pennsylvania, USA. *Water Resour. Res.*, **50**, 3409–3427, doi:10.1002/2013WR014988.

Sobol I. (1990). Sensitivity estimates for nonlinear mathematical models. *Matematicheskoe Modelirovanie*; 2:112–118 in Russian. *Mathematical Modeling and Computational Experiment (Engl. Transl.)* 1993; 1:407–414.

Song, X., Zhang, J., Zhan, C., Xuan, Y., Ye, M., & Xu, C. (2015). Global sensitivity analysis in hydrological modeling: Review of concepts, methods, theoretical framework, and applications. Journal of hydrology, 523, 739–757, ISSN 0022-1694, https://doi.org/10.1016/j.jhydrol.2015.02.013.

Spang, R.M. (2002). Certification of rockfall barriers in Europe. Better Highways Through Applied Geology. 53rd Annual Highway Geology Symposium. California. ISSN 00962012.

Spear R & Hornberger G. (1980). Eutrophication in peel inlet II. Identification of critical uncertainties via generalized sensitivity analysis. *Water Research*; 14(1):43–49.

Stavrou A & Murphy W. (2018). Quantifying the effects of scale and heterogeneity on the confined strength of micro-defected rocks. International Journal of Rock Mechanics and Mining Sciences. 102, pp. 131–143.

Stenhouse, M.J. & Savage, D. (2004). Monitoring experience associated with nuclear waste disposal and its application to CO2 sequestration projects. Geological Society, London, Special Publications, 233, 235–247, https://doi.org/10.1144/GSL.SP.2004.233.01.16.

Stephansson, O., Hudson, J. & Jing, L. (2004). Coupled Thermo-Hydro-Mechanical-Chemical Processes in Geo-systems. Elsevier Geo-Engineering Book Series Volume 2.

Tang Y, Reed P, Wagener T & Van Werkhoven K. (2007). Comparing sensitivity analysis methods to advance lumped watershed model identification and evaluation. *Hydrology and Earth System Sciences*; 11:793–817.

Terzaghi, K. Theoretical Soil Mechanics, Wiley, New York, 1943.

Thomas, H. R., Vardon, P. J. & Cleall, P. J. (2014). Three-dimensional behaviour of a prototype radioactive waste repository in fractured granitic rock. Canadian Geotechnical Journal 51(3), pp. 246-259. (10.1139/cgj-2013-0094).

Thomas RN, Paluszny A & Zimmerman RW (2017). Quantification of Fracture Interaction Using Stress Intensity Factor Variation Maps, Journal of Geophysical Research-solid Earth, Vol:122, ISSN:2169-9313, Pages:7698-7717.

Thomas RN, Paluszny A, Hambley D, et al. (2018). Permeability of observed three dimensional fracture networks in spent fuel pins, Journal of Nuclear Materials, Vol:510, ISSN:0022-3115, Pages:613-622.

Thornton, D. A. & Crook, A. J. L. (2014). Predictive Modeling of the Evolution of Fault Structure: 3-D Modeling and Coupled Geomechanical/Flow Simulation. Rock Mechanics and Rock Engineering, 47(5), 1533–1549, DOI: 10.1007/s00603-014-0589-6.

Thury, M. & Bossart, P. (1999). The Mont Terri rock laboratory, a new international research project in a Mesozoic shale formation, in Switzerland. Engineering Geology, 52, 347–359.

Titarenko S. & Hildyard M. (2017). Hybrid Multicore/vectorisation technique applied to the elastic wave equation on a staggered grid. Computer Physics Communications. 216, pp. 53-62.

Tod, S.R. (2002). The effects of stress and fluid pressure on the anisotropy of interconnected cracks. *Geophysical Journal International*, **70**(5), N27-N38.

Towler et al., 2008. Quintessa. Post-closure performance assessment: Example approaches for groundwater modelling of generic environments.

Tripathy, S., Sridharan, A., & Schanz, T. (2004). Swelling pressures of compacted bentonites from diffuse double layer theory. Canadian Geotechnical Journal, 41(3), 437-450.

Vanuytrecht, E., Raes, D. & Willems, P. (2014). Global sensitivity analysis of yield output from the water productivity model. *Environmental Modelling & Software*, **51**, pp.323–332.

Vasco, D.W., Rucci, A., Ferretti, A., Novali, F., Bissell, R.C., Ringrose, P.S., Mathieson, A.S. & Wright, I.W. (2010). Satellite-based measurements of surface deformation reveal fluid flow associated with the geological storage of carbon dioxide, Geophysical Research Letters, Volume 37, Issue 3, https://doi.org/10.1029/2009GL041544.

Verdon, J.P., Kendal, J.-M., White, D.J. & Angus, D.A. (2011). Linking microseismic event observations with geomechanical models to minimise the risks of storing CO2 in geological formations. Earth and Planetary Science Letters, 305:1–2, 143–152. ISSN 0012-821X, https://doi.org/10.1016/j.epsl.2011.02.048.

Verruijt A. Theory and Problems of Poroelasticity. Delft University of Technology. 2013.

Vogel, H. Physikalische Zeitschrift. 22 (1921) 645.

Wang W & Kolditz O (2013). High performance computing in simulation of coupled thermal, hydraulic and mechanical processes in transverse isotropic rock. Rock Characterisation, Modelling and Engineering Design Methods. 485–490.

Wang, J., Li, X., Lu, L. & Fang, F. (2013). Parameter sensitivity analysis of crop growth models based on the extended Fourier Amplitude Sensitivity Test method. *Environmental Modelling & Software*, **48**, 171–182, ISSN 1364-8152, https://doi.org/10.1016/j.envsoft.2013.06.007.

Wang, S., Li, C., Yan, W., Zou, Z., & Chen, W. (2017). Multiple indicators prediction method of rock burst based on microseismic monitoring technology. Arabian Journal of Geosciences, 10(6), 132, 10.1007/s12517-017-2946-8.

Wang, Y., Ju, Y. & Yang, Y. (2018). Adaptive Finite Element-Discrete Element Analysis for Microseismic Modelling of Hydraulic Fracture Propagation of Perforation in Horizontal Well considering Pre-Existing Fractures, Shock and Vibration, vol. 2018, Article ID 2748408, 14 pages. https://doi.org/10.1155/2018/2748408.

Wang, Y., Ju, Y., Chen, J. & Song, J. (2019). Adaptive finite element-discrete element analysis for the multistage supercritical CO2 fracturing and microseismic modelling of horizontal wells in tight reservoirs considering pre-existing fractures and thermal-hydro-mechanical coupling, Journal of Natural Gas Science and Engineering, Volume 61, Pages 251-269, ISSN 1875-5100, https://doi.org/10.1016/j.jngse.2018.11.022.

Warpinski, N. R., Wolhart, S. L., & Wright, C. A. (2001). Analysis and Prediction of Microseismicity Induced by Hydraulic Fracturing. Society of Petroleum Engineers. doi:10.2118/71649-MS.

Watanabe N. (2012) Finite element method for coupled thermo-hydro-mechanical processes in discretely fractured and non-fractured porous media. PhD Thesis, Technische Universität Dresden, Chair of Applied Environmental System Analysis, Helmholtz Centre for Environmental Research UFZ, Department of Environmental Informatics.

Watson S, Metcalfe R, Paulley A, McEwen T & Michie U (2007). Identification of how aspects of Nirex PGRC would differ if adapted to alternative geologies. Quintessa Report QRS-1338A-1.

Watson, S., Hicks, T.W., Towler, G., Reedha, D., Paulley, A., Baldwin, T.D. and Bond, A. (2009). Post-Closure Performance Assessment: Consideration of a Co-Located Geological Disposal Facility in the Safety Case. Quintessa and Galson Sciences Limited Report QRS1378P-R1 Version 2.1 for the NDA RWMD. Quintessa Ltd, Henley.

van Werkhoven, K., Wagener, T., Reed, P. & Tang, Y. (2008). Characterization of watershed model behavior across a hydroclimatic gradient. *Water Resour. Res.*, **44**, W01429, doi:10.1029/2007WR006271.

Winpenny, B., Hicks, T., Watson, S. & White, M. (2012). Separation of Co-located Geological Disposal Facility Emplacement Modules: Thermal, Hydrogeological, Mechanical, Chemical and Gas Interactions. Galson Sciences Ltd and Quintessa Report 1151b1-1, Version 1 for the NDA RWMD. GSL, Oakham.

Wileveau Y. (2005). THM Behaviour of Host Rock - Progress Report of the HE-D Experiment, Mont Terri Project, Technical Report TR2005-03.

Wileveau Y & Rothfuchs T (2003). HE-D Experiment: Test Plan. Mont Terri Project, Technical Note 2004–20.

Wileveau, Y. & Rothfuchs, T. (2006). THM behaviour of host rock (HE-D) Experiment: Study of Thermal effects on Opalinus Clay, Mont Terri Technical Report 2006-01, Switzerland.

Wileveau, Y., Su, K. & Ghoreychi, M. (2009). A Heating Experiment in the Argillites in the Meuse/Haute-Marne Underground Research Laboratory, 11th International Conference on Environmental Remediation and Radioactive Waste Management, Parts A and B, International Conference on Radioactive Waste Management and Environmental Remediation, 939-944, 10.1115/ICEM2007-7276.

Wolfs, R.J.M., Bos, F.P. & Salet, T.A.M. (2019). Triaxial compression testing on early age concrete for numerical analysis of 3D concrete printing. *Cement and Concrete Composites*, **104**, 103344, ISSN 0958-9465, https://doi.org/10.1016/j.cemconcomp.2019.103344.

Wood, D.M. (1990). Soil Behaviour and Critical State Soil Mechanics. Cambridge University Press, Cambridge.

Woodman, J., Murphy, W., Thomas, M. E., Ougier-Simonin, A., Reeves, H., & Berry, T. W. (2017). A Novel Approach to the Laboratory Testing of Replica Discontinuities: 3D Printing Representative Morphologies. American Rock Mechanics Association.

Xiang, J., Munjiza, A., Latham, J.P. & Guises, R. (2009) On the validation of DEM and FEM/DEM models in 2D and 3D, Engineering Computations, Vol. 26 Issue: 6, pp.673-687, https://doi.org/10.1108/02644400910975469.

Xiong, Y. L., Yang, Q. L., Sang, Q. Y., Zhu, Y. H., Zhang, S., & Zheng, R. Y. (2019). A unified thermal-hardening and thermal-softening constitutive model of soils. Applied Mathematical Modelling, 74, 73–84, ISSN 0307-904X, https://doi.org/10.1016/j.apm.2019.04.034.

Yu, C. & Shapiro, S. (2014). Seismic anisotropy of shale: Inversion of microseismic data, SEG Technical Program Expanded Abstracts 2014, 2324–2329, 10.1190/segam2014-1251.1.

Yven, B., Sammartino, S., Geraud, Y., Homand, F. & Villieras, F. (2007), Mineralogy, texture and porosity of the Callovo-Oxfordian argillites ofthe Meuse/Haute Marne region (eastern Paris Basin), Mem. Soc. France,178, 73–90.

Zhang, M., Takahashi, M., Morin, R. & Esaki, T. (2000). Evaluation and Application of the Transient-Pulse Technique for Determining the Hydraulic Properties of Low-Permeability Rocks–Part 2: Experimental Application. *Geotechnical Testing Journal*, **23**, 1, 91–99. https://doi.org/10.1520/GTJ11127J.

Zhang, C., & Rothfuchs, T. (2004). Experimental study of the hydro-mechanical behaviour of the Callovo-Oxfordian argillite. Applied Clay Science, 26(1-4), 325-336.

Zhang CL, Rothfuchs T, Moog H, Dittrich J and Müller J (2004a). Thermo-Hydro-Mechanical and Geochemical Behaviour of the Callovo-Oxfordian Argillite and the Opalinus Clay. June 2004, GRS-202, ISBN3-931995-69-0.

Zhang CL, Rothfuchs T, Jockwer N, Kröhn K-P, Miehe R and Moog H (2004b). Results of Laboratory Investigations on Clays, Proc. International Conference on Radioactive Waste Disposal - DisTec 2004, Berlin 26-28 April 2004.

Zhang CL, Wileveau Y and Rothfuchs T (2005). A Heating Experiment in the Opalinus Clay at the Mont Terri Rock Laboratory. The 10th International Conference on Environmental Remediation and Radioactive Waste Management, Glasgow, Scotland.

Zhang, CL., Rothfuchs, T., Wieczorek, K., Jockwer, N. & Wileveau, Y. (2006). Monitoring and Modelling of Responses of the Opalinus Clay to Heating. *Chinese Journal of Rock Mechanics and Engineering* **25**, 4, 659–669.

Zhang, CL., Rothfuchs, T., Jockwer, N., Wieczorek, K., Dittrich, J., Müller, J., Hartwig, L. & Komischke, M. (2007a). Thermal effects on the Opalinus clay. A joint heating experiment of ANDRA and GRS at the Mont Terri URL (HE-D Project). Final report. Gesellschaft fuer Anlagen-und Reaktorsicherheit mbH (GRS).

Zhang, CL., Rothfuchs, T., Su, K. & Hoteit, N. (2007b). Experimental study of the thermo-hydro-mechanical behaviour of indurated clays. *Physics and Chemistry of the Earth*, Parts A/B/C, **32**, 8–14, 957–965, ISSN 1474-7065, https://doi.org/10.1016/j.pce.2006.04.038.

Zhang, J. (2013). Borehole stability analysis accounting for anisotropies in drilling to weak bedding planes. *International Journal of Rock Mechanics and Mining Sciences*, **60**, 160–170, ISSN 1365-1609, https://doi.org/10.1016/j.ijrmms.2012.12.025.

Zhang, X., Chen, Z., & Liu, Y. (2016). The material point method: a continuum-based particle method for extreme loading cases. Academic Press.

Zhao, C., Hobbs, B.E. and Ord, A. (2008). Convective and Advective Heat Transfer in Geological Systems. Springer.

Zhao T., Guo W., Tan Y., Lu C. & Wang C. (2018a). Case histories of rock bursts under complicated geological conditions. *Bulletin of Engineering Geology and the Environment*, **77**, 4, 1529–1545.

Zhao, JS., Feng, XT., Jiang, Q. & Zhou, YY. (2018b). Microseismicity monitoring and failure mechanism analysis of rock masses with weak interlayer zone in underground intersecting chambers: A case study from the Baihetan Hydropower Station, China. *Engineering Geology*, **245**, 44–60, ISSN 0013-7952, https://doi.org/10.1016/j.enggeo.2018.08.006.

Zhou, F., Shi, A. & Wang, X. (2014). An efficient finite difference model for multiphase flow in fractured reservoirs. *Petroleum Exploration and Development*, **41**, 2, 262–266, ISSN 1876-3804, https://doi.org/10.1016/S1876-3804(14)60031-8.

Zhu, J. (2019). Non-linear flow reduction factor and effective permeability of fractal fracture network. *Journal of Natural Gas Science and Engineering*, **66**, 138–147, ISSN 1875-5100, https://doi.org/10.1016/j.jngse.2019.03.029.

Zou, L., Jing, L. & Cvetkovic, V. (2017). Shear enhanced nonlinear flow in rough-walled rock fractures. *Int J Rock Mech Min Sci*, **97**, 33–45.

APPENDIX

Table A.1 provides a comprehensive list of operating and discontinued URLs reported in Gens (2018). Purpose built URLs have been sited in argillaceous, crystalline and salt host rocks.

Table A.2 is a country by country summary of HLW and spent fuel disposal plans reported in Fayblshenko et al. (2016). Host rocks can broadly be categorized using the UK generic concepts: higher strength rock, lower strength sedimentary rock and evaporite rock. Lower strength sedimentary rocks are commonly specified as claystones and siltstones.

Country	URL name	Host rock	Status
Belgium	HADES Underground Research Facility	Argillaceous	Operational, purpose-built
Finland	ONKALO	Crystalline	Operational, purpose-built
France	Meuse Haute-Marne URL	Argillaceous	Operational, purpose-built
Germany	Gorleben Exploratory Mine	Salt	Operational, purpose-built
Japan	Horonobe Underground Research Center	Sedimentary	Operational, purpose-built
Japan	Mizunami URL	Crystalline	Operational, purpose-built
Republic of Korea	KAERI Underground Research Tunnel	Crystalline	Operational, purpose-built
Sweden	Äspö Hard Rock Laboratory	Crystalline	Operational, purpose-built
Switzerland	Grimsel Test Site	Crystalline	Operational, purpose-built
Switzerland	Mont Terri Rock Laboratory	Argillaceous	Operational, purpose-built
Czech Republic	Josef Underground Research Centre	Crystalline & tuff	Operational, pre-existing
Finland	Olkiluoto Research Tunnel	Crystalline	Operational, pre-existing
France	Tournemire URL	Argillaceous	Operational, pre-existing
Germany	KONRAD	Sedimentary	Operational, pre-existing
Canada	AECL URL	Crystalline	Not operational
France	Amelie	Salt	Not operational
France	Fanay-Augères	Crystalline	Not operational
Germany	Asse Mine	Salt	Not operational
Germany	Morsleben	Salt	Not operational
Hungary	Pécs	Argillaceous	Not operational
Japan	Tono Mine	Sedimentary	Not operational
Japan	Kamaishi Mine	Crystalline	Not operational
Sweden	Stripa mine	Crystalline	Not operational
USA	Climax	Crystalline	Not operational
USA	G-Tunnel	Tuff	Not operational
USA	Yucca Mountain	Tuff	Not operational
USA	WIPP	Salt	Not operational

Table A.1: A comprehensive list of operating and discontinued URLs with categorized host rocks (Gens, 2018).

Country	Host rock classification	Notes	Status
China	Higher strength rock	Granite	Conceptualized
Czech Republic	Higher strength rock	Bohemian Massif granitoids	Host rock formation determined
Finland	Higher strength rock	Veined gneiss, pegmatitic granite and granodiorite	Sited: Onkalo Underground Rock Characterization Facility
India	Higher strength rock	Granite, 500–600 m depth	
Slovenia/Croatia	Higher strength rock		
South Africa	Higher strength rock		Sited: Vaalputs Radioactive Waste Disposal Facility
Sweden	Higher strength rock	Forsmark: granite, aplite, pegmatite, gabbro, etc.	Location determined: Forsmark
Ukraine	Higher strength rock	Archaean and Proterozoic granitoid formations	Location determined: Chernobyl exclusion zone
Bulgaria	Lower strength sedimentary	Lower Cretaceous clayey marl and Neogene clay	
France	Lower strength sedimentary	Callovo-Oxfordian Clay, 500 m depth	Host rock formation determined
Hungary	Lower strength sedimentary	Boda Claystone Formation	Host rock formation determined
Switzerland	Lower strength sedimentary	Opalinus Clay	Host rock formation determined
Canada	Undetermined	Crystalline/sedimentary	Site selection process
Germany	Undetermined	Unrestricted selection	New site selection process, previously Gorleben salt dome
Japan	Undetermined	Unrestricted selection	Voluntary siting process
Lithuania	Undetermined	Crystalline/Lower Cambrian Baltija and Lower Triassic clay fms.	Conceptualization and generic safety assessment
Mexico	Undetermined	Granite/salt/clay/tuff or multinational repository	
Slovak Republic	Undetermined	Granitoids/siltstones/claystones or multinational repository	
UK	Undetermined	Unrestricted selection	Voluntary siting process
USA	Undetermined	Crystalline/argillite/salt	
Latvia	Undetermined	Multinational repository	
Brazil	No data		
Spain	No data		

Table A.2: A country by country list of potential and determined host rocks and radioactive waste disposal project status (Fayblshenko et al., 2016). Slovenia and Croatia have shared responsibilities for their radioactive waste.